technische universität
dortmund

Dissertation

Tuning spin and charge at a metal-organic hybrid interface

Submitted in partial fulfillment of the
requirements for the degree of

Dr. rer. nat.

to the Faculty of Physics of the
TU Dortmund University, Germany

by
Henning Sturmeit

Dortmund, November 2021

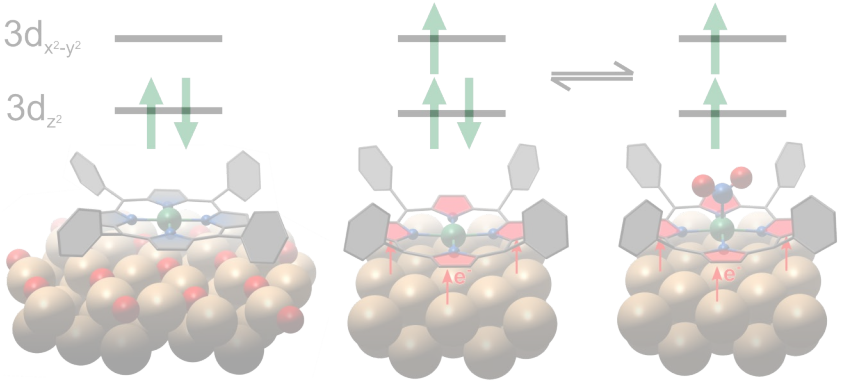

Accepted by the Faculty of Physics of the TU Dortmund University, Germany.

Date of the oral examination: 3rd February 2022

Examination board:

Prof. Dr. Mirko Cinchetti

Prof. Dr. Carsten Westphal

Prof. Dr. Marc Aßmann

Dr. Gerald Schmidt

Abstract

Metal-organic interfaces are key constituents of the various functional building blocks that can be found in molecular electronics and spintronics. Long electron and spin relaxation times of organic molecules make them superior to inorganic materials for many technological devices. When put into contact with a metal electrode, the hybridization of molecular orbitals and metallic states can lead to several intriguing effects, which strongly affect the electronic and magnetic properties of the system. In this regard, the interface obtained by depositing nickel tetraphenyl porphyrin onto the copper (100) surface (NiTPP/Cu(100)) can be seen as an interesting model system. Previous experiments reported an unexpected high charge transfer leading to a partial filling of the molecular orbitals up to the LUMO+3 and a reduction of the central nickel atom. Considering this observation as the point of departure, this thesis aims to develop different approaches to alter the hybridization at this interface.

The results of this thesis can be divided into three main topics. First, it is shown that a pre-oxidation of the copper substrate leads to a substantial quenching of the charge transfer from the metal to the molecule and, thereby, weakens the interaction. Crucially, the molecules adsorb in a well-defined geometry, thus allowing for the determination of the molecular orbital symmetry. This is a major advantage over gas-phase and multilayer measurements, as in such cases, a random molecular orientation prevents an evaluation of the orbital symmetry via near-edge x-ray absorption fine structure spectroscopy. Moreover, the so-obtained NiTPP/O-Cu(100) interface can be used as a reference system, which enables a direct comparison of the weakly and strongly hybridized NiTPP molecules.

In a second approach, the NiTPP/Cu(100) interface was exposed to a few Langmuirs of nitric dioxide (NO_2) gas. The NO_2 molecules are found to bind to the central nickel atom of the NiTPP molecules. A comparison of the d shell configuration of the pristine and NO_2-modified system reveals that the on-top ligation leads to a reduction of the nickel center. Remarkably, the nickel center in NO_2-NiTPP/Cu(100) has a d^8 configuration with two unpaired electrons, which is in contrast to the situation in gas-phase molecules where the central ion is in a d^8 configuration without unpaired electrons. Thus, NO_2 adsorption enables a spin switching from d^9 to d^8 with two unpaired electrons. Interestingly, the electronic structure of the molecular macrocycle is only weakly perturbed by the NO_2 adsorption. Moreover, annealing up to 390 K suffices to remove the adsorbed NO_2 molecules and restores the original electronic configuration of the central nickel atom.

When annealed to high temperatures, substrate-supported porphyrins often undergo structural changes, which is disadvantageous for many applications. The third part of the results addresses the temperature-induced changes at the NiTPP/Cu(100) interface upon annealing. Up to the limit of thermal decomposition, the NiTPP molecules do not undergo chemical changes but only conformational modifications. This is in contrast to what has been observed for similar metal-molecule combinations. Generally, porphyrins are prone to dehydrogenation reactions at the periphery of the molecule, which is usually connected to a ring-closing reaction in which peripheral substituents bind to the macrocycle. A rotation of the phenyls to a more coplanar orientation and an enhanced charge transfer from the metal to the molecule result in a strengthened molecule-substrate interaction. All experimental evidence points toward molecular pinning as the underlying reason that prevents the molecule from a complete flattening.

Zusammenfassung

Metall-organische Grenzflächen sind wichtige Bestandteile verschiedener funktionaler Bauteile, die in Molekularelektronik und Spintronik zu finden sind. Aufgrund langer Elektronen- und Spin-Relaxationszeiten sind organische Moleküle anorganischen Materialien für viele technische Bauteile überlegen. In Kontakt mit einer Metallelektrode kann die Hybridisierung von Molekülorbitalen und metallischen Zuständen zu vielen faszinierenden Effekten führen, welche die elektronischen und magnetischen Eigenschaften des Systems stark verändern. In diesem Zusammenhang kann die Grenzfläche, die durch das Aufdampfen von Nickel-Tetraphenyl-Porphyrinen auf eine Kupfer(100)-Oberfläche (NiTPP/Cu(100)) entsteht, als interessantes Modellsystem betrachtet werden. In früheren Experimenten wurde ein unerwartet hoher Ladungstransfer beobachtet, der zu einer partiellen Füllung der Molekülorbitale bis hin zum LUMO+3 und zu einer Reduktion des zentralen Nickelatoms führt. Ausgehend von dieser Beobachtung zielt diese Arbeit darauf ab, verschiedene Ansätze zur Veränderung der Hybridisierung an dieser Grenzfläche zu entwickeln.

Die Ergebnisse dieser Arbeit lassen sich in drei Hauptthemen unterteilen. Zuerst wird gezeigt, dass eine Oxidation des Kupfersubstrats zu einer erheblichen Verringerung des Ladungstransfers vom Metall zum Molekül führt und die Wechselwirkung schwächt. Trotz der Oxidation adsorbieren die Moleküle in einer wohldefinierten Geometrie, so dass die Symmetrie der Molekülorbitale bestimmt werden kann. Dies ist ein großer Vorteil gegenüber Gasphasen- und Mehrschichtmessungen, da in solchen Fällen eine zufällige Molekülorientierung eine Auswertung der Orbitalsymmetrie mittels Röntgen-Nahkanten-Absorptions-Spektroskopie verhindert. Außerdem kann die so erhaltene NiTPP/O-Cu(100)-Grenzfläche als Referenzsystem verwendet werden, was einen direkten Vergleich der schwach und stark hybridisierten NiTPP-Moleküle ermöglicht.

In einem zweiten Ansatz wird die NiTPP/Cu(100)-Grenzfläche einigen Langmuir von Stickstoffdioxid (NO_2) ausgesetzt. Es wird gezeigt, dass die NO_2-Moleküle an das zentrale Nickelatom der NiTPP-Moleküle binden. Ein Vergleich der Elektronenkonfiguration der d-Schale des ursprünglichen und des NO_2-modifizierten Systems zeigt, dass die Bindung zu einer Reduktion des Nickelatoms führt. Außerdem liegt das Nickelatom in NO_2-NiTPP/Cu(100) in einer d^8-Konfiguration mit zwei ungepaarten Elektronen, was im Gegensatz zur Konfiguration in Gasphasenmolekülen steht, in denen das zentrale Ion eine d^8-Konfiguration ohne ungepaarte Elektronen aufweist. Somit ermöglicht die NO_2-Adsorption eine Änderung der Spinkonfiguration, von d^9 mit einem, zu d^8 mit zwei ungepaarten Elektronen. Interessanterweise wird die elektronische Struktur des molekularen Makrozyklus durch die NO_2-Adsorption nur geringfügig gestört. Darüber hinaus reicht ein Aufheizen bis 390 K aus, um die adsorbierten NO_2-Moleküle zu entfernen und die ursprüngliche elektronische Konfiguration des zentralen Nickelatoms wiederherzustellen.

Bei hohen Temperaturen, verändert sich häufig die chemische Struktur substratgestützter Porphyrine, was für viele Anwendungen nachteilig ist. Der dritte Teil der Ergebnisse befasst sich mit den temperaturbedingten Veränderungen an der NiTPP/Cu(100)-Grenzfläche beim Aufheizen. Bis zur thermischen Zersetzung durchlaufen die NiTPP-Moleküle keine chemischen Veränderungen, sondern nur Konformationsänderungen. Dies steht im Gegensatz zu dem, was bei ähnlichen Metall-Molekül-Kombinationen beobachtet wurde. Im Allgemeinen sind Porphyrine anfällig für Dehydrierung an der Peripherie des Moleküls, die in der Regel mit Ringschlüssen verbunden sind, bei denen die peripheren Substituenten an den Makrozyklus des Moleküls binden. Eine Rotation der Phenyle in eine eher koplanare Ausrichtung und ein verstärkter Ladungstransfer vom Metall zum Molekül führen zu einer verstärkten Molekül-Substrat-Wechselwirkung. Alle experimentellen Indizien deuten darauf hin, dass eine Verankerung der Moleküle an das Substrate die vollständige Abflachung des Moleküls verhindert.

Contents

1. Introduction

In recent years, a rapid miniaturization trend in spintronics has led to a variety of new device architectures for functional building blocks. Since the discovery of the giant magnetoresistance (GMR) in the late eighties* [1], various designs rely on the control of the motion of electrons by acting on their spin via magnetic fields. This approach holds promises for applications in countless areas, such as data storage, sensing, and photovoltaic applications.

For most of these applications, long spin relaxation times are desired. Initial approaches were based on all-metallic device architectures. However, as metals typically have spin relaxation times ranging from the pico- to the microsecond regime [2], a coherent spin manipulation is hardly achievable in applicative conditions. In this respect, molecular semiconductors build a particularly interesting class of materials as they not only possess spin relaxation times ranging up to the millisecond regime but also have high photoelectric and magnetic field responsivities [3].

To fully exploit the versatility of organic semiconductors, the concept of multifunctional devices has been proposed recently [4]. While originally introduced to refer to materials that can be used for a vast range of applications [5], the term "multifunctional" has been recently used to describe devices that unite several functionalities based on different molecular properties [6]. An early example of such a multifunctional device was provided by Sun *et al.* [4], who devised an organic spin valve based on fluorinated copper phthalocyanine ($F_{16}CuPc$) between two ferromagnetic electrodes. By separate adjustment of light irradiation and external magnetic field, four different resistance states can be realized in a single device, offering prospects for novel sensing devices. However, despite these remarkable findings, this research area is still in its infancy as fundamental mechanisms behind the charge injection from typical metallic electrodes into the organic layers are yet to be fully understood.

When molecules are put into contact with a metal, the (spin-dependent) electronic energy level alignment and, thus, the charge injection properties are largely defined by the hybridization between the frontier molecular orbitals and the electronic bands of the surface. The interaction strength typically ranges from the regime of physisorption, in which weak van der Waals forces rule the molecule-substrate interaction (typical for rather inert metals like Au), up to chemisorption, where chemical bonds and interfacial charge transfer can occur [7]. In the chemisorption regime, the hybridization can, even on non-ferromagnetic metals, lead to intriguing magnetic phenomena on the molecule as well as on the substrate side. For example, the adsorption of Buckminster fullerenes (C_{60}) on a diamagnetic copper surface can lead to the emergence of magnetic ordering at the surface at room temperature [8].

* The groups of Albert Fert of the Paris-Sud University and Peter Grünberg of the Forschungszentrum Jülich independently discovered GMR. In recognition, Fert and Grünberg were jointly awarded the Nobel Prize in Physics 2007.

To optimize device performance, e.g., for improving spin injection in organic spin valves, strategies to tune the hybridization at metal/molecular interfaces are required. Promising approaches are pursued in the field of on-surface magnetochemistry [9], where coordination chemistry is exploited to tailor the magnetic properties of adsorbed molecules. Due to their rich coordination chemistry and self-assembly, square-planar transition metal complexes, such as porphyrins or phthalocyanines, are particularly suitable candidates to provide platforms for tailoring interfacial magnetic properties at room temperature [10,11]. Wäckerlin *et al.* demonstrated a reversible spin-switching via on-top ligation of different tetraphenyl porphyrin/ferromagnet combinations [12]. This experiment demonstrates that fundamental parameters, such as the spin and oxidation state of the contained metal ions, can be controlled.

The present thesis aims at exploring the tunability of the hybridization at metal-organic interfaces using the example of nickel tetraphenyl porphyrin on a copper (100) substrate (NiTPP/Cu(100)). This system was identified as an interesting model system since an unexpected high interfacial charge transfer leads to a partial filling of the molecular orbitals up to the LUMO+3 [13] and a reduction of the molecular nickel center [14]. To this end, an extensive set of surface science techniques was employed to investigate three different approaches modifying the molecule-surface hybridization. First, an oxygen treatment of the copper substrate is shown to be a viable way to quench the previously reported high charge transfer toward the NiTPP molecules. Since the NiTPP molecules form an ordered self-assembled monolayer on the oxygen-modified copper surface, the resulting NiTPP/O-Cu(100) interface can be seen as a reference system for a weakly hybridized interface. In the second part, the effects of NO_2 as an axial ligand bound to the open Ni coordination site is investigated. This ligation is demonstrated to lead to a change of the spin configuration of the central Ni ion, while the electronic level alignment of the frontier molecular orbitals remains vastly unchanged, offering perspectives for electronic devices whose optical/ transport and magnetic properties can be addressed independently. For practical applications, it is often required to restore the electronic properties of the pristine system. Annealing to several hundred Kelvin is a common means of choice for removing axial ligands from metal-organic interface. Therefore, the third part discusses thermally induced changes at the NiTPP/Cu(100) interface. The strong molecule-metal interaction is shown to stabilize the molecules against chemical modifications.

Chapter 2 provides an overview of the basic properties of porphyrin molecules. This is followed by a short introduction of their adsorption behavior on metal substrates and the implications of ligation with on-top adsorbed small gas molecules.

Chapter 3 briefly reviews the results previously obtained for the model system NiTPP/Cu(100). Subsequently, two open questions are formulated, which are of central importance in view of potential applications and shall be answered in this thesis.

Chapter 4 gives a short introduction to the experimental techniques that have been used in this work. Various complementary surface-sensitive methods were employed to get a consistent picture of the hybridization of the investigated model interface and its modified versions. Information about the electronic structure and, therefore, the chemical and conformational structure of the molecules is obtained by photoemission tomography (PT),

x-ray photoemission spectroscopy (XPS), as well as near-edge x-ray absorption fine structure spectroscopy (NEXAFS). A spin sensitivity can be gained by measuring the absorption of circularly polarized light. This is exploited in x-ray magnetic circular dichroism (XMCD) measurements. By probing imbalances in the spin-dependent unoccupied density of states at the valence bands, a comprehensive picture of the magnetic properties of the investigated systems is drawn. The vibronic properties are probed by infrared reflection absorption spectroscopy (IRAS). In addition to further confirming the adsorption geometry, this technique also yields information on the adsorption of small gases on a buried monolayer. Such information is barely accessible through photoemission-based techniques, as the short inelastic electron mean free path leads to a small probing depth. Lastly, a short introduction of scanning tunneling microscopy is given, which yields additional complementary information on the topology of the systems.

In **chapter 5**, the results of this thesis are presented and discussed. At first, the quenching of the charge transfer through a pre-oxidization of the copper substrate is introduced. As an interface with a weak metal-molecule interaction, this system serves as a reference for the subsequent experiments. In the next step, the reactivity of the different systems to NO_2 molecules is investigated, and a consistent picture of the electronic, magnetic, and geometric properties of the functionalized interfaces is given. Finally, the thermal stability of this system at elevated temperatures is investigated.

2. Porphyrin molecules

This chapter provides a short review of the fundamental properties of porphyrins that are necessary to understand the results presented in this thesis. At first, the structure and fundamental aspects of this molecule class are introduced. After that, the adsorption behavior and chemical reactivity to small gasses are discussed.

2.1. Basic properties

Porphyrins are π-conjugated molecules that are ubiquitous both in nature and in vital-related processes, e.g., as light harvesters in the photosynthesis apparatus of plants, as oxygen binding centers in heme proteins, and as important cofactors in enzymes. Their versatile coordination chemistry is extremely appealing both for model systems aiming to understand critical processes in nature and for artificial devices with novel functionalities [15,16]. Porphyrin is a derivative of porphin, which consists of four pyrrole moieties and builds the macrocycle of porphyrin. Porphyrin is obtained by attaching additional peripheral substituents. Remarkably, it can form stable complexes with almost all the elements in the periodic table. Hence, a $3d$ metal atom can be introduced through metalation [17,18], which offers the possibility of tailoring the molecule's electronic and magnetic properties to specific needs for a wide range of applications. The $3d$ metal incorporation into porphyrin molecules leads to the same nearly square-planar coordination present in biological systems like Chlorophyll, Heme B, and the cofactor F430, which are responsible for photosynthesis, oxygen uptake of the human body, and enzymatic processes, respectively. The cofactor F430, for instance, features a macrocyclic ring system with a tetracoordinated nickel atom. This geometric ligand configuration is also present in nickel tetraphenyl porphyrin (NiTPP), which is shown in Figure 1. However, while the central Ni atom is in a +1 oxidation state in the cofactor F430, it is in a +2 oxidation state

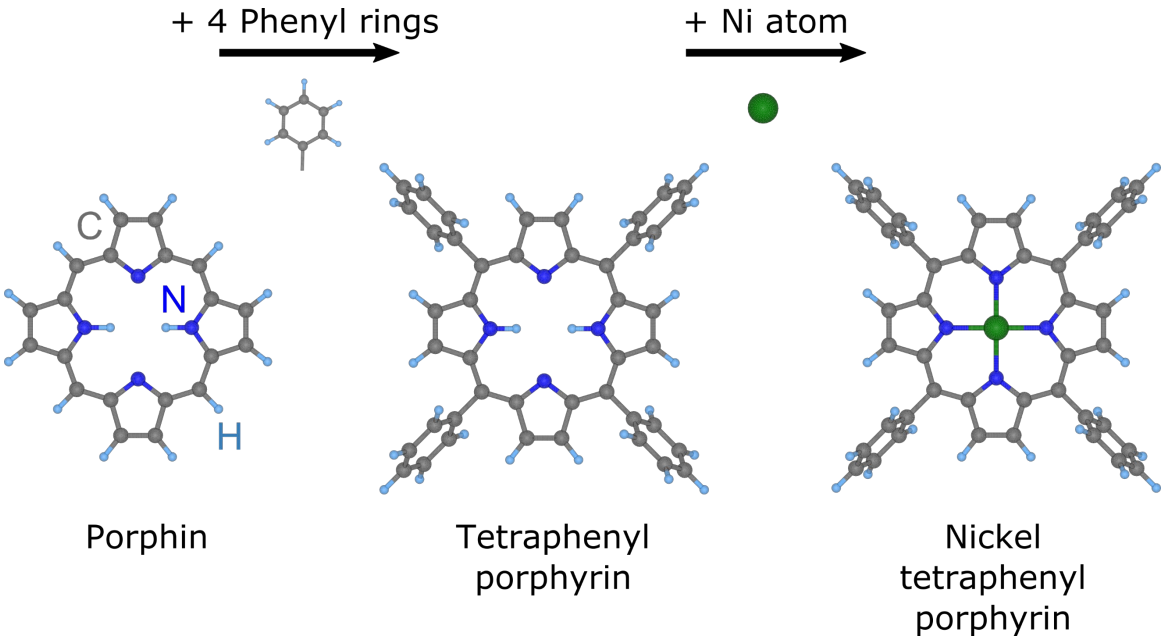

Figure 1) Ball-and-stick models of free-base porphin (2HP), tetraphenyl porphyrin (2HTPP), and nickel tetraphenyl porphyrin (NiTPP). Figure adapted from [43].

in the gas phase NiTPP molecule. Aside from a match of the metal center and the crystal field surrounding it, the periphery of the molecule is also a crucial factor in the description of the molecule properties. As an example, the sterical hindrance due to macrocycle-substituent interaction determines the flexibility and the equilibrium conformation of the molecule. For certain peripheries, such as the four phenyl rings in a tetraphenyl porphyrin, the steric repulsion between the hydrogens at the phenyl rings and the macrocycle can lead to a saddle-shaped equilibrium structure of the porphin cycle and a noncoplanar orientation of the peripheral substituents even in the gas phase or solution [19]. The adsorption geometry of the phenyl rings can be described in the notation of Wölfle *et al.* [20], where a twist angle (θ) and a tilt angle (Φ) are used. The twist angle describes the rotation of the phenyl rings around the σ-bonds by which they are attached to the macrocycle, whereas the tilt angle is the angle of the out-of-plane bending of the phenyl groups [20]. The angles are illustrated in Figure 2 at the example of NiTPP adsorbed on Cu(100).

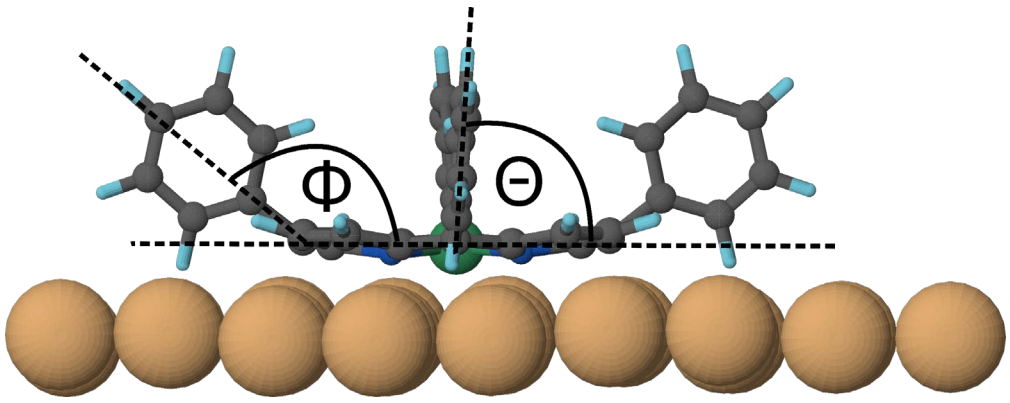

Figure 2) Twist angle Θ and tilt angle Φ at the example of nickel tetraphenyl porphyrin (NiTPP) adsorbed on a Cu(100) surface. Figure adapted from [13].

The degree of distortion can be also influenced by the choice of the complexed metal. Generally, a more rigid macrocycle can be achieved through the incorporation of larger metal atoms [21]. In addition, the latter ones also essentially define natural processes and device functionalities through their specific spin and oxidation states. In general, a gas phase metalloporphyrin has a central metal ion in a formal +2 oxidation state, as the porphyrin acts as a dibasic acid [15]. The central metal ion is exposed to a crystal field with a D_{4h} symmetry surrounded by four electronegative nitrogen atoms. For pure d orbitals, this generally results in a crystal field splitting into one degenerate and three non-degenerate orbitals, as shown in Figure 3.

This was also computed for the orbital energies of gas-phase tetraphenyl porphyrins with a d-like character. Aside from the case of FeTPP, the three lower orbitals get fully occupied first [22]. As suggested by Figure 3, the order of the $3d$ levels, and therefore the electronic and magnetic properties of the molecule, can be further tuned by adding ligands to its axial

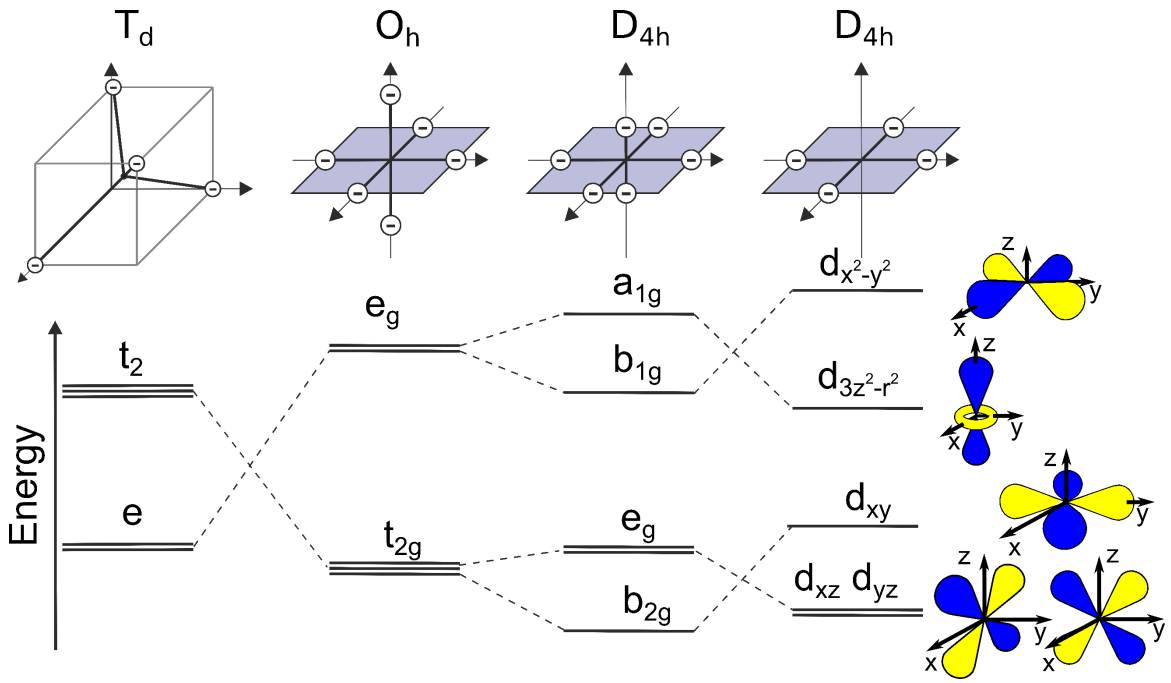

Figure 3) Crystal field splitting for a single d electron surrounded by different arrangements of electronegative ligands. In a tetrahedral (T_d) and octahedral (O_h) cubic symmetry, the d orbitals split into two groups of degenerate energy levels which form the bases of irreducible representations, while for both of the two tetragonal symmetries (D_{4h}) one has two degenerate and three non-degenerate energy levels. Figure adapted from [73].

positions. This can be realized with randomly oriented tetrapyrroles in solution, as in human blood [23], on a single-molecule scale with absorbed molecules by an STM tip [24], by the interaction with the substrate itself [13], or by the functionalization of adsorbed porphyrins by small gas molecules [12]. The latter two aspects will be discussed in the following chapters.

2.2. Adsorption on metal substrates

Due to an interplay of molecule-molecule and molecule-substrate interactions, metalloporphyrins often self-assemble in ordered two-dimensional (2D) lattices, and the geometric properties of single molecules are drastically modified upon deposition on metal substrates [15,16]. The fact that metalloporphyrins arrange in long-range ordered arrays owing to non-covalent interactions, offers the possibility for bottom-up fabrication of electronic devices with nanometer precision [25]. Additionally, an understanding of the surface-induced modifications of the mutually related geometric, electronic, and magnetic properties of individual molecules is essential for the design of functional building blocks [26]. The influence of the substrate on the molecular self-assembly is discussed in the subsequent section, followed by a discussion on surface-induced modifications on a single-molecule scale.

2.2.1. Molecular self-assembly

Both attractive and repulsive lateral interactions between molecules have been observed in the supramolecular patterning of porphyrins on metal substrates. For tetraphenyl porphyrins, a trend regarding the substrate-dependence of these lateral interactions can be identified: while metalated porphyrins show a substrate-independent lateral attraction, free-base porphyrins (2HTPP) behave differently on strongly and weakly interacting surfaces [15]. As a consequence, metalated tetraphenyl porphyrins form ordered islands already at coverages below one monolayer (ML) on strongly [27] and weakly [28] interacting substrates. In contrast, free-base tetraphenyl porphyrins form densely packed islands only on weakly interacting surfaces such as Ag(111) [29], and adsorb in an unordered fashion on strongly interacting surfaces such as Cu(111) [27]. Notably, in addition to the central metal atom, the periphery of the molecule also plays a major role. This is demonstrated by the different adsorption behaviors of free-base porphyrin and porphin rings on Ag(111).

2.2.2. Influence on individual molecules

Upon adsorption on a metal substrate, the geometric, electronic, and magnetic properties of single molecules can be substantially modified. A thorough understanding of these chemical and conformational changes can open new avenues for the use of molecules designed to engage specific bonds that enable desired device functionalities and performance. The influence of the substrate on single molecules will be discussed first for weakly interacting surfaces and then for strongly interacting surfaces. While on weakly interacting surfaces, primarily changes in the molecular conformation can be observed, strongly interacting surfaces are also found to promote chemical changes. This can happen in the form of molecule-substrate bonds, as well as surface-assisted intramolecular modifications.

On weakly interacting surfaces, the molecules can undergo non-reactive adaptions by changing their conformation vis-à-vis the gas-phase equilibrium state. Two competing interactions determine the configuration of an adsorbed molecule. On the one hand, attractive van der Waals forces act to maximize the contact area [15]. On the other hand, steric repulsive forces between the hydrogen atoms attached to the macrocycle and phenyls favor a saddle shape, as already mentioned in section 2.1 for gas-phase molecules. This can lead to a tilt of the phenyls with respect to the surface of 30° as observed for CoTPP/Ag(111) [29]. The equilibrium between the two interactions depends on the substrate and the properties of the porphyrin and, therefore, can differ enormously for different surfaces and metal centers.

On more reactive surfaces, the chemical structure of the molecules can be additionally modified by the formation of covalent bonds with the substrate. As shown for porphins and porphyrins, this can lead to a partial filling of the lowest unoccupied molecular orbitals (LUMOs) [30,31]. For 2HTPP on Cu(111), the interaction was found to involve an electron donation from the nitrogen atoms to the metal [32] but also a quenching of an absorption feature ascribed to the LUMO [31]. Therefore, this charge transfer can be described as a donation/ back-donation mechanism rather than a net charge transfer and generally involves

all parts of the molecule, i.e., the nitrogens, the porphin cycle, and the peripheral phenyls [15,30]. As processes like diffusion, reaction, and conformational switching often have higher activation energies when molecules bind to the surface (compared to molecules that interact via van der Waals forces with the substrate), they become accessible even far beyond cryogenic temperatures [33]. This offers perspectives for switching applications at and even above room temperature.

Aside from molecule-substrate bonds, also the formation of new intramolecular bonds is possible. For temperatures that are sufficiently high to induce C-H bond dissociation, subsequent binding of the carbon atoms at the peripheral substituents of the porphyrins to the macrocycle carbons was observed for different porphyrin-substrate combinations [34–36]. This is commonly referred to as cyclodehydrogenation or ring-closing reaction. Even though these reactions happen at the periphery of the molecule and the atoms adjacent to the central metal atom are not directly involved, they can lead to a change in the latter's magnetic anisotropy. This was reported for FeOEP on Au(111), where the ring-closure reaction was accompanied by a substantial increase of the effective spin moment of the complexed Fe ion [35]. Therefore, surface-assisted reactions provide a new path for tailoring the magnetic properties of molecules for their use in spintronics.

2.3. Reactivity to small gases

Besides the surface-induced filling of LUMOs and the ring-closing reactions mentioned above, the magnetic and electronic properties of on-surface porphyrins can be further adjusted to specific needs by coordinating additional ligands to the free axial binding position available on top of the chelated metal ion. A central concept introduced for the description of the phenomena that have been observed experimentally so far is the surface-*trans* effect. In analogy to the classical *trans* effect [37], which is well-established in solution chemistry, the surface-*trans* effect describes the competition for the stronger bond between two ligands that bind to the same metal center in a *trans* configuration (shown in Figure 4), one of which is the surface [38]. The surface-*trans* effect can not only lead to changes in the electronic energy level alignment [38], but it often also has a substantial impact on the magnetic properties of the porphyrins. For example, it can lead to the compensation of spins of the adsorbed gas and the porphyrin center [12], or a change in the crystal field surrounding the central metal atom inducing a high-spin configuration [10].

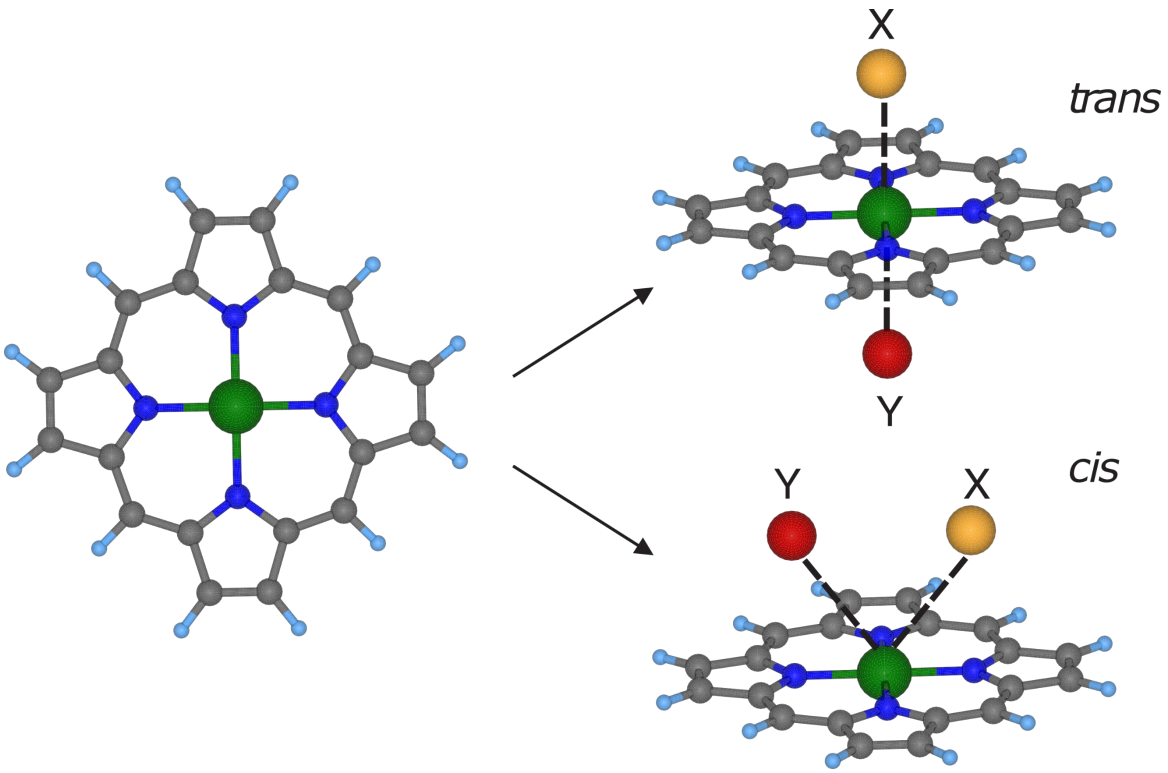

Figure 4) Trans- and cis-configuration of two ligands binding to the metal center of a porphin molecule. Figure adapted from [15].

The surface-*trans* effect is often responsible for a decoupling of metallporphyrins from the supporting substrate. Hieringer *et al.* found that the interaction between the central metal atom of different porphyrins and the Ag(111) surface was essentially weakened by the coordination of NO [38]. In the case of NO-CoTPP/Ag(111), the additional bond to an NO molecule even leads to the disappearance of surface-induced valence states, which points to a significant realignment of the electronic energy levels. Furthermore, this also has consequences on the spin configuration, as suggested by core-level photoemission measurements on NO-CoTPP/Ag(111) [39]: while there is a multiplet structure in the Co $2p_{3/2}$ spectrum of CoTPP/Ag(111), the adsorption of NO leads to a single peak. This was

explained by a pairing of the formerly unpaired spins in the CoTPP and NO molecules, respectively, in a mixed NO-Co bonding orbital. By means of density functional theory (DFT) calculations, the competition between the bond to the Ag substrate and the one to the NO molecule was found to increase the substrate-porphyrin distance by 0.2 Å.

A similar result, with a significantly smaller increase in the distance between the central cobalt atom and the topmost layer of surface atoms, was obtained by Wäckerlin *et al.* for NO-CoTPP/Ni(100). Here, DFT calculations suggested for the simplified case of CoP/Ni(100) a cobalt-nickel distance of only 0.06 Å, indicating a much weaker *trans* effect [40]. Still, the two unpaired electrons occupy the orbital formed upon adsorption, leading to a diamagnetic on-surface complex, as demonstrated by XMCD [40].

Aside from the compensation of spins of the two molecules, the surface-*trans* effect can also lead to a transition from a ferromagnetic to an antiferromagnetic coupling between the substrate and the metal center of a porphyrin, as shown for NO-MnTPP on cobalt [9]. In addition to a reduced magnitude, a reversed sign with respect to the substrate was reported for the XMCD signal at the Mn $L_{2,3}$-absorption edges. The impact of the surface-*trans* effect on the interaction sign and strength between ferromagnetic substrates and the molecular spin is also referred to as the surface spin-*trans* effect [40].

The functionalization with small gas molecules also leads to a different crystal field that is seen by the central metal ion. While a penta-coordinated ion surrounded by the four nitrogen atoms in the macrocycle and the surface is in a tetragonal pyramidal crystal field, the coordination of a sixth ligand on the top leads to a more octahedral-like crystal field. As anticipated in section 2.1, this can also affect the electronic energy levels. If the level alignment is changed such that the splitting between two levels is smaller than the spin-pairing energy, this can lead to a different magnetic ground state. Similar to the behavior of spin-crossover complexes, the energy costs of occupying two orbitals with a single electron can be lower than pairing the two formerly unpaired electrons. For NiTPP adsorbed onto cobalt (100), it was shown that a spin on-switching can be achieved by coordinating a diamagnetic NH_3 molecule (S = 0) to the open site [10]. Via a removal of the NH_3 molecules through annealing, this procedure was also shown to be reversible and repeatable (S = 0 ↔ S = 1). Without the NH_3 ligand on top, the central nickel atom is in a $(d_{xy})^2$ $(d_{yz}, d_{xz})^4$ $(d_{z^2})^2$ $(d_{x^2-y^2})^0$ configuration. The adsorption of the additional diamagnetic ligand causes an energetical upshift of the d_{z^2} level, which results in a $(d_{xy})^2$ $(d_{yz}, d_{xz})^4$ $(d_{z^2})^1$ $(d_{x^2-y^2})^1$ configuration. In terms of the total spin, this corresponds to an S = 1 configuration, as expected for a coordination number of six and an octahedral configuration [41,42].

3. The model system

Nickel tetraphenyl porphyrin (NiTPP) molecules deposited on a (100) copper surface (Cu(100)) represent a model system for studying strongly hybridized metal-organic interfaces. Upon adsorption, an unexpectedly high charge transfer takes place from the substrate to the molecule. This chapter aims to review the previously found results, which are mainly reported in [13] and [14].

3.1. NiTPP/Cu(100)

As is typical for several of the metal TPP (MTPP) molecules, NiTPP assembles in two long-range ordered rotational domains, rotated by ± 8° concerning the [001] direction of the substrate, respectively. The unit cell is commensurate with the one of the substrate, with a distance of approximately 1.27 nm between the centers of two adjacent molecules. Moreover, periodic density functional theory (DFT) calculations revealed that the nickel sits on top of a hollow site. Combined with a strong twisting and tilting of the peripheral phenyl rings [43], this enables a very small macrocycle-surface distance.

The consequences for the electronic structure were investigated by photoemission tomography [44], a well-established approach for the interpretation of momentum maps that combines experimental momentum microscopy and theoretical DFT calculations. This method will be introduced in more detail in section 4.1.1. As summarized in Figure 5, the occurrence of three valence band features upon adsorption revealed a substrate-to-molecule charge transfer that leads to the partial filling of the degenerate LUMO and LUMO+1 (LUMO/+1) and the LUMO+3 [13].

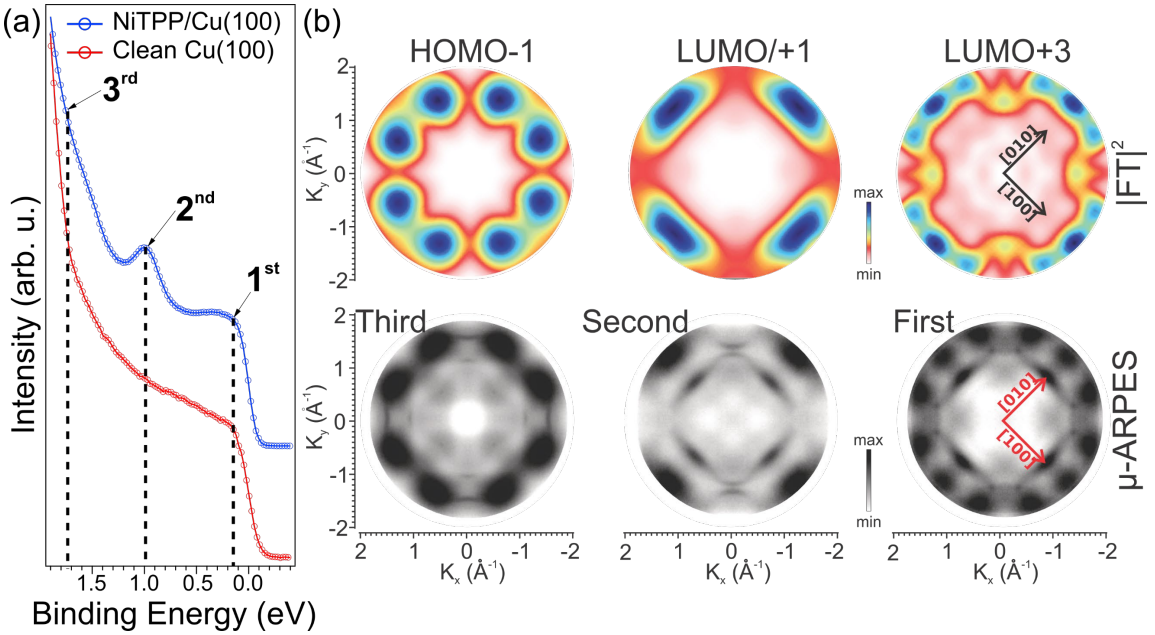

Figure 5) (a) Angle-integrated photoemission spectra of Cu(100) and NiTPP/Cu(100). After deposition of NiTPP, two features appear at binding energies around 0.15 eV and 1.0 eV. (b) In the comparison of the experimental and DFT-calculated maps a third feature can be identified and the three features can be unambiguously assigned to the HOMO-1, LUMO/+1, and LUMO+3. Figure adapted from [13].

However, no specific indication for an occupation of the LUMO+2 could be seen in the valence band as the corresponding features are located outside the experimentally probed k-space range. In contrast to the LUMO/+1 and the LUMO+3, which are mainly located at the macrocycle of the molecule, the LUMO+2 also has a significant contribution to the electron density at the central Ni ion. Therefore, its occupancy can provide insight into the oxidation state of the Ni center. To cast light on this, a comparison between the near-edge x-ray absorption fine structure (NEXAFS) spectra of a multi- and a monolayer sample was done. In a nutshell, it was shown that the LUMO+2 of the first-layer molecules gets occupied, which leads to a change of the Ni oxidation from Ni(II) in the gas-phase to Ni(I) when adsorbed on Cu(100) [14].

Thus, altogether, the exceptionally high charge transfer from the Cu(100) surface to the NiTPP molecules does not only lead to a partial filling of the molecular orbitals up to the LUMO+3 [13], but it also causes a change in the oxidation state of the central nickel atom from Ni(II) to Ni(I) [14].

3.2. Open questions

The unusually high charge transfer in combination with the self-assembly into highly ordered molecular arrays makes the NiTPP/Cu(100) interface appealing for a wide range of possible applications and offers a versatility that makes it a potential model system to emulate systems in nature. Two main questions shall be answered in this thesis to explore the implications of this charge transfer:

1. **Can the charge transfer be quenched or tuned?**

This question targets the electronic configuration of the molecule upon manipulation. As anticipated in sections 2.2 and 2.3, such manipulation can happen through the interaction with the surface or with ligands that bind to the available axial adsorption site on top of the molecule.

The first approach is to inhibit the extensive charge transfer from the Cu(100) substrate to the NiTPP molecule. The conformational and electronic modifications caused by the substrate lead to a substantial deviation of the molecule properties from its gas-phase equilibrium state. An interlayer could be a possible means of preserving the gas phase properties, e.g., the +2-oxidation state of the central nickel ion, but still to attain an ordered growth. Such a system would provide a reference for evaluating the effects of the charge transfer.

A second approach is to functionalize the molecule with a second axial ligand that binds on top of the porphyrin. Capturing trace gases, for example, can be interesting for sensing and catalytic applications in light of the ongoing climate change. As mentioned in section 2.3, the molecule-substrate interaction can be tuned via the surface-*trans* effect and the surface spin-*trans* effect. For the present system, it is particularly interesting to understand

- if the +1-oxidation state of the nickel atom is a basic requirement for its reactivity to selected gas molecules,

- how the additional electron density from the substrate affects the spin configuration in the nickel d shell, and
- if the anchoring of small gases changes the electronic configuration caused by the substrate.

2. What are the implications of the charge transfer on the thermal stability of this system?

The second question concerns the stability against the thermally induced on-surface reactions mentioned in chapter 2.2. For possible applications in sensing [45], catalysis [46], or spintronic building blocks where the molecule-substrate exchange coupling can be tuned [9,10,12], it is often required to regenerate the system. Annealing is one of the most effective ways to restore the molecular layer to its pristine configuration by removing anchored ligands that alter the activity of the catalytic center. In powders, porphyrin molecules are usually robust against thermal treatments as they can be annealed to high temperatures without changing their chemical structure. However, when deposited on a surface, the molecule-substrate interaction drastically influences the stability of the molecular film. If the interaction is weak, the molecules may desorb from the substrate before the anchored ligand has been removed or, in contrast, the substrate can accelerate the thermal decomposition of the molecular layer [47]. As it was found earlier for NiTPP/Cu(100), the charge transfer was connected to a certain conformation of the molecule and the special adsorption site [13]. How does this configuration impact the behavior upon annealing?

These questions have been tackled with an extensive set of complementary surface-sensitive techniques, which will be introduced in the next chapter.

4. Methods

The underlying concepts of the experimental techniques used in this work are summarized in this chapter. As all of these methods are well-established and extensively discussed elsewhere in the literature, only the basics that are required to understand the results of this thesis will be introduced. Every technique is followed by a description of the setup where it has been carried out. At first, the techniques based on the photoemission process, i.e., photoemission tomography (PT) and x-ray photoemission spectroscopy (XPS), are introduced. Then, techniques based on absorption due to excitation of electrons from core levels, i.e., near-edge x-ray absorption fine structure spectroscopy (NEXAFS), x-ray magnetic circular dichroism (XMCD), are discussed. After that, infrared reflection absorption spectroscopy (IRAS) will be introduced, which exploits the absorption of light in the IR regime due to the excitation of molecular vibrations. Scanning tunneling microscopy (STM), which relies on the tunneling of electrons from (to) the surface to (from) the tip, will be discussed subsequently. Finally, the chapter will be closed with a brief description of the data treatment in the analysis of the NEXAFS, XPS, and XMCD results.

4.1. Photoemission spectroscopy

Photoemission spectroscopy is a well-established and widely employed tool for investigating the electronic properties of metal-organic interfaces [7,48,49]. The basic principle of this technique relies on the photoelectric effect: a photon impinging on the sample excites an electron by the photoelectric effect, which leaves the sample and is then analyzed with respect to its kinetic energy E_{kin} and its momentum $\vec{p}$. Obeying the energy conservation, the kinetic energy of the photoemitted electron is

$$E_{\mathrm{kin}} = h\nu - \Phi - E_{\mathrm{B}}, \tag{1}$$

where $h\nu$ is the photon energy, Φ the work function of the sample, and E_{B} the binding energy of the emitted electron [50]. In an experiment, the resulting photocurrent is measured in dependence on the kinetic energy E_{kin} using an electron analyzer. The photon energy has to be chosen in accordance with the binding energy range of the electronic levels to be investigated. While valence band states are typically measured with UV light to enhance the photoemission cross section, x-ray light is required for core levels. These disciplines are generally referred to as ultraviolet photoemission spectroscopy (UPS) or valence band spectroscopy and XPS, respectively.

In the simplest approach, the photoemission process can be described in the one-electron picture for the initial- and final-state wave function. A very comprehensive approximation for the description is the so-called three-step model. In this model, the photoemission process is described as three subsequent steps: excitation from the initial ground state of the system to an unoccupied final state, propagation of the electron to the surface, and the electron's escape into the vacuum. The contribution of each step to a photoelectron spectrum is illustrated in Figure 6.

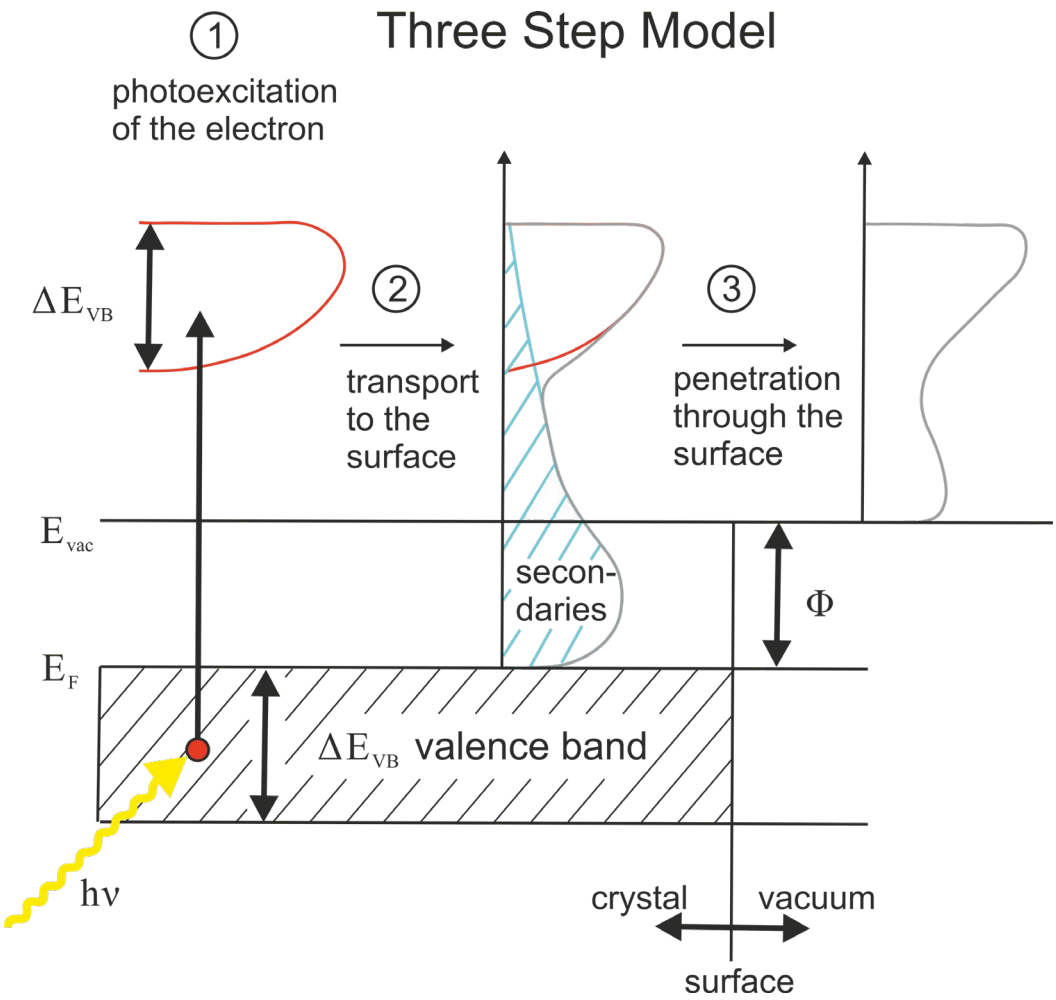

Figure 6) The photoemission process divided into three steps: (1) the excitation from an initial to a final state, (2) the transport to the surface giving rise to a background of inelastically scattered electrons and (3) the escape from the surface cutting off the low kinetic energy secondaries. Figure adapted from [50].

First, an electron from the initial state $|i\rangle$ is excited to a final state $|f\rangle$ by a photon with the energy $h\nu$. The transition probability per unit time $\omega_{i\to f}$ can be described by Fermi's golden rule [50]

$$\omega_{i\to f} \propto \frac{2\pi}{\hbar}\underbrace{|\langle f|\Delta|i\rangle|^2}_{M_{i\to f}}\times \delta(E_\mathrm{f}-E_\mathrm{i}-h\nu), \qquad (2)$$

where E_f and E_i are the energies of the final and initial state, respectively, and Δ is a small, time-dependent perturbation. For the photon energies used in this work, the perturbation Δ, which describes the interaction of the electron and the electromagnetic field, can be written in the so-called dipole approximation leading to

$$M_{\mathrm{i}\to\mathrm{f}} = |\langle f|\Delta|i\rangle| \approx \left|\langle f|\overrightarrow{A_0}\cdot\vec{p}|i\rangle\right|. \qquad (3)$$

Here, $\overrightarrow{A_0}$ is the vector potential describing the monochromatic radiation and $\vec{p}$ is the momentum operator of the photoelectron. By evaluating the combinations of initial and final states that lead to a non-zero transition matrix element in equation (2), the so-called dipole selection rules can be formulated. They can be used to infer the symmetry of the states involved in direct transitions [50].

In the second step, the electron propagates to the surface. For typical kinetic energies, the electron has a relatively short mean free path in solids and might undergo different scattering processes. During these processes, the information about their original initial state gets lost. The electrons that still have enough kinetic energy to leave the sample will lead to a background of secondary electrons at the low kinetic energy side.

In the third step, the electron overcomes the surface barrier and escapes into the vacuum. Here, the out-of-plane component (i.e., the one perpendicular to the surface) of the electron momentum is reduced, while the in-plane component is preserved. This is described as a consequence of the symmetry breaking in the direction perpendicular to the surface. As a result, the perpendicular component of the photoelectron momentum can be only empirically determined, whereas the parallel component can be directly determined from the kinetic energy and the polar emission angle [51].

Even though the three-step model is sufficient for the description of a wide range of phenomena, the decomposition into three separate incoherent steps is not always appropriate [52]. In this case, the one-step model, in which the three abovementioned steps are described as a single quantum-mechanical process, is more accurate [53].

4.1.1. Photoemission tomography

Photoemission tomography (PT) is a combined approach consisting of photoemission spectroscopy and density functional theory. In this technique, the Fourier transformed electron densities obtained by DFT are used to characterize the features of momentum maps and understand the chemical structure of molecular adsorbate systems [13,54]. Under certain assumptions [44], the molecular orbitals are visible in the valence band spectrum of molecule-single crystal interfaces, representing a fingerprint of a specific state. Exploiting this, PT has already been used to follow on-surface reactions. For example, Yang *et al.* identified reaction intermediates providing a tool for the analysis of reaction pathways [55]. This method has also been shown to be useful to gain insight into dehydrogenation reactions of porphyrins adsorbed on metal substrates [56].

By using equation (3), the photoemission current can be written as the sum over all initial state wave functions $|\Psi_i\rangle$ to the final state $|\Psi_f\rangle$ which is characterized by the direction and the kinetic energy of a photoemitted electron [44]

$$I(k_x, k_y; E_{\text{kin}}) \propto \sum_i \left|\langle \Psi_f(k_x, k_y; E_{\text{kin}}) | \overrightarrow{A_0} \cdot \vec{p} | \Psi_i \rangle\right|^2 \times \delta(E_{\text{f}} - E_{\text{i}} - h\nu), \qquad (4)$$

where k_x and k_y are the parallel momentum components. In momentum microscopy, the parallel k-components are obtained directly; whereas, in angle-resolved photoemission spectroscopy, a conversion of the angles is required [57]. Under certain conditions, the final state can be treated as a free electron plane wave $|\Psi_f\rangle = C\, exp(-i\vec{k}\vec{r})$ so that the matrix can be written as $M_{i\to f} \propto \overrightarrow{A_0} \cdot \vec{k} \langle \Psi_f | \Psi_i \rangle$ or

$$M_{i\to f} \propto \left(\overrightarrow{A_0} \cdot \vec{k}\right) \int_{-\infty}^{\infty} \Psi_i \, exp\left(i\left(\vec{k} \cdot \vec{r}\right)\right) d^3 r, \qquad (5)$$

which is the Fourier transform of the initial state. From theoretical considerations, the plane-wave final-state assumption can be expected to be valid for (i) π orbital emissions from large planar molecules, (ii) an experimental geometry in which the angle between the polarization vector $\overrightarrow{A_0}$ and the direction of the emitted electron $\vec{k}$ is rather small, and (iii) molecules consisting of many light atoms (H, C, N, O) [58]. Exploiting this, equation (4) can be rewritten so that for a fixed energy, it holds that

$$\left|\left(\mathcal{F}(\Psi_i)\right)(\vec{k})\right| \propto \frac{\sqrt{I_i(k_x,k_y)}}{\left|\overrightarrow{A_0}\cdot\vec{k}\right|}. \tag{6}$$

With this expression, it becomes clear that the experimental photoemission intensity is proportional the square modulus of the Fourier transform of the initial state wave function $|\Psi_i\rangle$,

$$I(k_x,k_y) \propto \left|\overrightarrow{A_0}\cdot\vec{k}\right|^2 \times \left|\left(\mathcal{F}(\Psi_i)\right)(\vec{k})\right|^2. \tag{7}$$

As the factor $\left|\overrightarrow{A_0}\cdot\vec{k}\right|$ depends on the experimental geometry, its square value can be calculated [59]. Therefore, the Fourier transform of the initial state can be used to reproduce (except for a phase) the experimental intensities within this approximation. In Figure 7, this is illustrated for the HOMO of a pentacene molecule from the proof-of-concept work for PT published by Peter Puschnig *et al.* in 2009 [44].

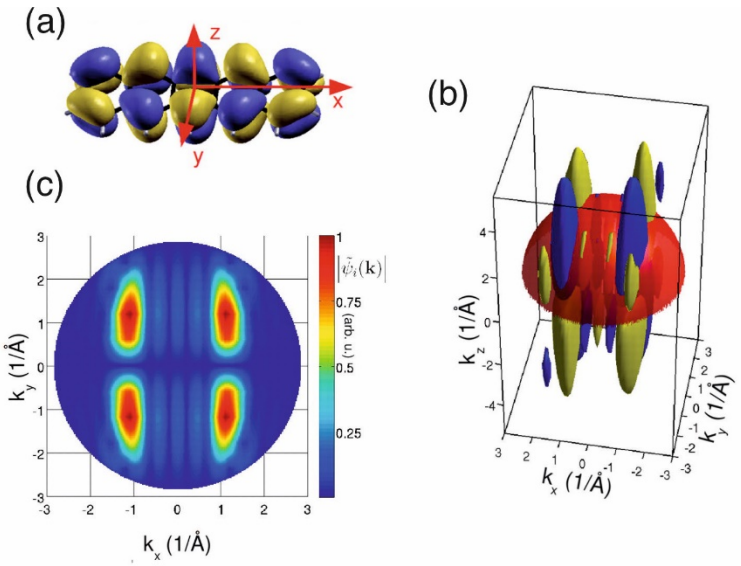

Figure 7) (a) Isosurface of the HOMO of pentacene calculated by DFT, (b) Fourier transform of (a). The red sphere is the energy for a free electron final state with a kinetic energy of 29.8 eV. (c) shows the absolute value of the Fourier transformed HOMO in (b) evaluated on the red sphere projected onto a plane. Figure adapted from [44]. Reprinted with permission from AAAS.

NanoESCA beamline

The so-called momentum maps $I(k_x,k_y;E_{\mathrm{kin}})$ and the momentum-integrated valence band photoemission spectra $I(E_{\mathrm{kin}})$ were mainly measured at the NanoESCA beamline of the Elettra synchrotron in Trieste, Italy. The endstation consists of an ultra-high vacuum (UHV) setup with a commercially available NanoESCA photoelectron emission microscope

(PEEM) described in [60] and a separated chamber for *in-situ* preparation. Generally, the microscope can be operated in a direct and a momentum imaging mode. However, in this work, only momentum maps were collected to analyze the photoemission intensity in a lateral reciprocal space range of $k_x, k_y \in [-2.1, 2.1]$ Å^{-1} for a kinetic energy range of a few electronvolts below the Fermi level. The maps were collected with p-polarized light with a photon energy of 35 eV. By keeping the sample at a constant temperature of 90 K, a total energy resolution of 70 meV was achieved.

4.1.2. XPS

While PT is performed with photon energies in the UV regime and is sensitive to electronic states in the valence band with a delocalized character, XPS investigates the electronic structure of the more localized core levels. This leads to a flat dispersion in the reciprocal space and thus sharp features in energy. As the binding energies of core levels depend on the Coulomb potential of the corresponding core, they are highly element-specific, and peaks can usually be assigned to the related elements. Moreover, multiple chemical environments of a certain element within a molecule or an alloy can lead to different changes in the binding energies of a specific core level, commonly referred to as chemical shifts. For this reason, this technique, developed starting from 1957 by Siegbahn *et al.* [61], is also called electron spectroscopy for chemical analysis (ESCA).

Several interesting phenomena have been identified for on-surface porphyrins in the past. Generally, they can be related to initial state effects, final state effects, or a combination of both.

An example of an initial state effect is the transformation of the N 1*s* spectrum metalation of free-base porphyrins. While in 2HTPP, the N atoms are in two different chemical environments, i.e., pyrrolic (-NH-) and iminic (=N-), giving rise to two separate components, metalation leads to four chemically equivalent N atoms resulting in one single feature in the N 1*s* spectrum. This was observed, for example, after post-deposition of nickel [62] or annealing-induced self-metalation with surface atoms [18]. As another instance for an initial state effect, XPS can also indicate changes in the oxidation state of the central metal ion in porphyrins. Even though the absolute oxidation state cannot be reliably determined by XPS alone, peak shifts towards lower binding energies can indicate a reduction of the element under investigation. This was observed, for example, at the CoTPP/Ag(111) interface. In this system, a strong charge transfer from the substrate to the molecule causes a significant Co $2p_{3/2}$ core-level shift, suggesting a reduction of the central Co ion [63].

A final state related change in the XPS spectrum was observed during the dehydrogenation of C atoms of CuTPP. The stepwise dehydrogenation led to a rotation of the phenyl rings resulting in a more parallel configuration of the peripheral substituents to the macrocycle plane [64]. The closer proximity to the surface results in an enhanced final state screening [64]. As a consequence, a shift towards lower binding energies of the corresponding C 1*s* component was observed.

The XPS measurements in this work were carried out at the ALOISA beamline of the Elettra Synchrotron in Trieste, Italy. The beamline will be introduced at the end of section 4.2.1.

4.2. Absorption spectroscopy

Another commonly used class of techniques in the investigation of metal-organic interfaces is based on the absorption of photons. Here, the kind of information one can gain depends on the employed photon energy and the polarization of the light. The present work will first discuss NEXAFS and XMCD, where the absorption of light in the x-ray regime is measured. In this regime, the absorption is mainly caused by electronic excitations from core levels to states above the Fermi level. The subsequent section discusses IRAS, where the absorption of light in the infrared regime, caused by vibronic excitations, is detected.

4.2.1. NEXAFS

In general, the intensity of an electromagnetic wave that propagates over a distance z through matter decays exponentially and can be written, equivalent to the Beer-Lambert law, as

$$I(z) = I_0\, exp(-\mu(E)z). \tag{8}$$

Here, I_0 is the intensity of the unattenuated light and $\mu(E)$ is the total attenuation coefficient of the material that can be written as

$$\mu(E) \propto \frac{\rho Z^4}{mE^3}, \tag{9}$$

where Z and m are atomic number and mass respectively. As in the soft x-ray regime, the main cause for the attenuation is absorption due to excitation or even ionization of an atom, the total attenuation coefficient approximately equals the photoelectric absorption coefficient in this regime [65]. This photoelectric absorption coefficient is proportional to the absorption cross section σ_x. σ_x is defined as the number of excited atoms per unit time divided by the number of incident photons per unit time and area, and it generally decreases with increasing photon energies. When the photon energy is close to the ionization energy of a certain core level, the absorption cross section increases abruptly, giving rise to a so-called absorption edge.

It can be seen in Figure 8 that the different edges also possess a fine structure due to the spin-orbit interaction.

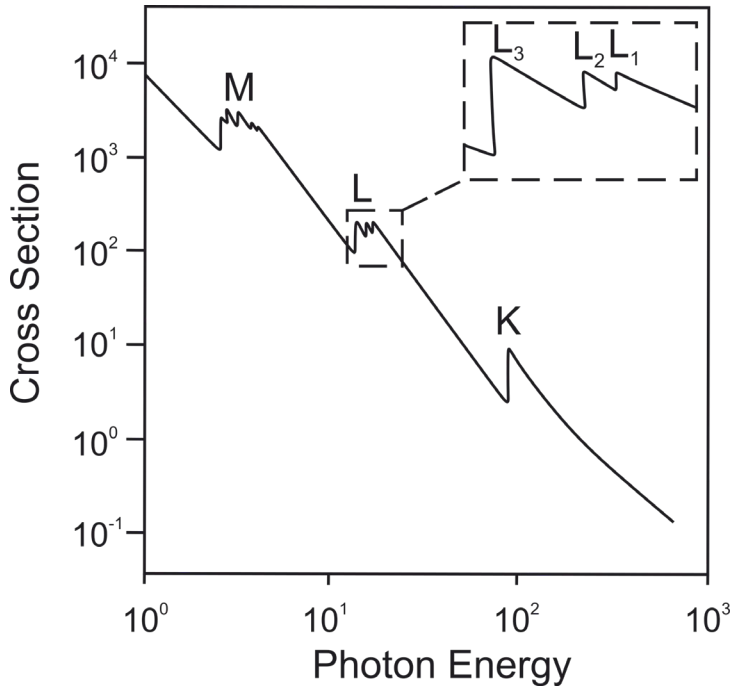

Figure 8) X-ray absorption cross section in an energy range containing K-, L-, and M-absorption edges. Figure adapted from [184].

In the commonly accepted notation, the edges are labeled with a capital letter associated with the principal quantum number followed by a subscript denoting the corresponding fine structure level. As the capital letters are alphabetically ordered starting from K and the subscript is an integer ascending with the binding energy of the core level beginning from one, the absorption edge that is caused by an electron excitation from the $2p_{3/2}$ core level is denoted as L_3-edge, for example.

In NEXAFS, the fine structure near an absorption edge caused by the excitation of electrons from core levels to unoccupied or partially occupied bound states close to the Fermi level measured with linearly polarized light is investigated. Staying in a one-electron picture, the transition probability for such an event follows the previously introduced relation (2). Moreover, the dipole approximation (3) holds for typically used photon energies in the range of 150 to 2000 eV. From these relations, it is clear that the two main parameters that determine the transition probability and, therefore, the absorption intensity are (1) the photon energy (included in the form of the Dirac delta function $\delta(E_\mathrm{f} - E_\mathrm{i} - h\nu)$) and (2) the orientation between the vector potential $\overrightarrow{A_0}$ (which, in the case of an electromagnetic plane wave, is collinear with the electric field vector $\vec{E}$) and the linear momentum operator $\vec{p}$.

First, we will discuss a typical photon energy dependence of the absorption probability for adsorbed molecules. For probing the energetic structure, the absorption in a range starting from a few electron volts below the ionization edge up to around 30-50 eV above it is measured [66]. When the photon energy crosses a resonance, i.e., when $h\nu$ equals the energy difference of an occupied and an unoccupied state, another absorption channel opens up, and electrons are resonantly excited. Thus, in contrast to photoemission

spectroscopy, NEXAFS gives access to the unoccupied states. The origin of different features, which can typically be found in a NEXAFS spectrum of diatomic molecules, is shown in Figure 9. Starting from low photon energies, the first absorption peak typically is a π^* feature, i.e., an empty bound molecular state with a π symmetry. When the photon energy approaches the ionization energy, Rydberg states can be observed. At the ionization threshold, a step-like feature is visible due to the excitation of core electrons to the quasi-continuum of final states. In reality, however, the Rydberg states often overlap with the step function at the ionization energy [67]. For a neutral molecule, σ^* states are typically above the ionization edge and, therefore, are superimposed to the continuum of final states.

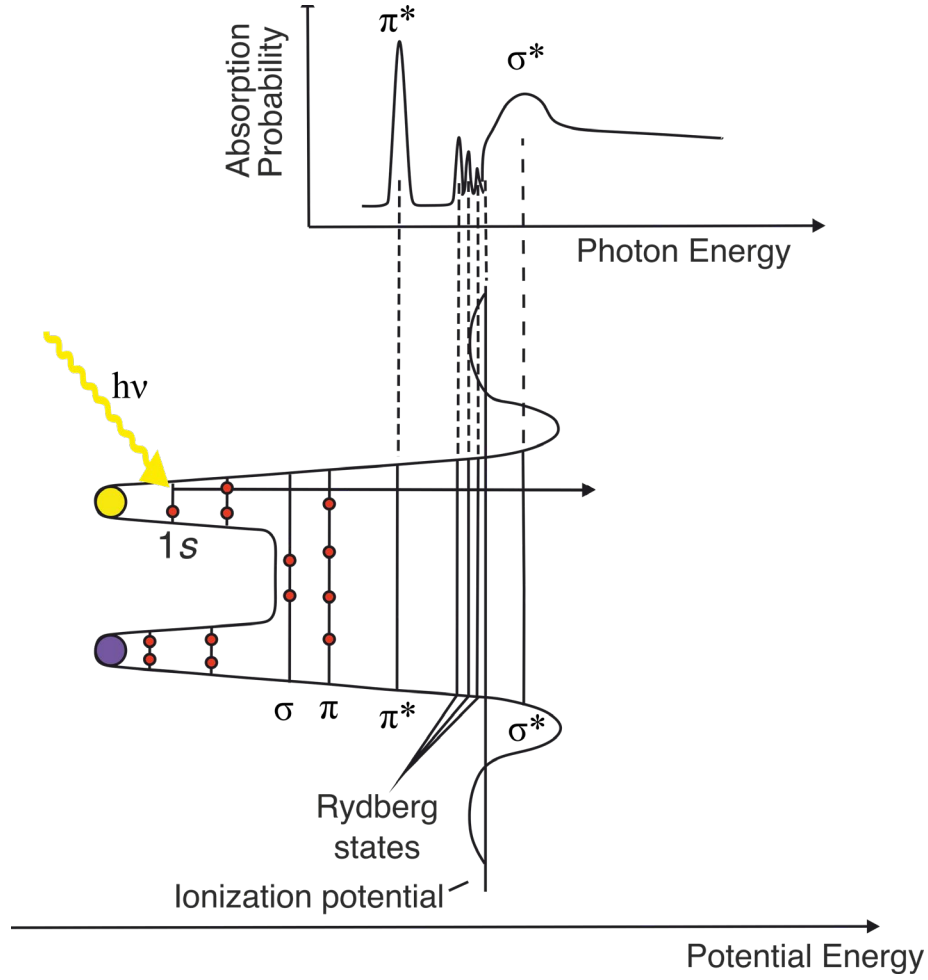

Figure 9) Schematic diagram of the origins of typical features in a NEXAFS spectrum of molecules. Figure adapted from [67].

In addition to the energetic order probed by the photon energy, the orientation of specific molecular orbitals can be probed by NEXAFS, as they have a strong directional character [68]. This can easily be seen in the transition intensity for a K-edge excitation, which is the case for most of the measurements shown in this work. Using linearly polarized light, we can write the general transition intensity $I_{i\to f}$ as proportional to equation (2) in the dipole-approximation (3) [67].

$$I_{\mathrm{i\to f}} \propto \left|\langle \Psi_f | \overrightarrow{A_0} \cdot \vec{p} | \Psi_i \rangle\right|^2 \propto \left|\overrightarrow{A_0} \cdot \langle \Psi_f | \vec{p} | \Psi_i \rangle\right|^2. \tag{10}$$

Under the assumption of a 1s initial state $|i\rangle = |i_{1s}\rangle$, the matrix element points in the direction of the final state orbital $\vec{O}$ and the transition intensity becomes

$$I_{\mathrm{i}\to\mathrm{f}} \propto \left|\overrightarrow{A_0}\langle\Psi_f|\vec{p}|\Psi_{1s}\rangle\right|^2 \propto \left|\overrightarrow{A_0}\cdot\vec{O}\right|^2 \propto cos^2(\delta), \tag{11}$$

where δ is the angle between the polarization $\overrightarrow{A_0}$ and the axis of the final state orbital $\vec{O}$ [67]. As a result, the absorption intensity will be maximal when the electric field vector of the perfectly linearly polarized light is parallel to the axis of the final state orbital and minimal in all directions perpendicular to the final state orbital. This behavior is sometimes referred to as the searchlight effect [69]. For the approximation of a perfectly planar, π-conjugated molecule with pure σ*(π*)-type orbitals aligned within (perpendicular to) the molecular plane, the absorption due to excitation will be maximal for perfectly s-polarized (p-polarized) light. The designation of s- and p-polarization has its origin in the orientation of the electric field vector with respect to the plane of incidence: while for s-polarization (from "*senkrecht*", German for perpendicular), the electric field vector is perpendicular to the plane of incidence, it is parallel to the plane of incidence for p-polarization. For a grazing incidence angle (close to 90° from the sample surface plane), one can also derive the tilt angle γ of approximately planar molecules with the relation [70]

$$\frac{I_\mathrm{p}}{I_\mathrm{s}} \propto tan^2(\gamma). \tag{12}$$

ALOISA beamline

The NEXAFS and XPS measurements in this work were carried out at the ALOISA (Advanced Line for Overlayer, Interface and Surface Analysis) beamline of the Elettra Synchrotron in Trieste, Italy. Only the basic setup will be introduced here as the beamline and end station are described in [71] and updated information, including technical upgrades, can be found in [72]. ALOISA offers the possibility for photoemission and absorption spectroscopy experiments with photon energies ranging from 130 to 1500 eV. The beamline is equipped with a combination of electron spectrometers which are mounted on rotatable frames, enabling a wide range of experimental geometries. *In-situ* sample preparation is possible in a separate preparation chamber equipped with a sputter gun, sample heating stage, and evaporators.

The XPS measurements were performed with quasi p-polarized light. In this configuration, the sample plane is perpendicular to the storage ring plane and is tilted by 4° to the propagation direction of the incoming light. The photoelectrons were detected in normal emission with a total energy resolution of the analyzer and the beamline of approximately 300 meV.

In the NEXAFS measurements, the surface orientation vis-à-vis the linear polarization was changed by rotating the sample around the beam axis. In this way, the electric field vector is either parallel to the surface plane (perpendicular to the plane of incidence, i.e., s-polarization) or almost perpendicular to the surface plane with an angle of 6° to the surface normal. The absorption is measured in a partial electron yield mode by collecting the Auger electrons with a channeltron multiplier and screening low-energy secondaries with a grid on a negative potential.

4.2.2. XMCD

XMCD is a powerful tool to probe the magnetic configuration of specific elements. While in NEXAFS, the absorption intensity mostly depends on the photon energy and the relative orientation of light polarization and sample, XMCD exploits the fact that the absorption process of circularly polarized light is spin-dependent [73]. Therefore, it is possible to probe imbalances of unoccupied states with different spin polarizations.

First, the XMCD effect will be explained in a one-electron picture with the example of the L_3 and L_2 absorption edges. As the magnetic and chemical properties of $3d$ metals are mainly determined by the electronic configuration of the $3d$ shell, the $L_{2,3}$-edges are commonly investigated for transition metal complexes. In a second step, the so-called sum rules will be introduced, using which quantitative information about the magnetic moment of an atom is obtained.

For understanding the dependence of the absorption intensity on the light polarization, the transition matrix element from (3) will be discussed now. For easier visualization, it is convenient to rewrite the equation by applying the commutator relation $[H_0, \vec{r}] = \frac{-i\hbar}{m_e}\vec{p}$ to

$$M_{\mathrm{i}\to\mathrm{f}} \propto \langle \Psi_f | \overrightarrow{A_0} \cdot \vec{r} | \Psi_i \rangle \propto \langle \Psi_f | \vec{\epsilon} \cdot \vec{r} | \Psi_i \rangle, \tag{13}$$

where $\vec{\epsilon}$ is the unit vector of the vector potential $\overrightarrow{A_0}$. The operator $\vec{\epsilon} \cdot \vec{r}$ is generally called dipole operator [73]. For the direction $\alpha \in (x, y, z)$ and the photon angular momentum, $\pm q\hbar$ for right and left circularly polarized light, it will be referred to as

$$P_\alpha^q = \overrightarrow{\epsilon_\alpha^q} \cdot \vec{r}. \tag{14}$$

In non-atomic systems, i.e., solids or molecules, the wavefunction can be written as a linear combination of atomic wavefunctions. Therefore, a simple and useful approach to evaluate (13) in the one-electron picture is to write the core electron wavefunction $|i\rangle$ and the valence electron wavefunction $|f\rangle$ as atomic spin orbitals of the form [73]

$$R_{n,l}(r) Y_{l,m_l}(\Theta, \Phi) \chi_{s,m_s} = \left| R_{n,l}(r); l, m_l, s, m_s \right\rangle. \tag{15}$$

Here, $R_{n,l}(r)$, Y_{l,m_l}, and χ_{s,m_s} are the radial part, spherical harmonics, and spin wavefunction respectively. With $|i\rangle = \left| R_{n,c}(r); c, m_c, s, m_s \right\rangle$ and

$|f\rangle = \left| R_{n',l}(r); l, m_l, s, m'_s \right\rangle$, the matrix element factors to

$$\langle \Psi_f | P_\alpha^q | \Psi_i \rangle = \underbrace{\delta(m'_s, m_s)}_{\text{spin}} \underbrace{\langle R_{n',l}(r) | R_{n,c}(r) \rangle}_{\text{radial}} \underbrace{\sum_{m_c, m_l, p} e_{\alpha,p}^q \left\langle l, m_l \middle| C_p^{(1)} \middle| c, m_c \right\rangle}_{\text{angular}}, \tag{16}$$

where $C_p^{(1)} = \sqrt{\frac{4\pi}{2l+1}} Y_{1,m}(\Theta, \Phi)$ is the Racah operator for $l = 1$ and $e_{\alpha,p}^q$ are imaginary coefficients [73]. As the dipole operator does not act on the spin, only the radial and angular parts must be considered.

The treatment of the radial part reveals that there is an $R_{\mathrm{core}} R_{\mathrm{valence}} r^3$ dependence, which results in a strong confinement of allowed transitions to small distances to the atomic center and explains the high element-specificity.

From an analysis of the angular part, it gets clear that combinations of l, m_l, q, c, m_c for nonvanishing matrix elements all fulfill

$$\begin{aligned} \Delta l &= l' - l = \pm 1, \\ \Delta m_l &= m_l - m_c = q, \\ \Delta s &= s' - s = 0, \text{ and} \\ \Delta m_s &= m_s' - m_s = 0. \end{aligned} \tag{17}$$

As tightly bound states with the same orbital momentum l but different total angular momentum j are well separated by spin-orbit coupling (10-100 eV for transition metals [73], 440-1100 eV for rear earth elements [74]), the edges due to absorption with a net parallel or antiparallel coupling of l and s can be easily resolved experimentally.

The spin-dependent excitation process from spin-split levels can be visualized as a two-step process. In the first step, the photon angular momentum is transferred to the angular momentum of the excited electron. Due to spin-orbit coupling, the excited electrons also gain a spin polarization in this process. In the second step, the spin polarization of the unoccupied final states, i.e., a density of states (DOS) in the case of a transition metal, serves as a "detector" [73]. Since the transition rate depends on the number of available final states with a spin aligned parallel to the spin of the photoexcited electrons, differences in the DOS of unoccupied states lead to different transition probabilities for spin-up and spin-down photoelectrons. Thus, if the spins are aligned due to exchange field splitting in a ferromagnet or an applied external magnetic field, the DOS for each unoccupied spin polarization can be probed by changing the relative orientation of the magnetic moment and the photon angular momentum. As the XMCD is proportional to $cos\left(\measuredangle(\overrightarrow{L_{\text{ph}}}, \vec{m})\right)$, the effect is maximal for a collinear alignment of the photon angular momentum $\overrightarrow{L_{\text{ph}}}$ and the sample magnetization $\vec{m}$. A measurement of the dichroism by absorption measurements with two different photon helicities is illustrated in Figure 10.

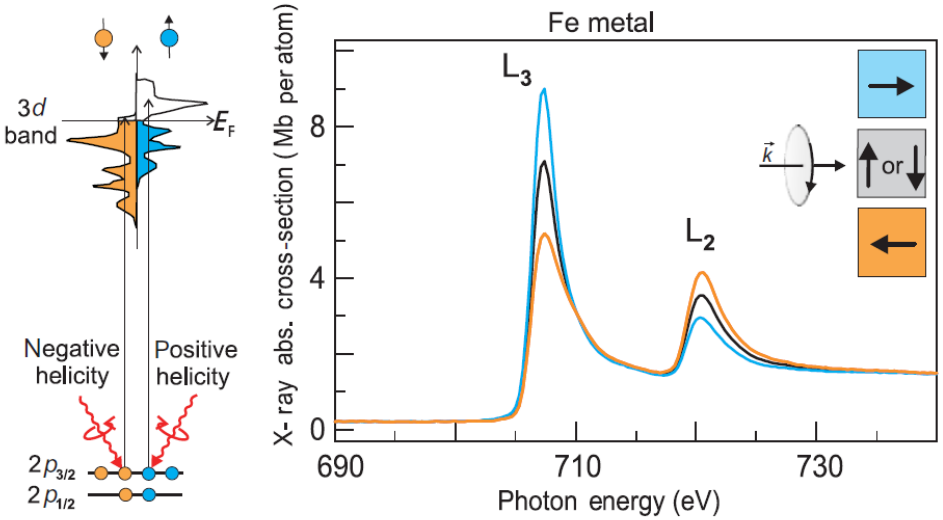

Figure 10) Illustration of the photoexcitation process with two different photon helicities: right circularly polarized light (RCP, $\overrightarrow{L_{\text{ph}}} \propto \vec{k}, |\overrightarrow{L_{\text{ph}}}| = \hbar$) and left circularly polarized light (LCP, $\overrightarrow{L_{\text{ph}}} \propto -\vec{k}, |\overrightarrow{L_{\text{ph}}}| = -\hbar$). As the spin-orbit coupling is different at the L_3- and L_2-edge, the spin polarization is different at the two edges for the same photon helicity. After changing the photon helicity the effect is reversed. Figure reproduced from [73].

So far, it has been qualitatively shown that a spin dependence of the absorption process can be achieved by changing the relative orientation of the magnetic moment and the photon angular momentum. However, by integrating over the XMCD signal of a given spin-orbit split pair of edges, it is even possible to experimentally determine the expectation values of the orbital magnetic moment as shown by Thole *et al.* [75]. Carra *et al.* also calculated the effective spin moment to the intensities of an XMCD experiment [76]. These relations are referred to as the XMCD sum rules and can be formulated as

$$m_l = -2\langle n_h \rangle \frac{\int_{L_3+L_2} I_+ - I_-}{I_{\text{iso}}}, \tag{18}$$

$$m_{s,\text{eff}} = -\frac{3}{2}\langle n_h \rangle \frac{\int_{L_3} I_+ - I_- - 2\int_{L_2} I_+ - I_-}{I_{\text{iso}}}. \tag{19}$$

Here, $\langle n_h \rangle$ is the number of empty valence states, L_2 and L_3 denote the integration ranges, and $I_\pm$ is the absorption intensity of right and left circularly polarized light, respectively. I_{iso} is the isotropic XAS intensity which, for a three-dimensional crystal with three principal axes that are orthogonal to each other, is the absorption intensity with a light polarization alongside the three main directions in a crystal x, y, and z. As this value is experimentally not accessible, it is often approximated by assumptions depending on the symmetry of the investigated system [77,78] as described in more detail in section A.1.

The effective spin moment

$$m_{s,\text{eff}} = m_s - 7\langle T_\Theta \rangle \tag{20}$$

deviates from the magnetic spin moment m_s by the so-called magnetic dipole term $7\langle T_\Theta \rangle$. This value accounts for the anisotropic spatial distribution of the spin density and, therefore, is zero only in certain symmetries (e.g., the symmetry point group O_h, illustrated in Figure 3) and without spin-orbit coupling [76]. Hence, this value must be known or theoretically approximated to calculate the magnetic spin moment m_s [79,80]. This is discussed in more detail in section A.2.

X-Treme beamline

The XMCD experiments in this work have been performed at the X-Treme beamline, located in the Swiss Light Source at the Paul-Scherrer Institut in Villigen, Switzerland [81]. The absorption was measured in a total electron yield mode (TEY), i.e., by measuring the drain current of the sample. The difference in absorption of circularly polarized x-ray light with opposite helicities (μ_+ and μ_-) was evaluated at the L_3 and L_2 absorption edges to check for a spin-polarization of the empty states. A magnetic field of 6.8 T was applied parallel to the light propagation to maximize the signal, and the sample was rotated to measure the absorption with normal ($\Theta = 0°$) and grazing ($\Theta = 70°$) incidence. To measure hysteresis, it is approximated that the difference signal at the L_3-edge is proportional to the total integrated XMCD signal. The TEY was measured at a photon energy close to the absorption maximum at the L_3-edge and at an energy at which the pre-edge lies in order to account for the background. These values were measured at external magnetic fields ranging from -6.8 to 6.8 T and back from 6.8 to -6.8 T for both polarizations. The hysteresis curve is then obtained by calculating the difference of the background-corrected absorption of left- and

right-hand circularly polarized light. The sample was cooled through a pumped ^{4}He cryostat and was kept below an estimated upper limit of around 3 K.

4.2.3. IRAS

Infrared spectroscopy (IR) is a set of techniques that, in different experimental variants, exploit the absorption of infrared light (500 to 4000 cm^{-1}). In this regime, absorption is mainly caused by the excitation of molecular vibrations. As such transitions are possible only if the excitation causes a change in the dynamic dipole moment of the molecule, the transition probability is determined by the symmetry of the investigated molecule. Thus, IR spectroscopy is a valuable tool to examine the constitution of molecules, inter- and intramolecular interactions, and the interaction of adsorbed molecules with a substrate [82].

Among the different types of IR spectroscopies, infrared reflection-absorption spectroscopy (IRAS) is a particularly surface-sensitive variant. In this technique, the absorption of linearly polarized light is measured, which penetrates an adsorbate, gets reflected at the substrate surface, and penetrates the adsorbate a second time. A special experimental arrangement, where gas dosers and evaporators point toward the sample, enables *in-situ* measurements, e.g., during a gas uptake or evaporation process.
To understand the benefits of IRAS in the investigation of metal-organic interfaces, it is important to discuss the reflection of an IR beam at a clean metal surface, as shown in Figure 11 (a). The incoming light, which can be seen as a superposition of a p- and an s-polarized component, hits the sample under a highly grazing angle ($\Phi = 88°$) to enhance the surface sensitivity. During the reflection at the sample surface, the s- and p-polarized components experience different angle-dependent phase shifts, as shown for a metal surface

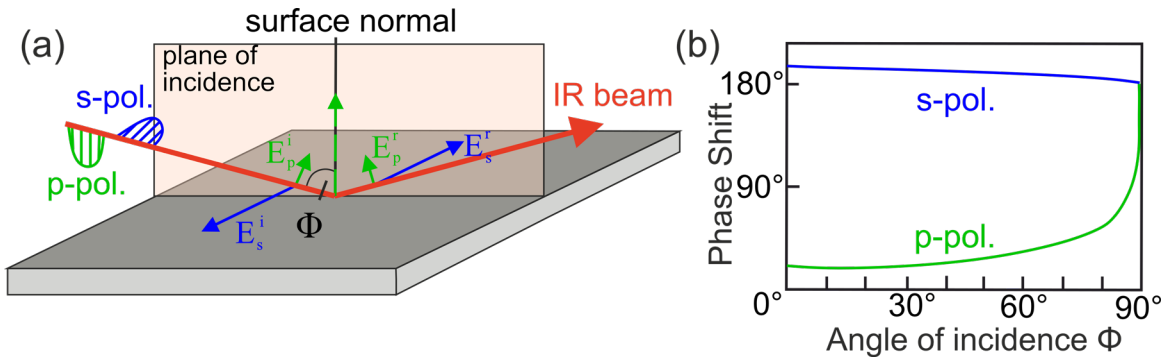

Figure 11) (a) Geometry of an IRAS experiment including the different polarization components (p and s) of the IR beam before and after the reflection on a clean metal surface. (b) Phase shifts of the p- and s-component of the linearly polarized light depending on the angle of incidence. Figure adapted from [82].

in Figure 11 (b). For angles close to $\Phi = 90°$, the p-polarized component undergoes a phase-shift of approximately 90°. In contrast, the s-polarized component undergoes a phase-shift of around 180°, almost independent of the angle of incidence. This behavior has consequences for the electric field close to the surface. For the p-component, this leads to constructive interference of the incoming (E_p^i) and the reflected (E_p^r) beam and, therefore, an enhancement of the electric field component perpendicular to the sample plane E_p^{i+r}.

Instead, for the s-components of the incoming (E_s^i) and reflected (E_s^r) beams, it leads to destructive interference of the beam and, thus, an extinction of the electric field component parallel to the surface plane.

In the next step, we include adsorbed molecules in the description. When a molecule is deposited onto a metal surface, instantaneous polarization effects due to induced charges in the free electron gas of the metal lead to a compensation of the dipole charge at the surface [83]. Accordingly, this induced "image dipole" in the substrate depends on the total dipole moment of the adsorbate. Generally, a molecular dipole oriented parallel to the surface is compensated by a dipole in the metal. This compensating dipole is parallel to the surface, too, but has the opposite orientation. A molecular dipole that is oriented perpendicularly to the sample plane causes another perpendicularly oriented dipole in the surface with an identical orientation. As the long-range electromagnetic field of the radiation interacts with the sum of the molecular and the induced image dipole moment, they cancel out for a parallel orientation and sum up for a perpendicular orientation vis-à-vis the surface plane. Consequently, the absorption intensity for a molecular dipole oriented perfectly parallel to the surface is zero, while it is doubled for a molecular dipole oriented perpendicular to the surface. More generally, the absorption intensity for a dipole moment $\overrightarrow{\mu_{mol}}$ oriented with an angle Θ to the surface normal can be written as proportional to $|2|\overrightarrow{\mu_{mol}}|\,cos(\Theta)\,|^2$, as shown in Figure 12.

Both of the effects mentioned above, i.e., the extinction of the p-polarized light component due to a phase shift at the metal substrate and the cancellation of the effective dipole moment due to an emerging image dipole, have the consequence that the absorption intensity is only different from zero if the excited vibration has a component perpendicular to the surface. Together, they are commonly referred to as the metal surface selection rule (MSSR) [84].

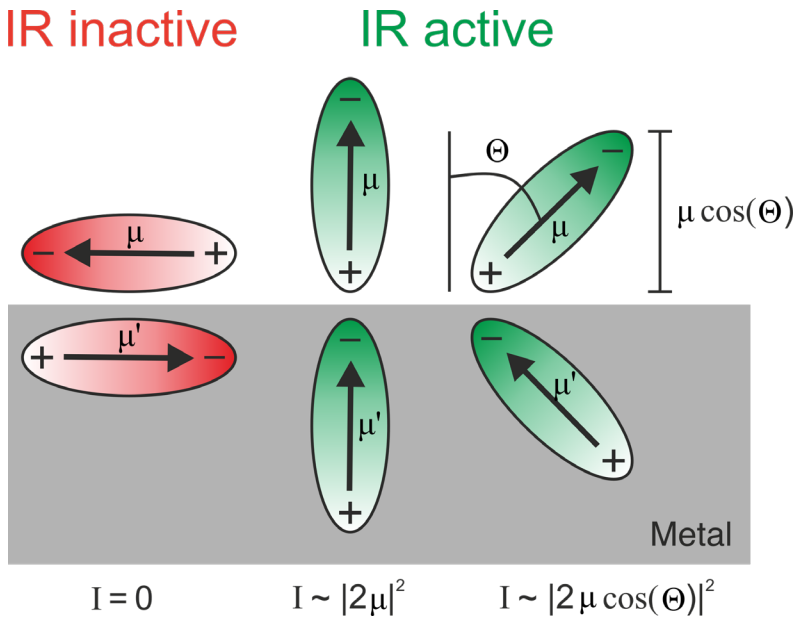

Figure 12) Different orientated molecular dipoles on top of a metal surface and the corresponding induced image dipole moments in the metal. Figure adapted from [185].

Experimental setup

The IRAS measurements were carried out at the Friedrich-Alexander-University Erlangen-Nuremberg, in the facilities of the Interface Research and Catalysis group (ECRC). The apparatus is equipped with various characterization and preparation tools described in [85]. A remote-controlled gas dosing system and evaporation sources allow for *in-situ* investigation with a vacuum Fourier-transform infrared (FT-IR) spectrometer (Bruker Vertex 80v). The measurements were performed in an ultrahigh vacuum chamber with a base pressure of $1 \cdot 10^{-10}$ mbar. To exclude molecular decomposition during deposition of the molecular layer, the attenuated total reflectance (ATR) reference spectrum of NiTPP in powder was measured. The principle of an ATR measurement is briefly introduced in the next section.

ATR

When light incidences on an interface to a medium with a lower index of refraction, it generally splits into two components at the interface, one of which is reflected and the other is refracted, as shown in Figure 13 (a). While the reflected beam has the same angle to the surface normal as the incident beam, the transmitted beam is refracted according to Snell's law

$$n_1 \, sin\, \Theta_1 = n_2 \, sin\, \Theta_2, \tag{21}$$

where n_1 and n_2 are the indices of refraction of the optically denser and thinner medium, respectively. Θ_1 and Θ_2 are the angles between the surface normal and the incident beam and the normal and the refracted beam, according to Figure 13 (a). In case the light comes

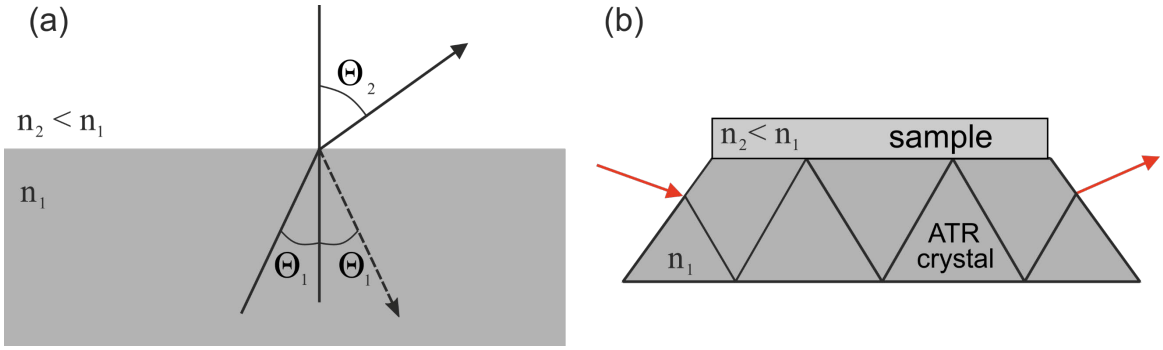

Figure 13) (a) Important angles for describing the reflection and transmission of a light beam that is incident from an optically denser medium (with an index of refraction n_1) onto the interface to an optically thinner medium (with $n_2 < n_1$). (b) Typical geometry of an ATR measurement. Figure (b) adapted from [186].

from the side of the medium with a higher index of refraction (here n_1), there is a critical angle of incidence for which there is no transmitted beam when exceeded. This phenomenon is known as total internal reflection. However, the boundary conditions require an electromagnetic field on both sides of the interface. It can be shown that even for total reflection, the amplitude of the electromagnetic field does not drop abruptly to zero. Instead, it can be described as a harmonic wave propagating parallel to the interface that is exponentially damped in the direction perpendicular to the interface in the optically thinner ($n_2 < n_1$) medium. This is called an evanescent wave. When the evanescent wave is in resonance with vibrational modes of the optically thinner medium, the light is

absorbed. Therefore, the optically thinner medium is the sample in an ATR measurement. As shown in Figure 13 (b), the experiment is designed such that several reflections take place to enhance the sensitivity. As the spectral bands of an ATR spectrum only appear in the signal of a multilayer sample if the molecules if the latter are intact, an ATR measurement can serve as an indication of a successful deposition. Thermal decomposition during the evaporation process, instead, would lead to missing features in the spectra of on-surface molecules.

4.3. STM

The experimental techniques introduced so far obtain spatially averaged information, as the signal originates from a macroscopic area of the surface, which contains many electronically or vibrationally excited molecules. STM is a widely employed tool that offers the possibility to resolve single molecules and even atoms, as lateral and vertical resolutions of 1 Å and 0.01 Å, respectively, can be reached [86].

In an STM experiment, a bias is applied between a conductive tip in the vicinity of the surface and the sample. This situation can be viewed as two potential wells separated by a barrier in the form of the vacuum between tip and sample, as shown in Figure 14.

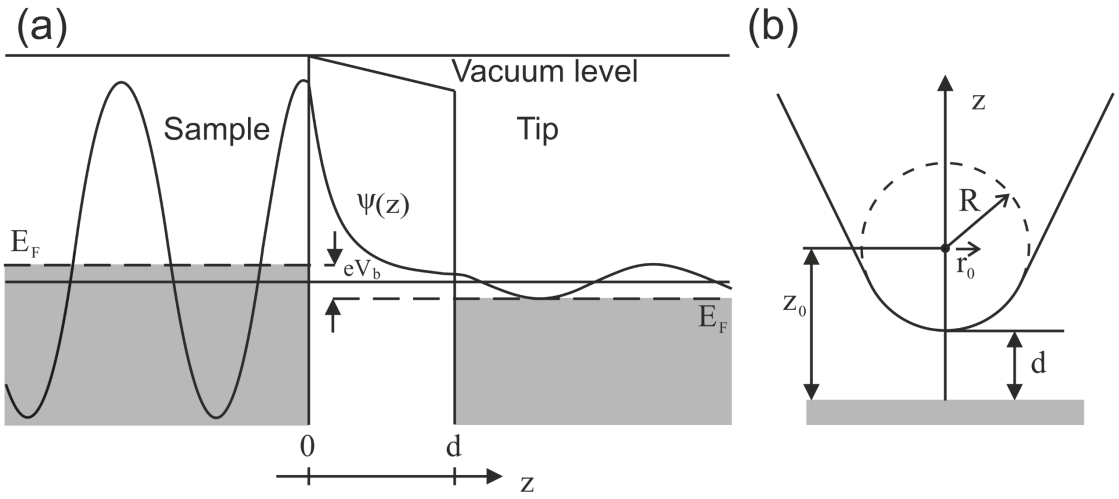

Figure 14) (a) Schematic of a one-dimensional metal-vacuum-metal tunnel junction, modelling the sample and the tip in an STM measurement. (b) Model of the tip as a locally spherical potential well, as described by Tersoff and Hamann. Figure adapted from [86].

While there is no classical solution of the Schrödinger equation in the area $0 < z < d$, and the barrier is impenetrable in a classical description, two quantum mechanical solutions in this range are

$$\psi(z) = \psi(0)\exp(\pm\kappa z), \tag{22}$$

with

$$\kappa = \frac{\sqrt{2m(U-E)}}{\hbar}. \tag{23}$$

Hence, the probability density $|\psi(z)|^2$ depending on the distance z and an applied bias U in this range is non-zero and bidirectional tunneling of electrons between the tip and the sample is possible. By applying a finite voltage $\pm V_b$ between the tip and the sample, a net

tunneling current of electrons from occupied states to unoccupied states can be induced. Depending on the sign of the applied voltage, electrons from the energy range E_F to $E_F \pm eV_b$ can flow from the tip to the sample or vice versa.

In the framework of the Tersoff-Hamann model, the tunneling current I is derived by approximating the tip as a locally spherical potential well with a radius R [87,88]. With the center at $\overrightarrow{r_0} = (0,0,z_0)$ and the sample surface in the $z = 0$ plane, it can be written as

$$I \propto U \cdot \rho_s(E_F, \overrightarrow{r_0}), \tag{24}$$

where ρ_s is the local density of states (LDOS) of the sample at the center of curvature of the tip. Therefore, the topography of a sample, i.e., a metal surface or an adsorbate, can be probed experimentally by rastering the surface and keeping the tunneling current constant, while the vertical distance is varied using a feedback system.

Experimental setup

The STM experiments in this work were performed by Alessandro Sala in the TASC laboratories in Trieste, Italy. The measurements were done with an Omicron LT-STM system at a sample temperature of 77 K. The microscope is in an ultrahigh vacuum chamber with a base pressure of below $7 \cdot 10^{-11}$ mbar. The images were acquired in a constant current mode, as described above. An inverse bias voltage was applied to the tip while the sample was grounded. Electrochemically etched tungsten tips were used for imaging.

4.4. Data treatment

NEXAFS

The energy of the absorption spectra presented in this thesis was calibrated by simultaneous acquisition of the drain current of the last toroidal mirror before the sample. A prominent feature in this absorption signal due to contamination on the beamline optics has been once calibrated by measuring $1s \rightarrow \pi^*$ gas-phase transitions of CO and N_2 at 287.4 and 410.1 eV, respectively [71]. By shifting the spectra in photon energy such that this feature in the drain current falls at the energy that has been obtained in this calibration, a potential offset, e.g., in the mechanical movement of the monochromator grid, is corrected.

Furthermore, the partial electron yields were normalized by the drain current of the last toroidal mirror and the signal of the clean sample. This was done by calculating the double ratio

$$\frac{I_{\mathrm{mol}}/I_{0,\mathrm{mol}}}{I_{\mathrm{clean}}/I_{0,\mathrm{clean}}}$$

Here I_{mol} and $I_{0,\mathrm{mol}}$ are the partial electron yield and the drain current of the toroidal mirror for the sample with the molecular film and I_{clean} and $I_{0,\mathrm{clean}}$ are the corresponding values for the clean substrate. The normalization by the drain current accounts for both the beam current variations in the storage ring and the photon flux decrease due to contamination. The additional normalization by the signal of the clean substrate allows the extraction of the signal stemming from the molecules.

XPS

The photon energy was calibrated by acquiring a Cu $3p_{3/2}$ spectrum and shifting it to a binding energy of 75.1 eV after every movement of the grid to correct for a potential offset of the monochromator grid and ensure reproducibility of the data. The fits of the N $1s$, C $1s$, and Ni $2p_{3/2}$ spectra in this work were performed by subtracting a linear and an integrated background and fitting Voigt profiles to the experimental data. The experimental resolution and inhomogeneity contributions were accounted for by a Gaussian broadening of 300 meV.

XMCD

The absorption spectra were acquired two times for each helicity in the order μ_+, μ_-, μ_-, μ_+. The average of the two spectra belonging to each helicity was calculated to correct for possible radiation damage of the sample during the measurement. Subsequently, the same background was subtracted from the two resulting average absorption spectra for each helicitiy. The background-corrected spectra were used for the integration according to the sum rules in equations (18) and (19). A detailed description of the evaluation of the isotropic absorption intensity I_{iso} contained in the sum rules is given in section A.1.

5. Results and discussion

This section will start with a description of the preparation for the different samples investigated in this thesis. Following the line of questions presented in section 3.1, we will then discuss possibilities to quench the charge transfer and tune the hybridization at the NiTPP/Cu(100) interface.

A promising approach to reduce the charge transfer consists in passivating the Cu(100) surface by preparation of a $(\sqrt{2} \times 2\sqrt{2})$R45° Cu(100) missing-row oxygen reconstruction, as the electrons at this surface were reported to be immobilized in Cu-O bonds [89]. The consequences of such an oxygen reconstruction for adsorbed NiTPP molecules are discussed in section 5.2. This chapter consists of parts that have been published in [90].

Subsequently, functionalization of the NiTPP molecules with NO_2 is discussed. While several publications address the adsorption of the strong donor NO, we found that NiTPP/Cu(100) is much more reactive to NO_2, requiring doses that are lower by a factor of 10^3 for full coverage, i.e., one nitrogen dioxide molecule per porphyrin. The chemical reactivity, the electronic, and the magnetic characteristics of a molecule, are inherently interwoven as they are all strongly driven by the alignment of the valence band levels. Therefore, the adsorption of NO_2 could give rise to intriguing effects on the electronic and magnetic configuration of the NiTPP/Cu(100) interface. This is investigated in section 5.3.

The reversibility of the NO_2 ligation is fundamental for designing devices such as sensors that need to be regenerable at will. In this regard, annealing is a common means of removing adsorbed molecules on top of porphyrins and, thereby, restoring the properties of the pristine metal-organic interface. However, as mentioned in section 2.2, on-surface porphyrins with highly flexible peripheries are prone to undergo intramolecular reactions at temperatures that allow C-H dissociation. The structural stability at such high temperatures is tested with a broad set of complementary techniques in section 5.4. This section consists of parts that have been published in [47].

5.1. Sample preparation

Two substrates have been used in this thesis, i.e., a copper (100) crystal (Cu(100)) and a $(\sqrt{2} \times 2\sqrt{2})$R45° oxygen-reconstructed Cu(100) surface, hereafter abbreviated as O-Cu(100). NiTPP was deposited onto both substrates up to a coverage in the monolayer regime. Afterward, the resulting NiTPP/Cu(100) and NiTPP/O-Cu(100) systems were exposed to doses of NO_2 gas ranging up to 20 L. The preparation and characterization of NiTPP/Cu(100) will be presented in this section, whereas NiTPP/O-Cu(100) and NO_2-NiTPP/Cu(100) will be characterized separately in sections 5.2 and 5.3.

The copper substrate was cleaned by several cycles of Ar^+ sputtering at 2.0 keV and subsequent annealing to 800 K. The cleanness was checked by standard techniques available at the different setups: at the NanoESCA beamline and the facilities of the Interface Research and Catalysis group (ECRC) of the Friedrich-Alexander-University Erlangen-Nuremberg, the cleanness was checked by LEED. Sharp, rectangularly arranged diffraction spots and the absence of a diffuse background indicated a clean (100) surface. At the ALOISA beamline, XPS measurements were performed at core-level energies of the most common contaminants, i.e., the O 1*s*, C 1*s*, and N 1*s*. The absence of any features in these energy ranges was taken as an indication of successful cleaning.

Commercial NiTPP molecules (Sigma Aldrich) with a purity of 95 % were thermally sublimated at 570 K from a Knudsen cell type evaporator onto the Cu(100) and O-Cu(100) substrates kept at room temperature. At the ALOISA beamline, the evaporation rate was checked by means of a quartz micro-balance. Depending on the experimental setup used, the coverage was checked by LEED (NanoESCA, X-Treme, ECRC), XPS (NanoESCA and ALOISA), IRAS (ECRC), and STM, as explained below.

In the LEED patterns, additional sharp spots can be seen after NiTPP deposition, as reported in [13]. With increasing coverage, the diffraction spots gain intensity. When exceeding the 1 ML regime, the spots blur, suggesting that the second layer does not grow in an ordered fashion. Accordingly, a sharp, intense LEED pattern was taken as an indicator of coverage in the monolayer regime.

Employing XPS, the coverage can be checked by measuring the Ni 2*p* core-level spectrum. Up to a coverage of 1 ML, the Ni 2*p* spectrum consists of a single feature at a binding energy of 859.2 eV due to the substrate-induced reduction of the central nickel atom [14]. Upon the formation of the second layer, which does not strongly interact with the substrate, a second component starts to grow at higher binding energies, as shown in Figure 15. This component can

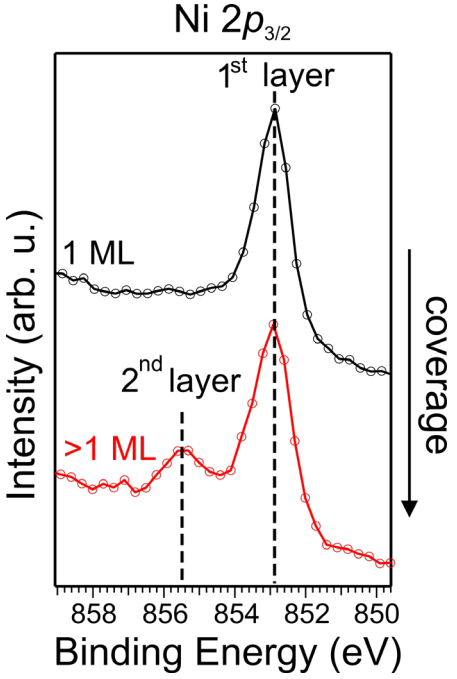

Figure 15) Ni $2p_{3/2}$ core-level spectra of the NiTPP/Cu(100) interface for different NiTPP coverages. The corresponding thicknesses of the molecular films are indicated in the graph. The spectra were measured in a normal emission geometry with a photon energy of hv = 1020 eV.

be assigned to the gas-phase-like Ni(II) oxidation state in NiTPP molecules that are not in direct contact with Cu(100) [91].

With IRAS, a monolayer NiTPP coverage can be identified by a comparison of the spectra acquired from molecular films with different thicknesses deposited onto the copper substrate. This approach provides an additional way to determine the coverage that is complementary to XPS and LEED, and therefore, is discussed in the following. It shall be noted that all the IRAS measurements and the subsequent analysis in this work were performed along with Dr. Miroslav Kettner, Chantal Hohner and Prof. Jörg Libuda from the Interface Research and Catalysis group (ECRC) at Friedrich-Alexander-University Erlangen-Nuremberg. Figure 16 shows IRA spectra of different film thicknesses deposited on Cu(100).

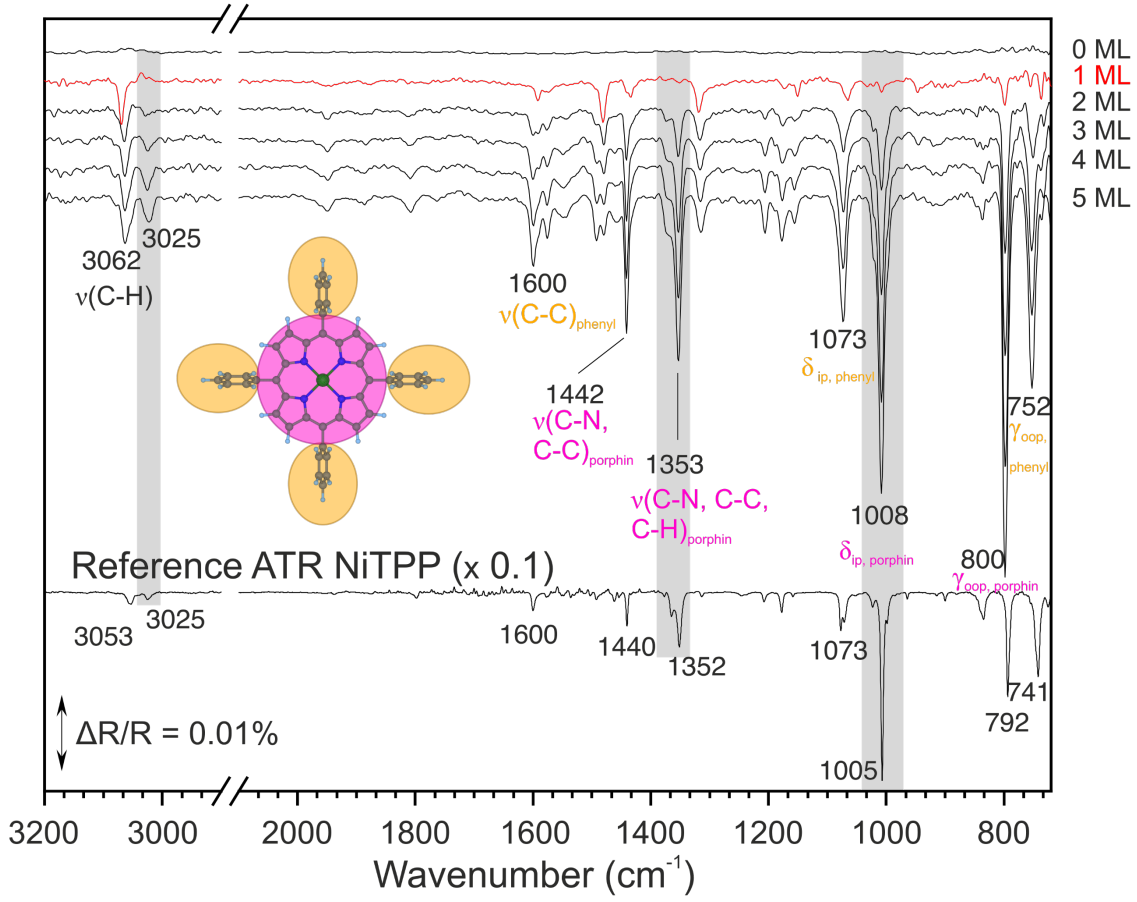

Figure 16) Top: Selected IRA spectra recorded during deposition of 5 ML NiTPP on Cu(100) at 300 K (ip = in plane, oop = out of plane). Bottom: Reference ATR IR spectrum of NiTPP. Figure adapted from [127].

In the following, a brief introduction of the vibrational modes that allow for a determination of monolayer coverage will be given. Starting with the 1 ML regime (spectrum plotted in red), most spectral components can be found with the same shape in the multilayer spectra. However, some features can be found exclusively in the multilayer spectra, i.e., the bands at 3025, 1353, and 1008 cm^{-1} (highlighted in grey). By comparison with computations and previous experiments [47,92], we ascribe them to C-H stretching ν(C-H), combined stretching of C-C, C-N (and C-H) in the pyrrole units $\nu(\text{C-N, C-C, (C-H)})_{\text{porphin}}$, and in-plane deformation of the porphin $\delta_{\text{ip, porphin}}$. As IRAS is sensitive to the adsorption geometry,

differences between monolayer and multilayer spectra often indicate a preferential orientation of adsorbates near the surface. The underlying reason is the metal surface selection rule (MSSR), implying that only those modes with a dynamic dipole moment that is not parallel to the surface are active in IRAS.

While the MSSR was introduced for a general case in section 4.2.3, the current section elaborates on the implications for the signal of the adsorbed NiTPP molecules. Information on the molecular conformation is obtained by the four IRA signal components of the NiTPP monolayer on Cu(100), i.e., the in-plane deformation vibrations of the porphin $\delta_{ip,\ porphin}$ (1008 cm^{-1}) and phenyl unit $\delta_{ip,\ phenyl}$ (1073 cm^{-1}) and the out-of-plane deformation modes of the porphin $\gamma_{oop,\ porphin}$ (800 cm^{-1}) and phenyl unit $\gamma_{oop,\ phenyl}$ (752 cm^{-1}). As illustrated in Figure 17, the flat-lying NiTPP can be divided into a macrocycle plane (a) oriented parallel and phenyl planes (b) that are tilted to the surface.

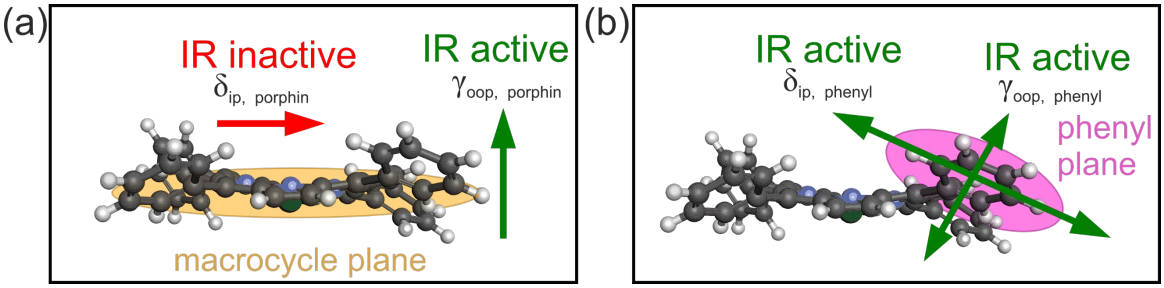

Figure 17) Model of the adsorbed NiTPP illustrating the orientation of the dynamic dipole moment for (a) $\delta_{ip,\ porphin}$ and $\gamma_{oop,\ porphin}$, (b) $\delta_{ip,\ phenyl}$ and $\gamma_{oop,\ phenyl}$ (ip = in plane, oop = out of plane). Figure adapted from [127].

In [14], the adsorbed NiTPP molecule was reported to have a flat-lying macrocycle, oriented parallel to the surface and phenyl rings that are rotated by approximately 69° ± 5° vis-à-vis the macrocycle plane. Accordingly, the in-plane vibration $\delta_{ip,\ porphin}$ is also parallel and thus IR inactive, whereas the out-of-plane component $\gamma_{oop,\ porphin}$ is IR active. Regarding the phenyl rings, both deformations ($\delta_{ip,\ phenyl,}$ and $\gamma_{oop,\ phenyl}$) feature dynamic dipole components parallel and perpendicular to the surface. Hence, they are IR active but less intense as the parallel component cannot be detected [84]. Altogether, this implies that the NiTPP is lying flat on the Cu(100) surface, in agreement with the adsorption geometries of MTPP reported in the literature [29,93–96]. As soon as the monolayer regime is exceeded, the three missing signals, highlighted in grey, rapidly gain intensity, confirming the loss of preferential orientation as already previously suggested by NEXAFS [14,90]. These characteristic differences are a clear mark that allows for the discerning of the transition from the monolayer to the multilayer growth regime directly from the IR spectra.

To exclude decomposition of the molecules during deposition, an ATR spectrum, shown at the bottom of Figure 16, was measured. Generally, a decomposition of the molecules during the deposition would lead to different vibrational bands in the ATR spectrum and the adsorbed molecules. Thus, the fact that the features in the ATR spectrum are also present in the multilayer spectra points to a successful deposition, i.e., that the adsorbed molecules are intact.

Employing STM, a densely packed, single-layer molecular film could be observed on large-scale images as shown in Figure 18. Hereafter, such a densely packed film is referred to as 1 ML. The STM images presented in this work were measured by Dr. Alessandro Sala from the TASC laboratory of the Centre Nazionale delle Ricerche (CNR-IOM) in Trieste, Italy, within the framework of a collaboration under the NFFA Europe Transnational Access Activity. Two rotational domains mirrored by about ± 8° with respect to the [001] direction of the substrate can be seen, in agreement to what has been reported in [13].

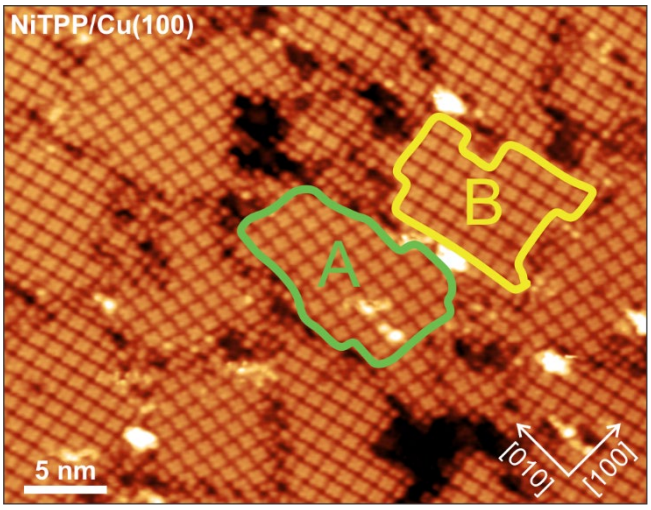

Figure 18) Large-scale STM images of NiTPP/Cu(100) acquired at 77 K. The NiTPP coverage is close to 1 ML. The molecules self-assemble in two rotational domains, highlighted as A and B, respectively. The lateral size is (38.8 x 30) nm^2 and the tunneling parameters are V_b = +1 V, I = 500 pA. Figure adapted from [127].

For preparing the NiTPP/O-Cu(100) system, the clean copper substrate was kept at a temperature of 500 K and exposed to 800 L of O_2, as described in a well-established recipe [97]. After this procedure, additional spots in the LEED pattern and STM images confirmed a successful preparation of the $(\sqrt{2} \times 2\sqrt{2})R45°$ oxygen-reconstructed Cu(100) surface. After that, the NiTPP layer was deposited equivalent to the preparation of NiTPP/Cu(100), and STM measurements were performed to ensure a full monolayer coverage. A characterization of O-Cu(100) and NiTPP/O-Cu(100) will be presented in section 5.1.

The NO_2-NiTPP/Cu(100) sample was prepared by dosing approximately 8 L NO_2 gas (Linde, purity grade 2.0). The gas was introduced through a leak valve for 4.5 minutes at a pressure of $5 \cdot 10^{-8}$ mbar (1 L = $1.33 \cdot 10^{-6}$ mbar · s). At ECRC, the gas was introduced pulse-wise by a remote-controlled gas dosing system. Generally, we observed that the spectroscopic signal measured by XPS and IRAS was saturated around this dose, and exposure to higher doses did not further affect the spectra.

5.2. Decoupling from the substrate by an interlayer

The results in this section will be divided into three parts. First, we will characterize the O-Cu(100) and NiTPP/O-Cu(100) samples by LEED and STM. After that, we will discuss the electronic structure of NiTPP/O-Cu(100) and compare it to substrate-decoupled NiTPP in a multilayer sample. Finally, the differences between the decoupled system of NiTPP on the O-Cu(100) substrate and the strongly interacting molecules in direct contact with Cu(100) is discussed.

5.2.1. Structural characterization of the O-Cu(100) interface

The NiTPP/O-Cu(100) sample was prepared as described in section 5.1, following the well-established recipe in [97]. The missing-row reconstructed O-Cu(100) surface is an early stage of Cu oxidation [98] with coverage of slightly below 0.5 ML. In this reconstruction, every fourth row of Cu atoms is missing. The O atoms occupy the sites along the edges of the missing rows, as shown in the model in Figure 19 [99].

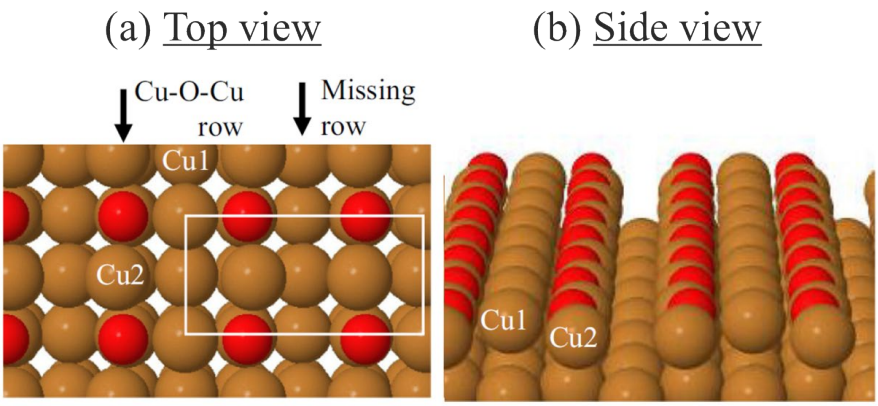

Figure 19) Model of the missing-row reconstructed ($\sqrt{2} \times 2\sqrt{2}$)R45° O-Cu(100) surface, top (a) and side (b) view. Figure adapted from [99].

LEED images of the clean copper surface and the oxygen reconstructed surface are shown in Figure 20. Concerning the copper surface, four spots arranged in a square and a low background signal confirm a clean (100) substrate. After exposing the annealed substrate to an oxygen atmosphere according to the recipe, additional spots revealing the ($\sqrt{2} \times 2\sqrt{2}$)R45° oxygen reconstruction appear in agreement with patterns reported in the literature [100].

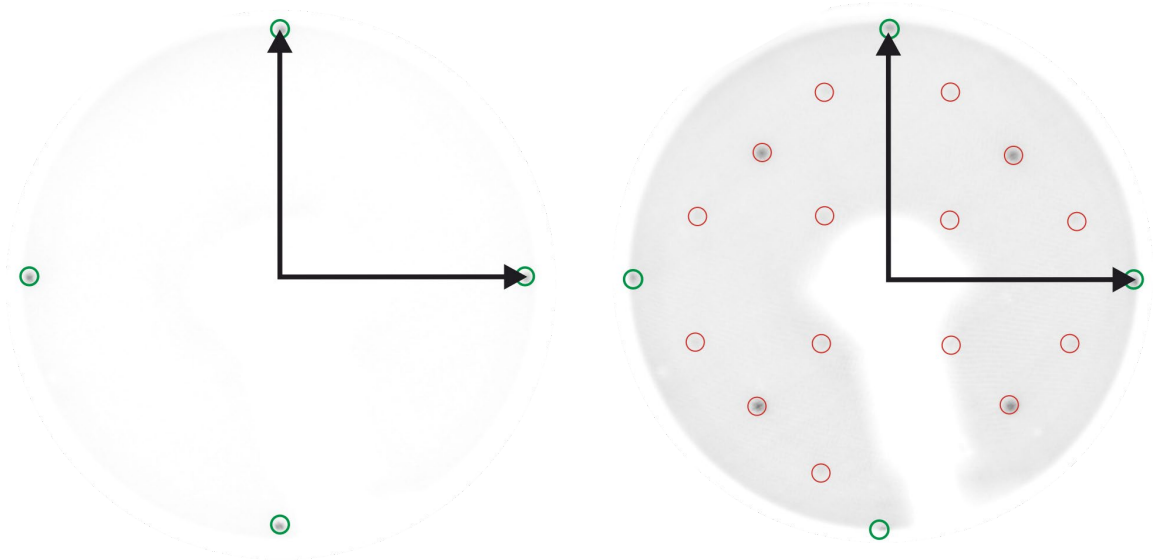

Figure 20) LEED images of the clean Cu(100) surface (left) and the oxygen reconstructed surface (right) acquired at a kinetic energy of 45.2 eV and 44.1 eV, respectively. Green circles highlight the first-order diffraction spots of the Cu(100) substrate, while red circles highlight the spots induced by the oxygen-reconstruction.

The characterization of the O-Cu(100) and the NiTPP/O-Cu(100) surface by LEED and STM is described in more detail in [101]. The main results of this analysis are presented below. The missing row reconstruction can also be seen in real space via STM, as reported in the literature [99]. As shown in Figure 21, two rotational domains are aligned along the [001] and [010] marked with black arrays of squares.

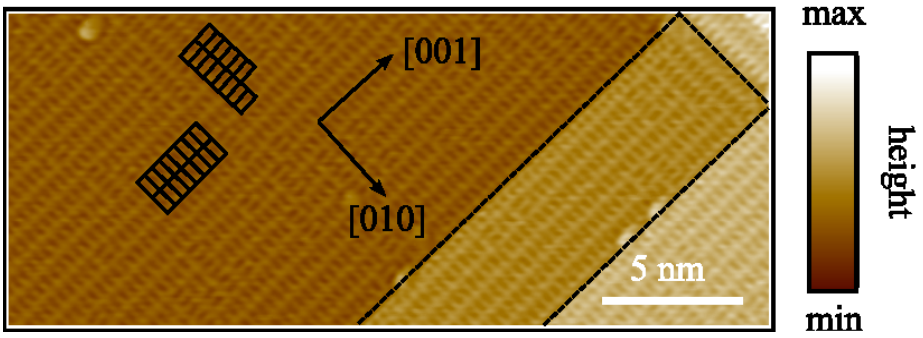

Figure 21) STM image of the O-Cu(100) surface with a lateral size of (3 x 8) nm^2. Two step edges can be seen in the right part of the image. The missing row reconstruction can be found in two different rotational domains (highlighted by black arrays of squares), aligned parallel to the [001] and [010] directions, respectively. The tunneling parameters are V_b = -1 V, I = 100 pA. Figure reproduced from [101].

The STM image after deposition of an additional NiTPP layer, i.e., of NiTPP/O-Cu(100) is shown in Figure 22.

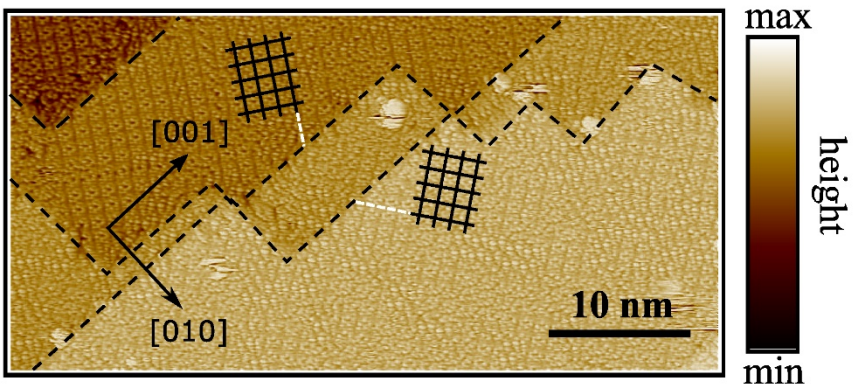

Figure 22) STM image of NiTPP/O-Cu(100) with a lateral size of (47 x 21) nm^2. The molecules assemble in a dense monolayer. Two different rotational domains rotated by approximately 56-59° with respect to the [001] direction are highlighted by black grids. The tunneling parameters are V_b = 2 V, I = 100 pA. Figure reproduced from [101].

At a coverage of 1 ML, i.e., a densely packed single-layer molecular film, the molecules assemble into two domains that are commensurate with the substrate and mirrored with respect to the [100] axis [101]. The angle of these domains with respect to the [100] axis can be approximated between 56° and 59° [101]. The grids defined by the two domains molecular adlayer can be described with respect to the underlying Cu-O structure by the epitaxial matrices

$$A = \begin{pmatrix} 5 & -1 \\ 1 & 5 \end{pmatrix} \text{ and } B = \begin{pmatrix} -5 & -1 \\ -1 & 5 \end{pmatrix}. \tag{25}$$

The distance between the centers of two adjacent molecules is approximately 1.2 nm. With this matrix, it is also possible to simulate the corresponding LEED pattern. In Figure 23,

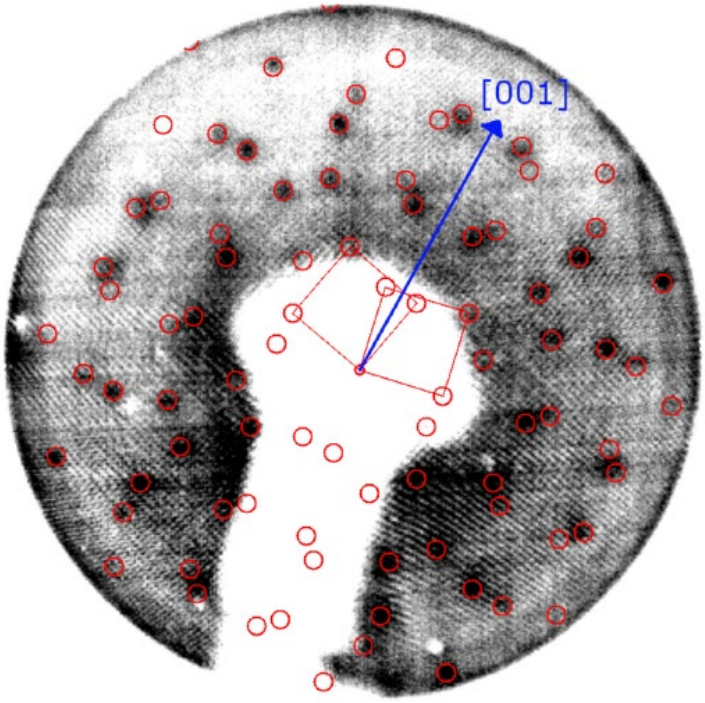

Figure 23) LEED image of NiTPP/O-Cu(100) acquired at an electron energy of 26.3 eV. The spots of a simulated LEED pattern predicted by STM are marked with in red circles. Figure reproduced from [101].

the simulated LEED pattern is superimposed with the experimentally observed image of NiTPP/O-Cu(100). The reciprocal unit cells of the two rotational domains are highlighted by reddashed lines. The simulated diffraction spot positions are marked by red circles and are in reasonable agreement with our LEED image. From the simulation, the unit cell size is calculated to be (1.27×1.27) nm^2, which is in agreement with the value reported for NiTPP/Cu(100) [13]. In summary, LEED and STM images consistently confirm that NiTPP molecules adsorb in a long-range ordered superstructure on O-Cu(100).

5.2.2. Decoupling: comparison to a multilayer sample

The electronic structure of NiTPP/O-Cu(100) according to the results published in [90] is discussed in the present section. As the charge transfer towards NiTPP on bare copper was revealed by additional features in the valence band, we start with a comparison between the integrated valence bands, i.e., the $k_{\parallel}$-integrated intensities of the measured momentum maps. Figure 24 shows the integrated valence band spectra of O-Cu(100) and NiTPP/O-Cu(100).

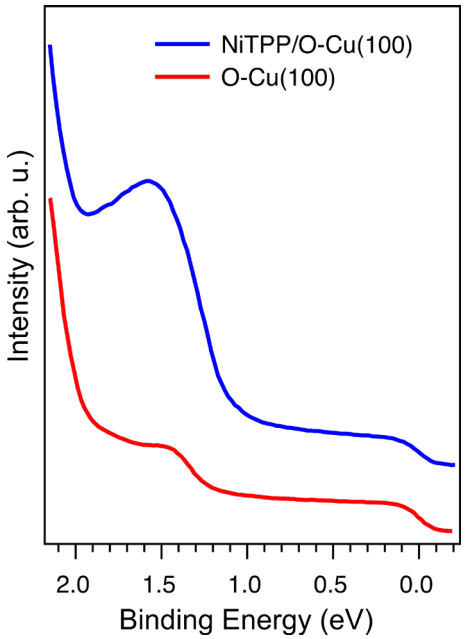

Figure 24) Angle-integrated valance band spectra of O-Cu(100) (red) and NiTPP(1 ML)/O-Cu(100) (blue) measured with a photon energy of hv = 35 eV. Figure adapted from [90].

The spectrum of O-Cu(100) consists of a featureless plateau below the Fermi level, stemming from the *sp* band of copper, and a feature at a binding energy of approximately 1.45 eV that was also observed for perylene-tetracarboxylic dianhydride on the same oxygen-reconstructed copper surface (PTCDA/O-Cu(100)) [89]. The deposition of NiTPP leads to an increase in intensity around a binding energy of 1.5 eV. Previous PT experiments revealed that the additional intensity can be ascribed to contributions from the HOMO and HOMO-1 [101], which are almost degenerate in the gas phase [13]. Remarkably, in contrast to NiTPP/Cu(100), the molecular fingerprints of the LUMO/+1 and LUMO+3 can be observed neither in the integrated valence band nor in the a $k_{\parallel}$-resolved maps investigated in a previous study [101]. Similarly, Yang *et al.* observed that

the oxygen reconstruction leads to a quenching of the LUMO feature for PTCDA on O-Cu(100) [89]. They mainly assigned it to an immobilization of the surface electrons in covalent Cu-O bonds, by which they lose their free-electron character. The missing fingerprint of the LUMOs in the valence band is a clear indication of a quenching of the charge transfer to the molecule and an electronic decoupling from the substrate.

As previously reported, such decoupling can also be achieved by preparing a NiTPP multilayer sample, which is often used as a reference for isolated molecules [14,102]. As a next step, these two methods to electronically decouple NiTPP from the Cu(100) surface are compared. For this, we measured the NEXAFS spectra of NiTPP/O-Cu(100) and a multilayer sample NiTPP(~ 8 ML)/Cu(100). In Figure 25, the K-edge spectra of carbon and nitrogen are shown. Notably, the resonances at both absorption edges appear at the same photon energies for the multilayer and the oxygen pre-treated sample, suggesting a similar electronic structure of the molecules in these two systems.

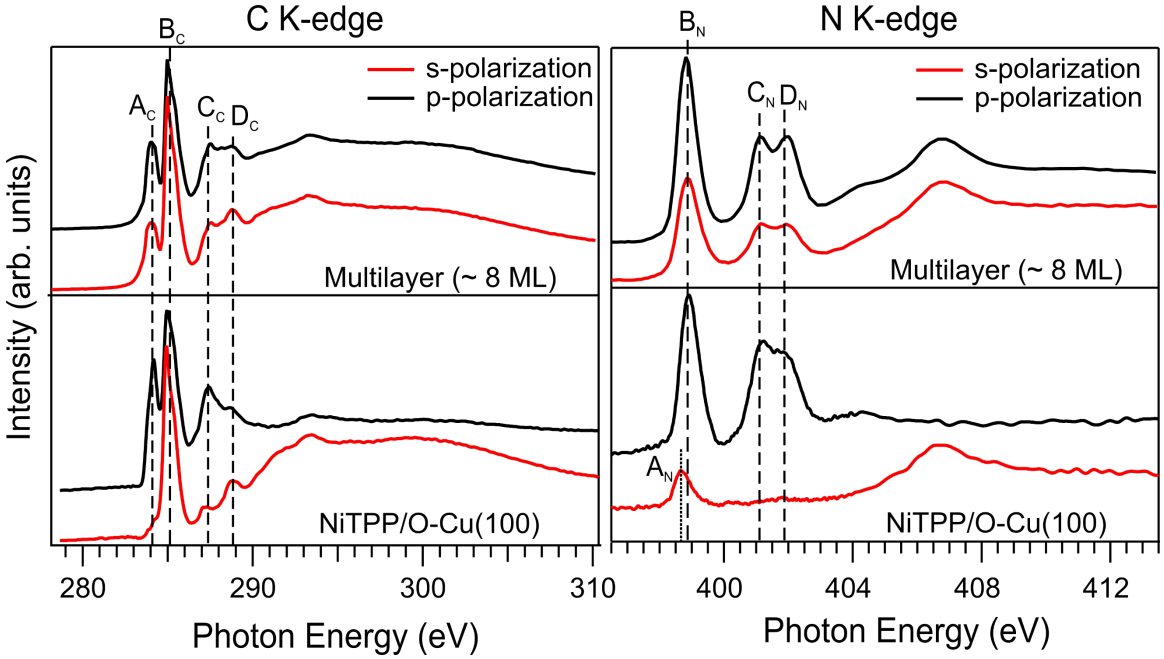

Figure 25) C K-edge (left) N K-edge spectra (right) of NiTPP(~ 8 ML)/Cu(100) (top panel) and NiTPP/O-Cu(100) (bottom panel). The spectra acquired in s- and p-polarization are plotted in red and black, respectively. Figure adapted from [90].

We start with the energetic structure of the C K-edge spectra by assigning the peaks according to the results reported in the literature. The peak A_C at 284 eV was assigned to a π^* feature located at the macrocycle, whereas the feature B_C at 284.9 eV can be ascribed to a π^*-type resonance at the peripheral phenyl rings [31]. The features C_C and D_C, at 287.5 eV and 289 eV, respectively, have been observed at similar energies in NEXAFS measurements of CoTPP multilayers, and theoretically assigned to different orbital symmetries at molecular subunits [103]. From a comparison with these assignments, the feature C_C can be interpreted as a π^*-type resonance at the macrocycle, whereas feature D_C can be ascribed to a σ^*-symmetry transition at the phenyl rings [103].

In the multilayer sample, none of the above peaks has clear dichroism, pointing towards a random molecular orientation as observed for other flexible porphyrins having peripheries with many degrees of freedom [104]. In contrast, clear dichroism in the NiTPP/O-Cu(100)

spectra suggests a preferential orientation of the adsorbed molecules and allows for a determination of the adsorption geometry. The features B_C and C_C (both π^*-type resonances at the macrocycle) have clear dichroism. The vanishing intensity of feature A_C in s-polarization indicates that the macrocycle of the adsorbed molecules is oriented parallel to the substrate. The intensities of the features related to transitions at the phenyl rings B_C and D_C do not entirely vanish in the s-polarization spectra, as the phenyl rings of adsorbed tetraphenyl porphyrins are typically are rotated and tilted. However, a rough estimation of the phenyl conformation is possible. From the intensity ratio of the signals measured in p- and s-polarization, the angle $\gamma = \frac{1}{2} arctan^2\left(I_s/I_p\right)$ between the phenyl plane and the surface can be calculated according to equation (12). As feature D_C also contains contributions to transitions to Rydberg states, we use the intensities of feature B_C, leading to an angle of $52° \pm 5°$. The error originates from the uncertainty of the intensity due to an overlap with adjacent features and a background intensity and is estimated by using the smallest and the largest ratios in a reasonable range around 284 eV. Even though the relative error amounts to almost 10 %, we can conclude that the quenching of the charge transfer for NiTPP/O-Cu(100) allows for a more coplanar orientation of the phenyl moieties. However, it shall be noted that the orientation of the phenyl rings is defined by a twist- and a tilt angle, as described in section 2.1. The contributions of these two angles to the flattening of the phenyls cannot be deconvoluted exclusively from presented NEXAFS data.

A similar picture is obtained by the N K-edge spectra. Starting from the multilayer sample, three features can be seen below the ionization threshold at ~ 404 eV, i.e., B_N, C_N, and D_N. In the spectra of NiTPP/O-Cu(100) acquired in s-polarization, a fourth feature with a σ^* symmetry can be appreciated, i.e., A_N. When compared with relevant literature, the features B_N and C_N can be ascribed to N $1s$ → LUMO/+1 and N $1s$ → LUMO+3 transitions [14,31,105]. A_N, instead, has a clear σ^* symmetry and can be assigned to a N $1s$ → LUMO+2 transition, as the LUMO+2 is a mixed ligand $2p_{xy}$- metal $3d_{x^2-y^2}$ orbital. Also here, the observed dichroism is in line with the adsorption geometry suggested by the C K-edge spectra. The fact that all $\pi^*(\sigma^*)$ features almost entirely vanish in the spectra acquired in s(p)-polarization supports a flat macrocycle oriented parallel to the surface. Moreover, since A_N is not visible in the NEXAFS spectrum of NiTPP/Cu(100), this provides another proof that the LUMO+2 of NiTPP gets filled on bare copper (100) [14]. Notably, this could not be assessed via PT [13].

It shall be emphasized that only through the preferential order of NiTPP on O-Cu(100), the distinction of the features A_N and B_N and the determination of their symmetry becomes possible. The σ^*-type resonance here referred to as A_N was also observed for porphyrins and phthalocyanines coordinated to other metals, such as Cu [70,106] and Co [107]. Moreover, it was found that its precise energy depends on the metal element chelated in the macrocycle [108] and the van der Waals interaction with the substrate [109]. In the spectrum of the disordered multilayer sample, these two features are both visible in measurements with p- and s-polarized light because of the random molecular orientation and cannot be resolved due to the inherently low intensity of the σ^*-type feature [90]. The high intensity of the π^* feature, even for small molecular tilt angles, leads to an overlap of

the two features that prevents a distinction. For NiTPP/O-Cu(100), however, it is possible to quantitatively analyze the intensities due to the parallel alignment of macrocycle and substrate. As mentioned in section 4.2.1, the absorption signal far above the ionization edge results from photoemission of an electron from core levels into continuum states and, therefore, is independent of the polarization orientation of the exciting light. Hence, it is reasonable to assume that the absorption intensities are equal at the high energy end of the spectrum and, accordingly, normalize the spectra at this value.

With this normalization, it is also possible to calculate the photoemission cross section by comparing the intensities of the σ^*- and the π^*-type features. Generally, the photoemission cross section σ_x is proportional to the oscillator strength f,

$$\sigma_x \propto f \cdot \rho(E) \tag{26}$$

with the density of states $\rho(E)$ and

$$f = \frac{2}{m_e \hbar \omega} \left| \langle f | \overrightarrow{A_0} \cdot \vec{p} | i \rangle \right|^2. \tag{27}$$

From the proportionality to the square modulus of the transition matrix element, it becomes clear that f is a measure for the intensity of a resonance [68]. Conversely, the intensity ratio of overlapping σ^* and π^* resonances can be used as an input for the theoretical calculation of the photoemission cross section. For the spectrum of NiTPP/O-Cu(100), the area ratio for σ^* to π^* is found to be 1 to 4.5 [90].

5.2.3. Comparison to NiTPP/Cu(100)

As described in detail in the previous section, the similarity of both energy position and line shape of the NEXAFS resonances measured of NiTPP on the oxygen pre-treated substrate and in the multilayer suggest a substantial electronic decoupling by the oxygen interlayer. In this section, we attempt to understand the consequences of the charge transfer to the first monolayer observed upon adsorption on the bare Cu(100) surface.

First, a comparison of the electronic structure at the macrocycle is presented. The C and N K-edge absorption spectra are shown in Figure 26.

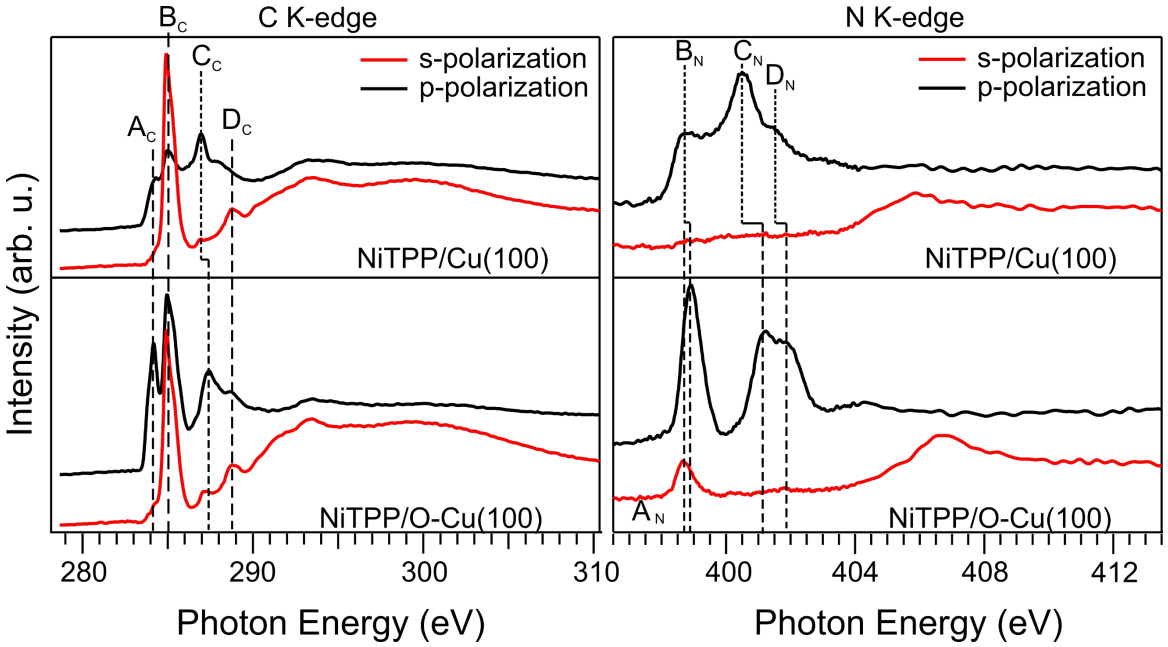

Figure 26) C K-edge (left) and N K-edge absorption spectra (right) of NiTPP/Cu(100) (top panels) and NiTPP/O-Cu(100) (bottom panels). The spectra acquired in s- and p-polarization are plotted in red and black, respectively. Figure adapted from [90].

Clear differences can be seen in the peak intensities measured at the C K-edge. Feature A_C, previously assigned to a π^* feature located at the macrocycle, has the same symmetry as on the passivated substrate, as can be seen from the small residual intensity measured in s-polarization. However, the partial filling of the π-type LUMO/+1 and LUMO+3 leads to a strong decrease in the intensity of the features A_N, as well as B_N, and C_N. This suggests a quenching of the charge transfer on the O-Cu(100) substrate and agrees well with the missing molecular fingerprints in valence band spectra. In addition, C_N is shifted to lower photon energies, as already observed in a previous comparison with a multilayer spectrum [14]. The dichroism of features A_C, C_C, and D_C is similar for both substrates, bare Cu(100) and O-Cu(100), which points toward a similar adsorption geometry. For the phenylic π feature B_C, instead, stronger dichroism can be observed on the clean copper substrate. This is caused by a bigger rotation angle of 68° ± 5° reported in [14].

In the N K-edge spectrum, an overall shift of the spectrum toward lower photon energies vis-à-vis the passivated system can be observed. A shift toward lower photon energies at the N K-edge was previously ascribed to a charge transfer from the substrate [14,110,111]. Moreover, the intensity of feature B_N, which we assigned to a π-type N 1*s* → LUMO/+1 transition in the previous chapter, is much stronger on the passivated surface. This is related

to the partial occupation of the LUMO/+1 through the charge transfer on bare Cu(100) [13,14]. Remarkably, feature A_N is not visible in the s-polarized spectrum of NiTPP/Cu(100), providing another proof that the LUMO+2 of NiTPP gets filled on bare copper (100) [14]. This orbital could not be accessed via PT, as the corresponding k-space features are located at high $k_{\parallel}$-values [13,43].

The experimental evidence collected so far points toward a similar adsorption structure and a quenching of the charge transfer toward the LUMOs localized at the macrocycle. However, to assess how this affects the reduction of the central nickel ion that was observed on the bare Cu(100) surface, we will now discuss the absorption spectra at the Ni L_3-edge. As the surface-induced change of the oxidation state was mainly detected by examining the core-level excitation to the σ^*-type LUMO+2 [14,90], the discussion here is restricted to the NEXAFS spectra acquired in s-polarization. The spectra of NiTPP/Cu(100) and NiTPP/O-Cu(100) are shown in Figure 27.

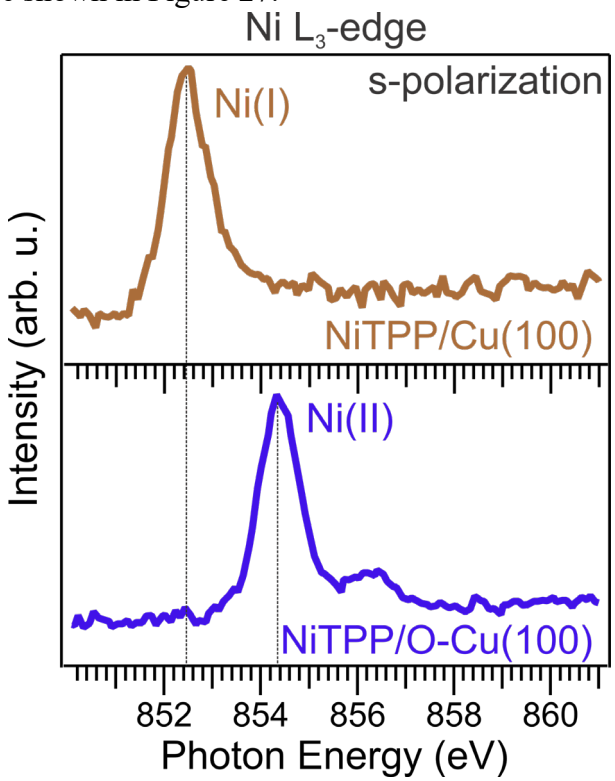

Figure 27) Ni L_3-absorption spectra of NiTPP/Cu(100) (top) and NiTPP/O-Cu(100) (bottom). Figure adapted from [127].

The spectrum of NiTPP/Cu(100) consists of a single-peak feature with a centroid at a photon energy of 852.4 eV. This agrees with previously reported results and is associated with an intra-atomic $2p_{3/2} \rightarrow 3d_{x^2-y^2}$ transition [14]. While the position is characteristic of the Ni(I) oxidation state, the single peak structure points toward a d^9 configuration [112].

The spectrum taken at the NiTPP/O-Cu(100) interface mainly consists of a sharp feature at higher photon energy (854.3 eV) and a small satellite peak at 856.5 eV. Similar behavior was also found for a Ni(II) low-spin (LS) compound [112]. As mentioned in section 2.1, a Ni (II) LS configuration with an empty $d_{x^2-y^2}$ orbital is typical for a tetra-coordinated nickel atom as in the gas-phase porphyrin [113]. Thus, this indicates that the strong

decoupling induced by the oxygen reconstruction of the copper surface not only quenches the charge transfer from the surface but also substantially weakens its influence as a ligand.

5.2.4. Conclusions

To summarize, a special oxygen treatment before the NiTPP deposition prevents the central Ni atom from stabilizing in a +1 oxidation state like in Ni(I)TPP/Cu(100) and leads to a preservation of the +2 oxidation state of nickel. Hence, Ni(II)TPP/O-Cu(100) is a valuable reference for a system with a reduced molecule-substrate interaction due to several reasons.

First, the clear dichroism proves a preferential orientation of the molecules, which, in contrast to a molecular multilayer thin film or gas phase measurement, allows for the discrimination of features that are close in energy but have different symmetries. For this system, in particular, the NEXAFS spectrum includes a distinct σ^*-type feature, which was associated with a transition to the LUMO+2 due to its symmetry inferred from a clear NEXAFS dichroism [14]. The absence of this feature in the NEXAFS spectrum of NiTPP on the bare copper surface indicates that the LUMO+2 gets occupied on the bare copper surface, while on O-Cu(100), it stays empty.

Additionally, this system can be seen as a gas-phase reference, as the resonances have the same energies as in the multilayer sample. Therefore, it is a practical means of investigating the implications related to the Ni oxidation state. We can directly compare Ni(I)TPP/Cu(100) and Ni(II)TPP/O-Cu(100) and answer, for example, how the reactivity to certain gases is related to the oxidation state of the central Ni atom. As the use of reference spectra is not confined to NEXAFS, the impact of the charge transfer on vibrational properties can also be investigated by IRAS or high-resolution electron energy loss spectroscopy (HREELS).

Lastly, due to the combination of long-range molecular order suggested by STM and confirmed by LEED [101] and the weakened molecule-substrate coupling, the system can be used for exploring the potential of time-resolved photoemission tomography (TR-PT). Generally, a strong hybridization between a metallic substrate and an organic molecule leads to reduced lifetimes of unoccupied states vis-à-vis the unoccupied states of a gas-phase molecule. An electronic decoupling increases the lifetime of transiently occupied states, enabling their detection by pump-probe-based techniques. Wallauer *et al.* showed in a proof-of-principle experiment that the LUMO of PTCDA shows a single exponential decay of 250 fs on the same O-Cu(100) substrate [114]. This makes it possible to follow excitation mechanisms not only in time but also in space.

5.3. Functionalization with axial ligands

While the gas-phase properties of the molecules are preserved to a large extent through pre-adsorbed oxygen, the preparation requires an additional working step. More importantly, restoring the surface-induced Ni(I) state on bare Cu(100) inevitably requires cleaning the substrate and subsequent re-deposition of NiTPP. For the realization of multifunctional devices, however, the reversibility of the control of magnetic and optical or transport properties by external stimuli is of great interest. Against this backdrop, a reversible on-top ligation with small molecules was proposed for the realization of chemical switches [9].

Caging the chelated metal ion in a crystal field through their unsaturated axial coordination bonds has been demonstrated to be a viable way to stabilize metal ions and to prevent their local moment from decreasing or being quenched by the interaction with the substrate [115]. This has been achieved already using molecular ligands, e.g., cyano- or carboxylic-molecular terminations, as demonstrated for Fe, Ni, and Mn ions forming 2-dimensional high-spin metal-organic networks [116–120]. Alternatively, the oxidation state can be tailored by the proper choice of porphyrins or phthalocyanines, as they exist in a variety of different spin states depending on the metal ion coordinated in their tetrapyrrolic macrocycle [15,16]. Additionally, long-range magnetic order can be induced by exploiting the molecule-substrate interaction. For example, ferromagnetic coupling of an iron porphyrin with a ferromagnetic film was achieved even at room temperature via superexchange interaction [121]. This offers a pathway for the control of the magnetism at such molecular interfaces. Well-established methods based on the anchoring of external axial ligand to the ion center [122] allow off-switching and spin-tuning transitions [9,12]. In contrast, attempts to realize a spin-off $\rightarrow$ spin-on transition are still limited to the adsorption of molecules at low temperature since chemical bonding has to overcome the spin-pairing energy, as in the example mentioned in [10]. A reversible spin-switching in porphyrin complexes can be achieved by mechanically moving an axial ligand strapped to the porphyrin ring [24]. However, such an approach requires a local voltage pulse generated by an STM tip, which is cumbersome and not scalable for logical operations with thousands of bits.

The magnetic moment of metal ions in tetrapyrrolic compounds was also manipulated by chemical doping using alkali metals [123]. So far, this was demonstrated only at low temperatures in a top-down approach to control the alkali atom site [124]. In fact, the alkaline metal must be placed precisely atop the central ion, often inducing disorder in the molecular array; therefore, reversibility is hardly achievable [125]. Both functionalization and chemical doping lead to a decoupling of the molecule from the surface. This, in general, changes the energy alignment of the molecular orbitals (MOs) and ultimately affects the carrier injection properties across the molecular interface. Regarding the choice of the ligand, di-, tri-, and tetra-atomic molecules have been reported to affect the electronic and magnetic properties. This can happen through electron pairing induced by the formation of chemical bonds to complexed ions, as reported for NO-CoTPP [12], or a change of the energy level caused by a modification of the crystal field, as observed for NH_3-NiTPP [10]. In the case of chemical bonding, the ligand competes with the surface for the stronger bond, known as the surface-*trans* effect. This competition significantly depends on the charge

donation ability of the ligand, which follows the order NO > CH_3 > SO_3^2 > NO_2 > Br > Cl > NH_3 [126]. Being in the middle of this order, i.e., between NO and NH_3, the adsorption of NO_2 could lead to interesting mechanisms between a simple electron donation and a change of the crystal field experienced by the metal ion. This section consists of parts that have been published in [127].

5.3.1. Dependence of the reactivity on the Ni oxidation state

As the first step, the dependence of the reactivity with NO_2 on the oxidation state of the central Ni ion is tested. For this, we exposed the Ni(I)TPP/Cu(100) and the Ni(II)TPP/O-Cu(100) interfaces at room temperature to NO_2 gas. The latter system can be seen as a reference system for NiTPP with a more gas-phase-like electronic structure in this comparison, as discussed in section 5.2.

The resulting changes were monitored using XPS. The N 1*s* core-level spectrum of Ni(I)TPP/Cu(100) consists of a single component at 398.6 ± 0.2 eV, as shown in Figure 28, top. This is expected for the chemically equivalent N atoms in a MTPP macrocycle [128].

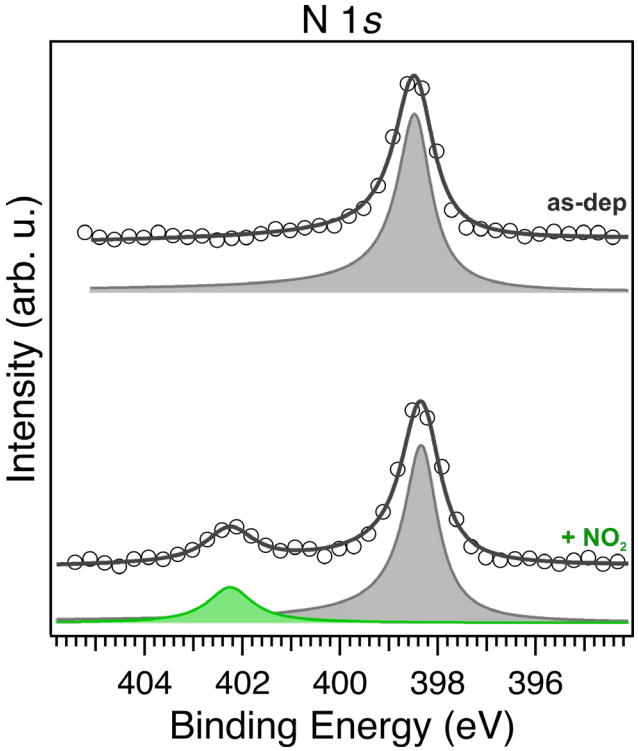

Figure 28) N 1*s* XPS spectra of the as-deposited NiTPP/Cu(100) and after exposure to 8 L of NO2, top and bottom, respectively. The components obtained from a fit are plotted as filled areas below the spectra. The spectra were measured in a normal emission geometry with a photon energy of hν = 1020 eV. Figure adapted from [127].

It also excludes contamination by demetalated and other non-intact molecules, as such impurities would lead to additional components at different binding energy [129,130]. After exposing the Ni(I)TPP/Cu(100) interface to NO_2, a second peak grows at a binding energy of 402.5 ± 0.2 eV, while neither the area nor the binding energy of the initial peak is affected (see Figure 28, bottom). Therefore, this peak can tentatively be assigned to the nitrogen atom of NO_2.

The area below that peak grows up to a dosage of around 8 L until a maximum value is reached, suggesting saturation of the NO_2 coverage. By fitting the spectrum, a peak area ratio of almost 1:4 between the peak appearing during exposure to NO_2 and the original peak, which is also present for the pristine Ni(I)TPP/Cu(100), was found. Considering that there are four N atoms in the NiTPP molecule and one N atom in the NO_2 molecule, this suggests a NO_2 coverage of almost one molecule per NiTPP molecule. Notably, a slight downward deviation from the ratio of 1:4 is because a small percentage of NiTPP molecules remains uncoordinated, as an analysis of the Ni $2p_{3/2}$ XPS spectra in Figure 29 shows.

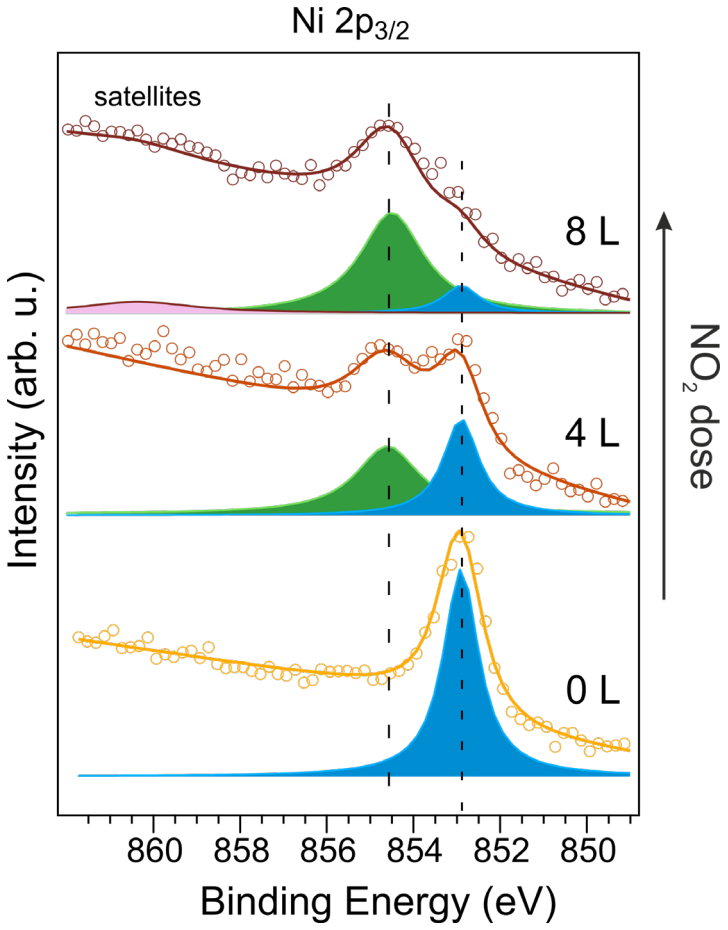

Figure 29) Ni $2p_{3/2}$ core-level photoemission spectra of the pristine NiTPP/Cu(100) (bottom) and after exposure to 4 and 8 L of NO_2 (middle and top, respectively). The spectra were measured in a normal emission geometry with a photon energy of hv = 1020 eV.

For pristine Ni(I)TPP/Cu(100), a single component is visible at a binding energy of 859.2 ± 0.2 eV, as previously reported [14]. After dosing 4 L of NO_2, a new feature appears at 854.6 ± 0.2 eV, and the intensity of the first peak is slightly reduced. After another dose of 4 L, i.e., a total dose of 8 L, the new peak further increases in intensity, while the original peak decreases. At this point, we can assume that the original peak is from the pristine NiTPP molecules, whereas the new peak is related to molecules that bind NO_2 molecules. From the peak areas of the two components, we estimate the share of pristine NiTPP molecules to be below 20 %. This explains the fact that the area ratio of the N 1*s* components is slightly below 1:4. Moreover, we can exclude the adsorption of several NO_2 molecules at a single Ni site as in the case of, e.g., two NO_2 molecules per NiTPP, an area

ratio close to 1:2 in the N 1*s* spectrum is expected from the full coverage observed in the STM images.

To get a hint about the precise adsorption site of the ligand, STM measurements were conducted before and after dosing NO_2 on the NiTPP layer. The images of NiTPP/Cu(100) are shown in Figure 30, top and bottom panels, respectively.

On the copper surface, the NiTPP molecule appears as four bright lobes with a dark depression in the center (see Figure 30, top right) in the STM images. Previously, the lobes and the dark center have been assigned to the four peripheral phenyl rings and the Ni atom,

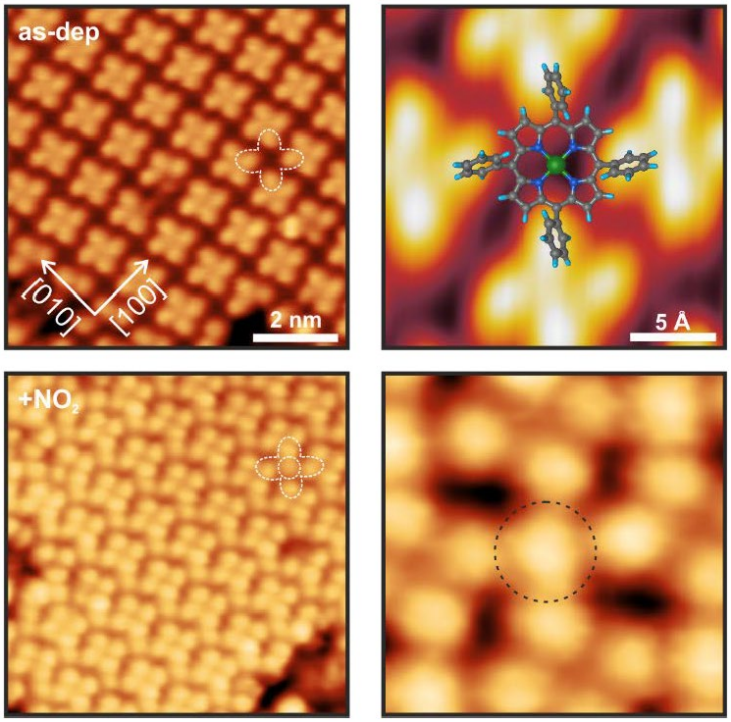

Figure 30) STM images of NiTPP/Cu(100) before and after exposure to 10 L NO_2 acquired at 77 K, top and bottom, respectively. The image size is (8 x 8) nm^2 and the tunneling parameters are V_b = -1 eV, I = 500 pA for the as-deposited sample and V_b = 1 V, I = 200 pA for the exposed sample. Figure adapted from [127].

respectively [13]. After exposure to 10 L of NO_2, circular protrusions (circled in black) appear at the center of the NiTPP, replacing the depression at the center of the macrocycle (see Figure 30, bottom right).

Large-scale STM images in Figure 31 reveal that such features appear on top of almost every Ni site. Thus, we can ascribe them to the NO_2 molecule bound to the nickel ion and deduce that almost every NiTPP hosts one NO_2 molecule, in agreement with the XPS data above. The two domains mirrored by about ± 8° with respect to the [001] direction found previously [13] are visible before and after exposure to NO_2.

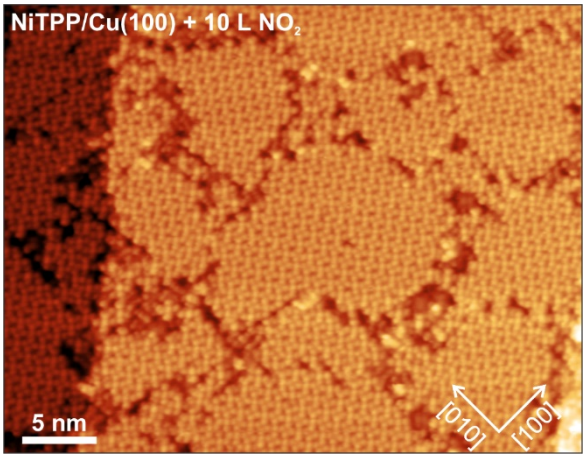

Figure 31) Large-scale STM images of NiTPP/Cu(100) after exposure to 10 L NO_2 acquired at 77 K. The lateral size is (38.8 x 30) nm^2 and the tunneling parameters are: V_b = +1 V, I = 200 pA. Figure adapted from [127].

So far, XPS and STM measurements demonstrate that the Ni(I)TPP/Cu(100) interface is already at room temperature highly reactive to nitrogen dioxide since only small doses in the order of a few Langmuirs are needed to saturate the available Ni adsorption sites.

Having established that NO_2 interacts with the Ni(I)TPP molecule, it shall now be tested whether the +1 oxidation state is crucial for the film reactivity by performing the same experiment on a Ni(II)TPP layer. As demonstrated in section 5.2, the gas-phase +2 oxidation state can be preserved by depositing NiTPP onto the inert O-Cu(100) surface

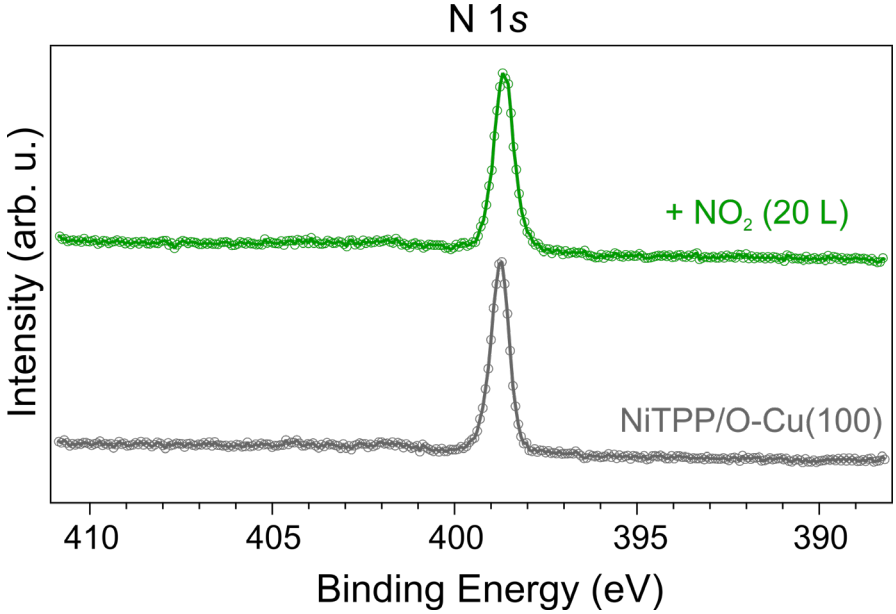

Figure 32) N 1s spectrum of NiTPP/O-Cu(100) before and after dosing 20 L of NO_2. The spectra are measured in a normal emission geometry at a photon energy of hv = 515 eV. Figure adapted from [127].

[89,90]. To exclude the appearance of an additional component in the N 1*s* XPS spectrum, we acquired the photoemission intensity for a binding energy range of more than 20 eV. The spectrum of Ni(II)TPP/O-Cu(100), shown in Figure 32, has a single component around a binding energy of 398.6 eV. Remarkably, even after dosing 20 L of NO_2 to the Ni(II)TPP layer, there is no observable change in the N 1*s* spectrum, and only a single component associated with the nitrogen atoms of the macrocycle is visible. The absence of any additional component, broadening, or change in line shape proves that the nickel is fully inert to NO_2 in the higher (Ni(II)) oxidation state. Therefore, it can be inferred that the surface-induced reactivity of the molecular layer entirely depends on whether the substrate can reduce the chelated nickel ion.

5.3.2. Adsorption geometry of NO_2

The next step involves the investigation of the adsorption geometry of the NO_2 molecules. To this end, we stepwise injected small doses of NO_2 into the chamber by a remote-controlled gas sensing system and took an IRA spectrum after each dosing step. In Figure 33 (a), the spectra of the 1.0 ML sample are shown after three selected NO_2 doses. To single out changes associated with adsorbed NO_2, the spectra are referenced to a background that was measured of the as-prepared NiTPP films.

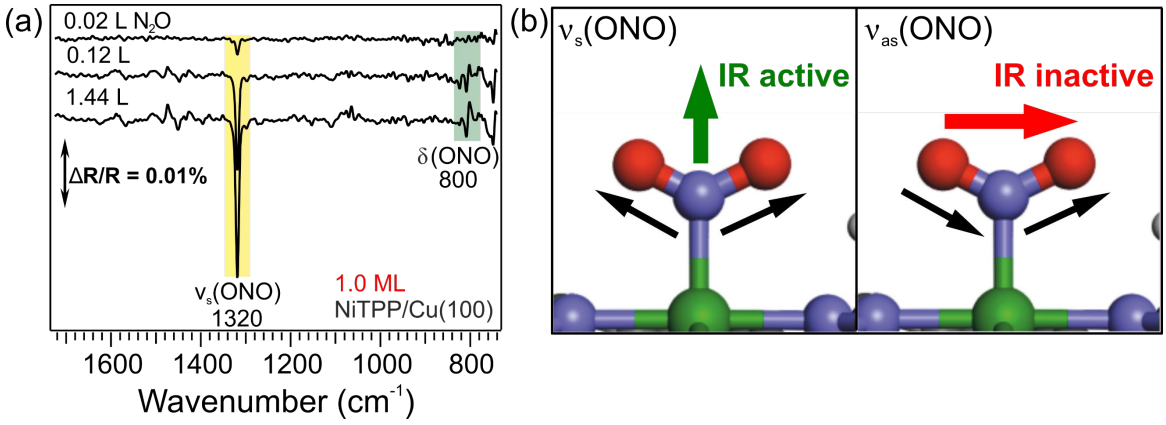

Figure 33) (a) IRA spectra of the NiTPP(1.0ML)/Cu(100) sample measured after exposure to 0.02 L, 0.12 L, and 1.44 L of NO_2. (b) Illustration of the dynamic dipole moment of a symmetric O-N-O stretching ν_s(ONO) and an asymmetric O-N-O stretching ν_{as}(ONO) in the proposed adsorption geometry of the NO_2 molecule. Figure adapted from [127].

Essentially, we observe the growth of two signal components at 1320 and 800 cm^{-1}. In the literature, three main vibrational fingerprints of NO_2 are reported: an asymmetric O-N-O stretching band ν_{as}(ONO) in the 1600-1750 cm^{-1} range, a symmetric O-N-O stretching ν_s(ONO) in the 1200-1300 cm^{-1} and O-N-O bending δ(ONO) in the 750-800 cm^{-1} interval [131–134]. Accordingly, we assign the signals we observe to the symmetric stretching mode ν_s(ONO) and an O-N-O bending δ(ONO). Notably, in the typical range of an asymmetric O-N-O stretching, the spectrum is absent of any feature. A possible explanation for this could lie in the adsorption geometry. If the NO_2 molecule adsorbs such that the asymmetric O-N-O stretching causes a change in the dynamic dipole moment, which is entirely parallel to the surface, it cannot be detected via IRAS due to the MSSR [84]. This is the case for adsorption in a "V" shaped configuration, i.e., the molecule binds to the central Ni atom of NiTPP through its nitrogen atom oriented such that its two oxygen atoms pointing upwards. As shown in Figure 33 (b), this would lead to an IR active symmetric stretching mode ν_s(ONO) and an IR inactive asymmetric mode ν_{as}(ONO). This geometry is also in line with previous STM reports. As the NO_2 molecule performs a fast (compared to the STM acquisition mode) precession motion, it gives rise to a time-averaged disc-shaped appearance in the topographic STM images, instead of two lobes as expected for a steady molecule [135].

5.3.3. Electronic properties of NO_2-NiTPP/Cu(100)

While we already know the Ni oxidation states for the Ni(I)TPP/Cu(100) and Ni(II)TPP/O-Cu(100) interfaces, it is still to be determined for NO_2-NiTPP/Cu(100). This can be accessed by NEXAFS measurements at the Ni L_3-edge. In analogy to the comparison between the spectra of NiTPP on the bare and passivated Cu surfaces, we first compare the NEXAFS spectra (acquired in s-polarization) of NO_2-NiTPP/Cu(100), to the case of Ni(I)TPP/Cu(100). The corresponding spectra are shown in Figure 34.

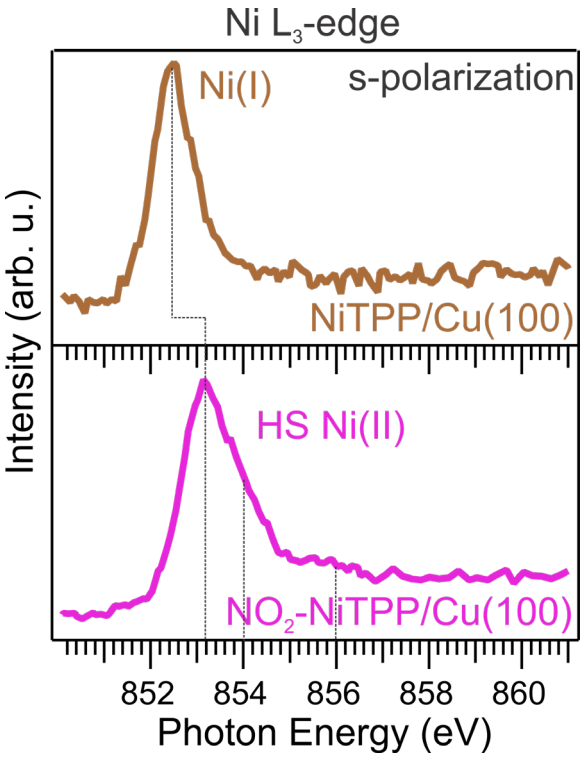

Figure 34) NEXAFS spectra acquired at the Ni L_3-absorption edge of NiTPP/Cu(100) (top) and NO_2-NiTPP/Cu(100) (bottom). Figure adapted from [127].

After dosing 10 L of NO_2, a remarkable change in the spectral line shape (bottom panel) can be observed. The centroid is shifted toward higher photon energies by 0.8 eV (to 853.2 eV), and a pronounced shoulder appears at 854 eV. In addition, a new broad resonance appears around 856 eV. Both line shape and energy position of the main resonance match the reports of compounds including nickel atoms in a Ni(II) oxidation state with two unpaired electrons [136]. Hence, this gives evidence for a reoxidation of the metal center through coordination with the NO_2 ligand from Ni(I) to Ni(II). Moreover, the shoulder at higher photon energy is a characteristic marker of the configuration with two partially filled $3\,d$ orbitals in nickel complexes and metalloproteinases [38,137–139]. Hereafter, a configuration with unpaired electrons is referred to as high spin (HS), whereas the configuration with paired spins only will be noted as low spin (LS). This must not be confused with the designation typically used for spin-crossover complexes, as in our case, the t_{2g}-orbitals are fully occupied for both the HS and LS configuration. The d^8 HS configuration is also in line with the Ni $2p_{3/2}$ XPS spectra presented in section 5.3.1.

At this point, NEXAFS provides evidence for three different spin configurations, namely d^9, HS d^8, and LS d^8 for NiTPP/Cu(100), NO_2-NiTPP/Cu(100), and NiTPP/O-Cu(100),

respectively. Since the three configurations should lead to different imbalances of unoccupied d states, a suitable way to confirm this interpretation is given by XMCD measurements.

The XMCD signals at the $L_{2,3}$-edge for the three samples in a normal and grazing incidence geometry were measured at a sample temperature of 3 K and an external magnetic field of 6.8 T. They are shown together with the absorption signals of left- and right-hand circularly polarized light, respectively, are shown in Figure 35.

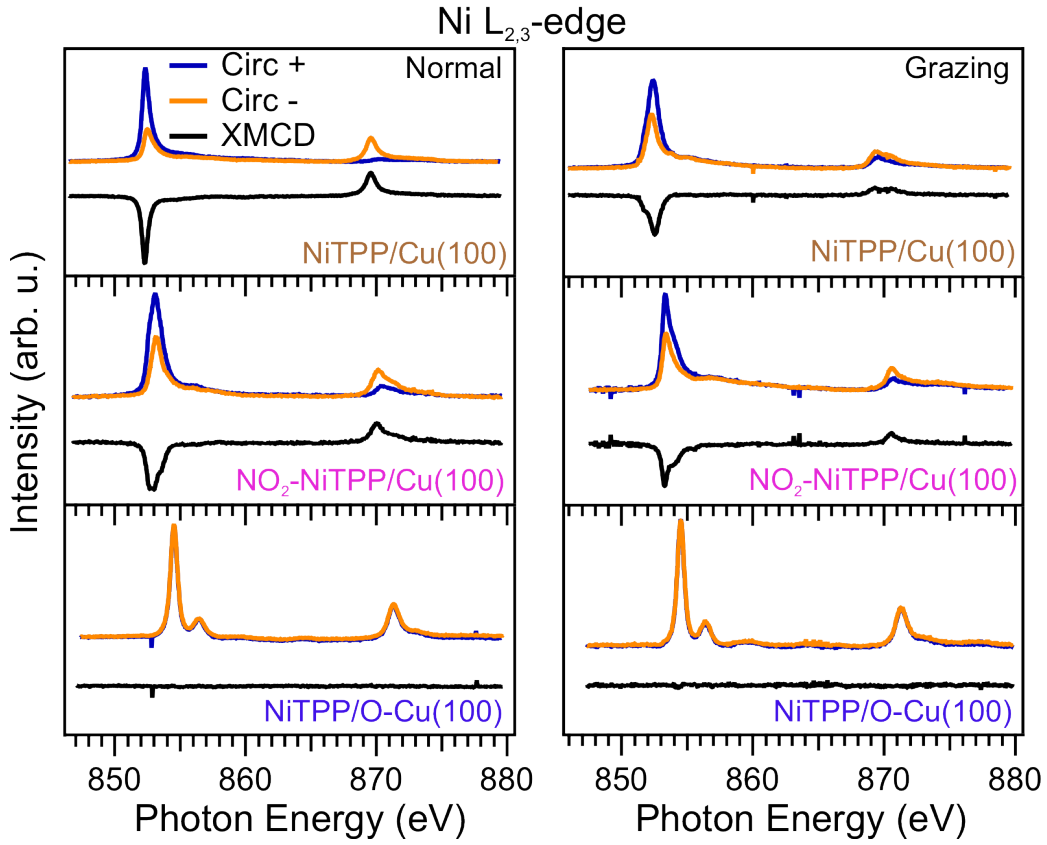

Figure 35) Absorption spectra at the $L_{2,3}$-edge of left- and right-hand circularly polarized light and the resulting XMCD signal for normal (left) and grazing (right) incidence. The spectra were acquired while an external field of 6.8 T was applied and the samples were cooled to 3 K. Figure adapted from [127].

As expected from the LS d^8 configuration suggested by NEXAFS, there is no XMCD signal detected for NiTPP/O-Cu(100). As in this configuration, there are no unpaired electrons in the d shell that can be aligned with an external field, no difference in the absorption of left- and right-circularly polarized light can be detected.

Instead, clear dichroism points toward unpaired electrons for NiTPP molecules in direct contact with the Cu(100) substrate. Even after the adsorption of NO_2, which was suggested to result in a d^8 configuration by NEXAFS, the XMCD signal is not quenched. This supports the interpretation that even though a transition from the d^9 to the gas-phase-like d^8 oxidation state takes place, there are still unpaired electrons as the d shell is in an HS configuration.

A sum rule analysis can provide the effective spin moment ($m_{s,eff}$) [76] and the orbital moment (m_l) [75] for further insights into the magnetic configuration of the samples. However, to ensure that the sum rule analysis does not underestimate the magnetic moments due to lacking saturation, the hysteresis curves in Figure 36 were measured first.

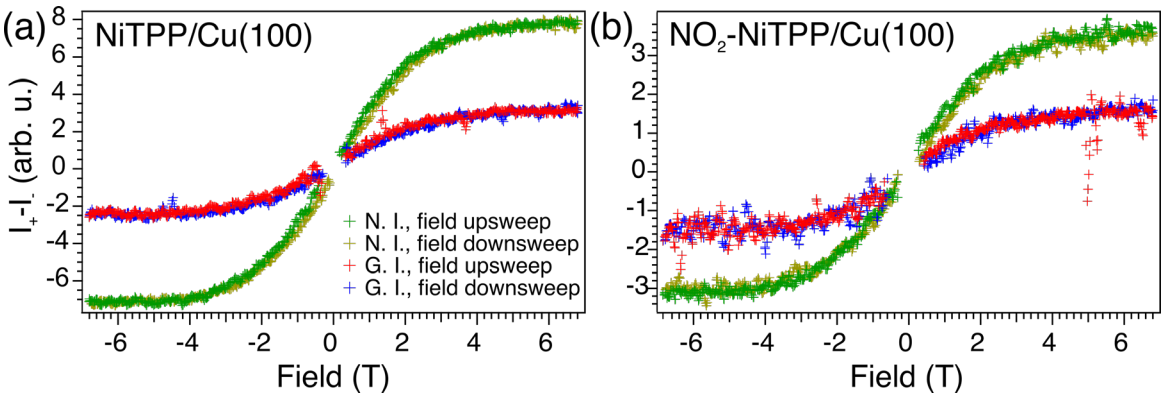

Figure 36) Magnetic hysteresis curves for NiTPP/Cu(100) (left panel) and NO_2-NiTPP/Cu(100) (right panel) measured at a temperature of 2 K. For both systems, magnetic saturation is reached in a normal incidence (N. I., yellow and green curves) and grazing incidence (G. I., blue and red curves) geometry. Due to experimental artefacts measured at low external fields, the data points have been removed in a small range around 0 T. Figure adapted from [127].

The absorption measured while sweeping the field from -6.8 to 6.8 T (6.8 to -6.8 T) is referred to as upsweep (downsweep). From the hysteresis curves in Figure 36 (a), it can be seen that magnetic saturation is reached for NiTPP/Cu(100) in a normal incidence (N. I., yellow and green markers) and a grazing incidence (G. I., blue and red markers) geometry. Moreover, it can be observed that while saturation is reached at the same value of the applied field in the two geometries (± 5 T), the absolute value is much lower at grazing incidence. Within the limits of our accuracy, no residual magnetization without an externally applied field could be detected. The same behavior can be observed for NO_2-NiTPP/Cu(100) in Figure 36 (b). Notably, even though the total values of the XMCD magnitudes are smaller, the anisotropy is neither lifted nor inverted.

Since all the hysteresis curves reach a slope of zero at external fields of around ± 5 T, we can assume that our XMCD measurements, taken at 6.8 T, were performed in magnetic saturation. As anticipated in section 4.2.2, the evaluation of the sum rules requires certain assumptions about the isotropic absorption intensity I_{iso}. The approximations used here are described in appendix A.1. The results of the sum rule analysis are shown in Table 1.

	Normal incidence	Grazing incidence
NiTPP/Cu(100)		
$m_{s,eff}$	(1.64 ± 0.09) μ_B	(0.39 ± 0.05) μ_B
m_l	(0.22 ± 0.02) μ_B	(0.08 ± 0.01) μ_B
NO_2-NiTPP/Cu(100)		
$m_{s,eff}$	(2.76 ± 0.2) μ_B	(0.73 ± 0.05) μ_B
m_l	(0.29 ± 0.05) μ_B	(0.18 ± 0.01) μ_B

Table 1) Effective spin moments and orbital moments of NiTPP/Cu(100) and NO_2-NiTPP/Cu/(100), in normal and grazing incidence, respectively, resulting from the sum rule analysis of the spectra shown in Figure 35.

For NiTPP/Cu(100), the values for the effective spin moment in normal and grazing incidence are (1.64 ± 0.09) μ_B and (0.39 ± 0.05) μ_B, respectively. These values can be compared to those for CuPc/Ag(100) [140], as the Cu ion is in a very similar crystal field and is in a $3d^9$ configuration like in our system. Indeed, the sum rule analysis for this system resulted in (1.67 ± 0.08) μ_B and (0.35 ± 0.08) μ_B [140], which is very similar to our values. For NO_2-NiTPP/Cu(100), the effective spin moment is (2.76 ± 0.2) μ_B. As in an HS d^8 and d^9 configuration, the electrons in the energetically highest orbitals (e_g orbitals) do not carry orbital angular momentum, the values of the effective spin moment can, in a first approximation, be compared to the moments resulting from the spin-only formula $\mu_s = \sqrt{n(n+2)}\mu_B$, which neglects orbital contributions to the total magnetic moment. Indeed, with values of 1.73 μ_B and 2.83 μ_B for one ($n = 1$) and two ($n = 2$) unpaired electrons, respectively, they lie within the uncertainty of our measurements.

Another striking property is that the effective spin moment is strongly anisotropic in both systems. As mentioned in section 4.2.2, the effective spin moment $m_{s,\mathrm{eff}}$ is the sum of the actual spin moment m_s and the dipolar spin term $7\langle T_\Theta \rangle$. To disentangle the different contributions and thereby directly access m_s, calculations [79] or additional measurements are required, as described in appendix A.2. In low-symmetry environments, such as the macrocycle that surrounds the Ni atom in NiTPP, the dipolar spin term can show a pronounced angular dependence, whereas m_s itself can be regarded as isotropic due to the low spin-orbit coupling [140,141]. Therefore, we tentatively ascribe the high anisotropy to the $7\langle T_\Theta \rangle$ term and assume, based on the NEXAFS results above, $m_s = 1\,\mu_B$ for the NiTPP/Cu(100) (S = 1/2) and $m_s = 2\,\mu_B$ for the NO_2-NiTPP/Cu(100) (S = 1).

We now focus on the orbital magnetic moment m_l, which has usually more impact on the crystal-field-induced magnetic anisotropy of transition metal atoms than m_s. We note that for the pristine molecular film, the out-of-the-plane component is 275 % higher than the in-plane one. Although the anisotropy of m_l does not reach the extremely high values around 420 % found for the CoOEP/graphene [141], it is comparable to that measured at the same incident angle for CuPc/Ag(100) (290 %) [78], and higher than the one of the Fe-TPA_4/Cu(100), which is around 190 % [116].

Upon exposure of the NiTPP/Cu(100) interface to NO_2, the m_l anisotropy remains out-of-the-plane but decreases from 275 % to 161%. This behavior differs from what is reported for similar systems, where an external ligand was adsorbed atop a coordinated metal ion. In those cases, the magnetic anisotropy is either almost quenched (as found for CO-CoOEP/graphene) [141] or inverted (observed for O_2-Fe-TPA_4/Cu(100)) [116]. For ferromagnets, it is well known that magnetic anisotropy determines the stability of the magnetization in bulk as well as in nanoparticles [137]. The fact that the magnetic anisotropy does not change even in the presence of the external ligand is of interest for the engineering of information storage devices at the atomic scale. In the present case, the NO_2 adsorption changes the spin configuration but not the anisotropy. This matches the results from the sum rule analysis, which suggested that electrons in the singly occupied *d* orbitals do not carry orbital angular momentum.

To further support the interpretation of the experimental observations regarding the 3d shell occupation, additional DFT calculations were performed. The DFT calculations in this work were performed by Andreas Windischbacher and Peter Puschnig from the Institute of Physics of the University of Graz, Austria. The computed density of states projected (PDOS) onto the different Ni 3d orbitals for NiTPP/Cu(100), NO_2-NiTPP/Cu(100), and NiTPP/O-Cu(100), from top to bottom, is shown in Figure 37.

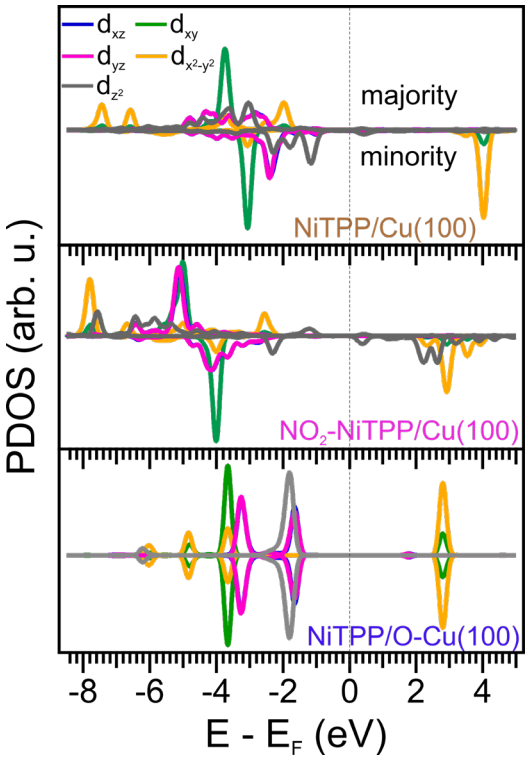

Figure 37) Density of states projected onto the different d states of the central Ni atom for the majority and minority spin channels of NiTPP/Cu(100), NO_2-NiTPP/Cu(100), and NiTPP/O-Cu(100) (from top to bottom). Figure adapted from [127].

NiTPP/O-Cu(100) has the same electron distribution for both, majority and minority spin channels. Together with the major contribution of both $d_{x^2-y^2}$ orbitals (yellow) above the Fermi level, this supports the NEXAFS results given above, suggesting a gas-phase-like $(d_{xy})^2$ $(d_{yz}, d_{xz})^4$ $(d_{z^2})^2$ $(d_{x^2-y^2})^0$ (S = 0) configuration on the oxygen-reconstructed copper surface. It is also perfectly in line with the missing XMCD signal, as such a configuration has only paired spins and, thus, no imbalance in the spin polarization of unoccupied 3d states.

For NiTPP/Cu(100), in contrast, a strong realignment of the 3d levels can be observed. In line with the previously found change of the Ni oxidation state [14], only one spin channel of the $d_{x^2-y^2}$ has a major contribution above the Fermi level resulting in a $(d_{xy})^2$ $(d_{yz}, d_{xz})^4$ $(d_{z^2})^2$ $(d_{x^2-y^2})^1$ occupation. The unpaired electron leads to a total spin of S = 1/2 and, therefore, causes a paramagnetic ground state configuration of the central Ni atom.

The coordination of NO_2 causes another significant realignment of the electronic energy levels. In addition to the $d_{x^2-y^2}$ orbital (yellow), the d_{z^2} orbital (grey) also has its major contribution above the Fermi level now. This corresponds, in first approximation, to a

$(d_{xy})^2$ $(d_{yz}, d_{xz})^4$ $(d_{z^2})^1$ $(d_{x^2-y^2})^1$ configuration and, therefore, agrees well with the HS d^8 configuration suggested by the NEXAFS analysis. Furthermore, the XMCD signal and the magnetic moments obtained by the sum rule analysis corroborate the electronic structure with two unpaired electrons below (or holes above) the Fermi level.

The DFT calculations also revealed substantial differences in the calculated intramolecular bond lengths. For NiTPP/O-Cu(100), the relaxed geometry of the molecule is typical of the conjugated porphyrin macrocycle in the gas phase state (~ 1.39 Å for C-N bonds) [142,143]. Instead, when NiTPP is in direct contact with copper, the bond lengths vary due to the strong hybridization. With a bond length of 1.44 Å at the conjugated porphyrin system, it is clearly elongated and rather typical of a single bond character. This can be ascribed to the filling of the formerly unoccupied antibonding π^* states in the course of the charge transfer, as they are predominately located at the macrocycle. The DFT optimized structure after adsorption of the NO_2 molecule is shown in Figure 38 (a). Ligation by the additional NO_2 ligand causes only slight changes in the NiTPP adsorption structure. This is indicated by the DOS projected onto the macrocycle of the molecule, shown in Figure 38 (b). In the range of -1.5 eV up to around 2 eV around the Fermi level, only minor differences between the PDOS of the two systems (with and without NO_2) can be seen.

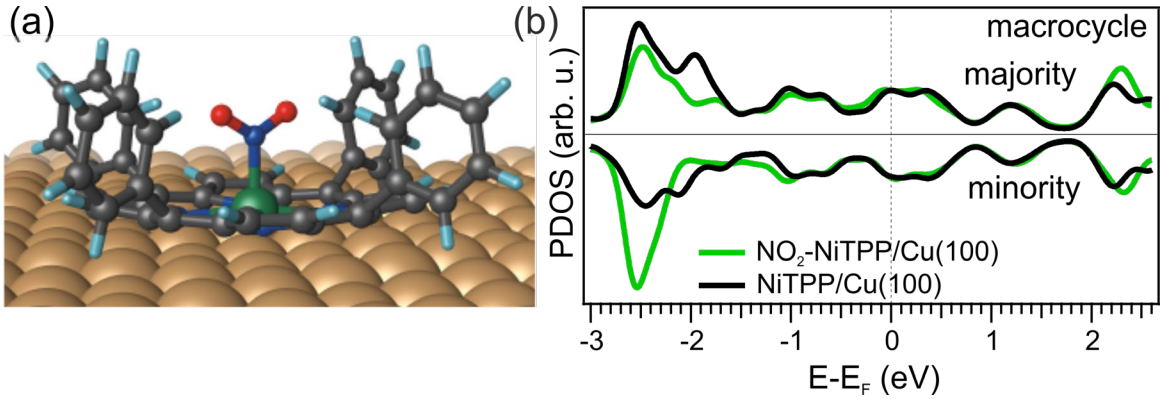

Figure 38) (a) Model of the DFT optimized geometry of NO_2-NiTPP/Cu(100). (b) DOS projected onto the NiTPP macrocycle for NiTPP/Cu(100) and NO_2-NiTPP/Cu(100). Around E_F, only minor NO_2-induced deviations can be oberved. Figure adapted from [127].

Experimentally, this scenario is further confirmed by NEXAFS measurements at the N K-edge of the two systems. The NEXAFS spectra for both systems acquired in an s- and p-polarization geometry, respectively, are shown in Figure 39. The spectrum of the pristine NiTPP/Cu(100) interface obtained with p-polarized light (black, top) mainly features three components, B_N, C_N, and D_N, at photon energies of 398.7 eV, 400.6 eV, and 401.6 eV, respectively. These features were previously assigned to π^* resonances associated with N 1*s*→LUMO/LUMO+1 and LUMO+3 [14,90] and, thus, are barely visible in the s-pol spectra due to the flat absorption geometry of the macrocycle, as discussed in section 5.2.3. After NO_2 ligation, a new feature appears around 402.3 eV with a shoulder at 401.5 eV. This feature, labeled E_{NO_2}, can be assigned to the π^* resonance of NO_2 [138,139]. This resonance is barely visible in the spectrum acquired with s-polarized light, providing further evidence that the NO_2 molecule adsorbs in a "V" shaped configuration with a mainly upward pointing N-O bond, as already suggested by the IRAS measurements and DFT

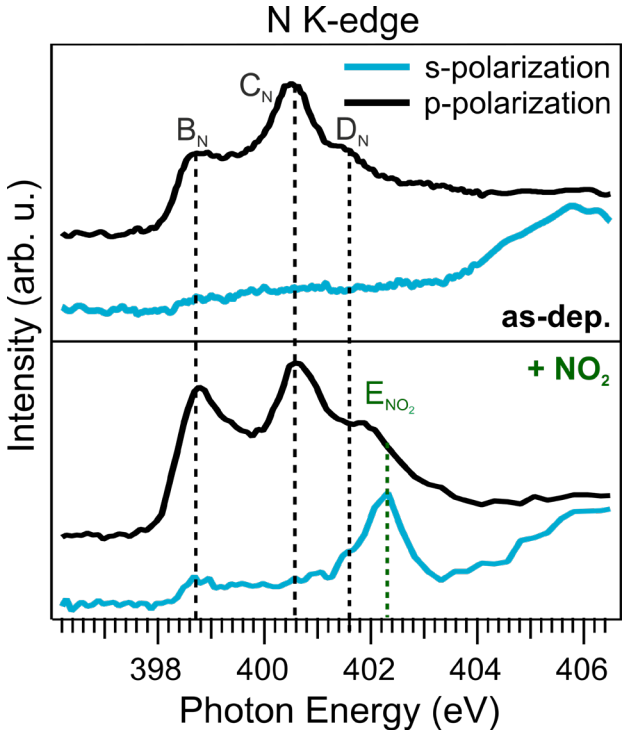

Figure 39) N K-edge absorption spectra of NiTPP/Cu(100) (top) and NO_2-NiTPP/Cu(100) (bottom). Figure adapted from [127].

predictions above. Remarkably, after NO_2 coordination, only a moderate increase of the resonances B_N and C_N can be observed. Hence, the charge transfer from the copper surface to the macrocycle vastly persists throughout the NO_2 adsorption.

The fact that DFT calculations and NEXAFS measurements unanimously indicate that the strong interaction between the substrate and the macrocycle is conserved proposes that almost exclusively the Ni atom is interacting with the NO_2 molecule. Due to the surface-*trans* effect, the Ni center is pulled away from the copper surface by 0.2 Å. However, the strong macrocycle-substrate interaction seemingly acts as a counterpart to this increase of the Ni-Cu distance. Remarkably, for other porphyrin-metal interfaces, the surface-*trans* effect was reported to lift the entire molecules away from the surface after adsorption of NO [38,40] and even ammonia (NH_3) [10,144], which has an even weaker charge donation ability [126]. The absence of substantial changes in the porphyrin macrocycle leaves the NO_2 molecule primarily responsible for causing the spin-switching. To support this hypothesis, we did a comparison between the DOS projected onto the NO_2 for the strongly interacting NiTPP on bare Cu(100) and surface-decoupled NiTPP on O-Cu(100). It shall be emphasized that while the former system was successfully prepared in the experiment, there was no NO_2 uptake by the NiTPP on the oxygen-reconstructed surface observed at room temperature. Therefore, the NO_2-NiTPP complex on the O-Cu(100) surface is only a hypothetical system that serves as a reference for the interaction with a NiTPP molecule, which is only weakly influenced by the substrate. The corresponding PDOS are shown in Figure 40.

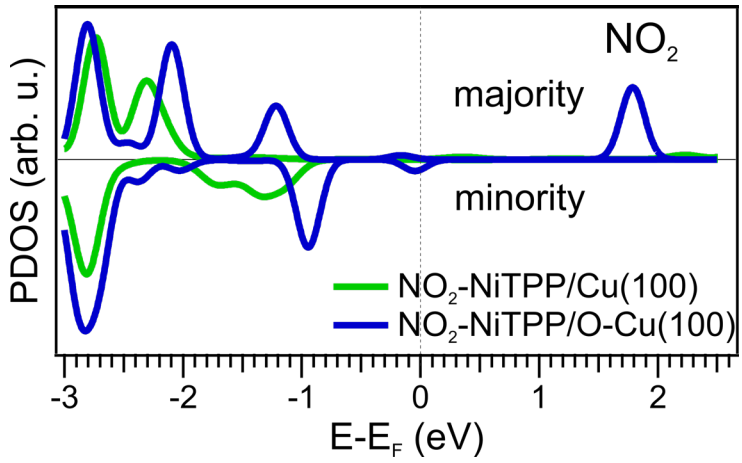

Figure 40) DOS projected onto the NO_2 molecule for the NO_2-NiTPP/Cu(100) interface and a hypothetical NO_2-NiTPP complex on the O-Cu(100) surface. Figure adapted from [127].

Comparing the PDOS of the two systems, it can be seen that only one spin channel of the NO_2-NiTPP complex on the passivated O-Cu(100) surface has a significant contribution above the Fermi level. In contrast, there is no contribution above Fermi on the bare Cu(100) substrate.

While the former is expected from the radical nature of NO_2, the latter strongly suggests an electron uptake by the NO_2 molecule. Remarkably, the electron uptake does not cause a gas-phase-like d^8 LS configuration but an HS complex. This was similarly found for the NiTPP-L_2 complex (L = piperidine) in solution, where the piperidine is coordinated to both axial coordination sites of the porphyrin molecule [41]. For the present system, DFT calculations suggest that the substrate and the NO_2 molecules have a similar impact. Upon NO_2 ligation, the Ni-Cu distance increases from a value of 1.85 to 2.05 Å, similar to the Ni-NO_2 distance of 2.0 Å. Hence, the coordination of the Ni atom changes from a square-based pyramid to an almost octahedral symmetry. As discussed in section 2.1, such a crystal field gives rise to an HS ground state configuration, as already observed for NiTPP-L_2 complexes [41,145].

5.3.4. Interface properties

After the electronic configuration of the Ni 3*d* shell and the adsorption geometry of the NO_2 molecules were determined, the adsorption behavior of NO_2 under more applicative conditions is tested as a next step. In this regard, an intricate understanding of the chemical properties of buried interfaces is of great importance to improve device performance, e.g., of photovoltaics [146]. To understand the effect of coverages above 1 ML, we injected small doses of NO_2 stepwise into the chamber by a remote-controlled gas dosing system and followed the uptake for three different thicknesses of the NiTPP layer by IRAS. We prepared three samples, namely 1.0, 2.5, and 5.0 ML of NiTPP on Cu(100), and took an IRA spectrum after each dosing step. To single out changes associated with adsorbed NO_2, the spectra are referenced to a background that was measured of the as-prepared NiTPP films. In Figure 41, the IRAS spectra of the three different samples taken after different dosing steps are plotted.

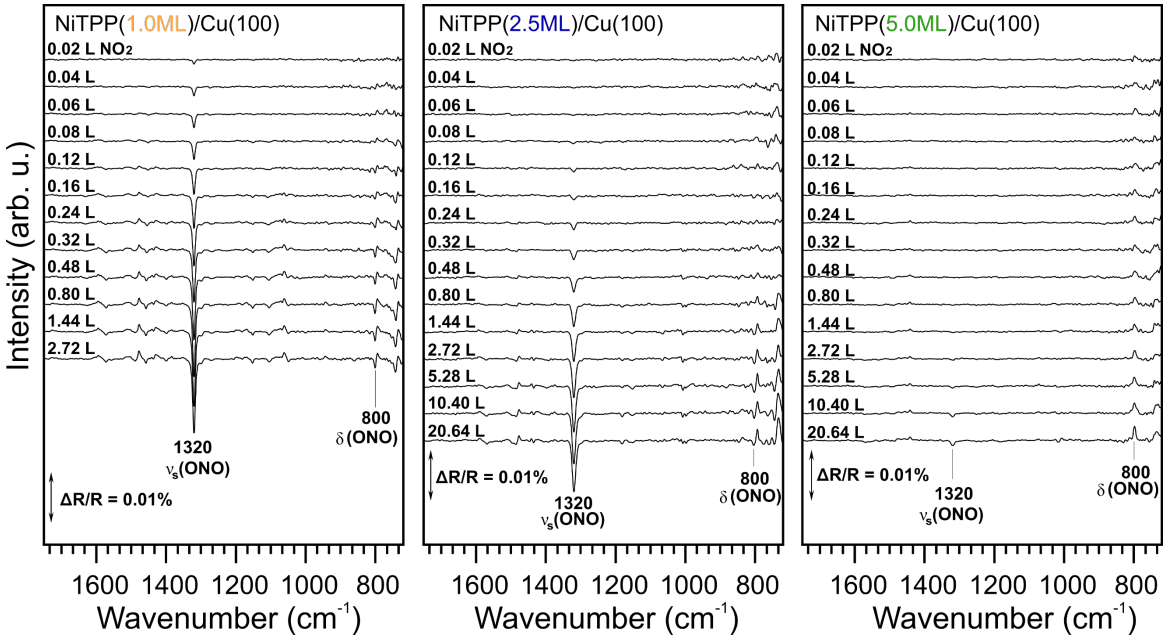

Figure 41) IRA spectra of three samples with NiTPP film thicknesses of 1.0 (left), 2.5 (middle), 5.0 (right) monolayers after different doses of NO_2. Figure adapted from [127].

Essentially, we observe the growth of the two signal components for symmetric O-N-O stretching ν_s(ONO) and an O-N-O bending δ(ONO) at 1320 and 800 cm^{-1} for all three samples. However, the peak height dependence on the dose significantly differs for the different NiTPP thicknesses. While after dosing NO_2 to the 1.0 ML sample, a sharp feature with relatively high intensity is already visible after 2.72 L, the relative intensity of this peak is much lower for the 2.5 ML sample. In fact, even after a much higher dose of 20.64 L, the relative intensity is still lower. For the 5.0 ML sample, this effect is even more severe.

The different peak height dependences on the NO_2 dose of the three samples are visualized in Figure 42 using the example of the ν_s(ONO) component at 1320 cm^{-1}.

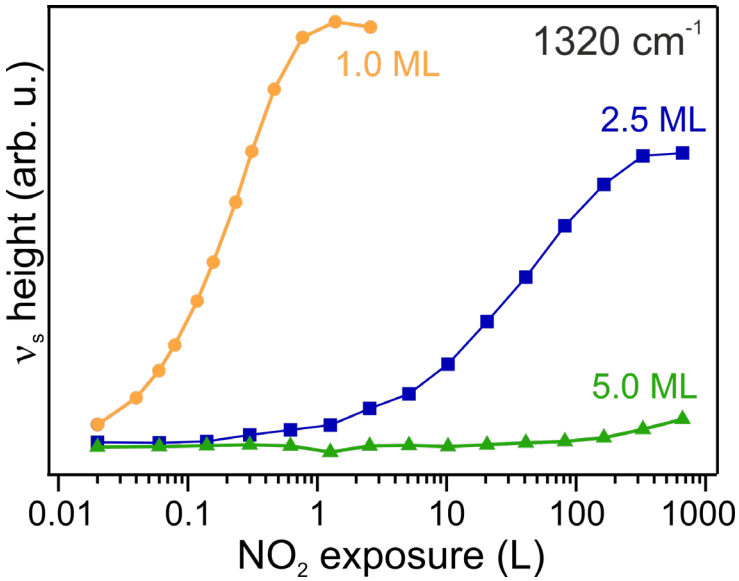

Figure 42) Peak height dependence of the ν_s(ONO) stretching mode on the NO_2 dose for the three NiTPP film thicknesses. Figure adapted from [127].

From the semilogarithmic plot, it can be seen that for increasing film thicknesses, the required doses to reach saturation drastically increases while the maximum intensity at saturation decreases. This behavior suggests that NO_2 does not adsorb on the upper molecule layers, which have a Ni(II) oxidation state, but diffuses through the upper layers until it adsorbs on the first monolayer in the same "V"-shaped geometry as on the monolayer sample. Thus, the different growth rates are in line with the fact that Ni(II)TPP molecules, present from the second layer on, are inert to NO_2. This also confirms the interpretation of the N 1*s* measurements of NiTPP/O-Cu(100) after exposure to NO_2 presented above (see Figure 32). In conclusion, the reactivity to NO_2 is an interfacial property, which is preserved when the NiTPP/Cu(100) interface is buried in a multilayer sample.

The possibility to selectively stabilize gas molecules even at the buried interface makes NiTPP/Cu(100) an interesting candidate for potential sensing applications. However, for many of these applications, it is necessary to restore the properties of the pristine interface by external stimuli [9,147]. A common means is the thermal annealing of such systems [10,40]. For the present system, we observe that by gentle annealing up to 390 K, the pure NiTPP film can be restored after NO_2 adsorption.

In Figure 43, STM images of the Ni(I)TPP/Cu(100) samples are shown after deposition, after exposure to 10 L of NO_2, and after annealing at 390 K.

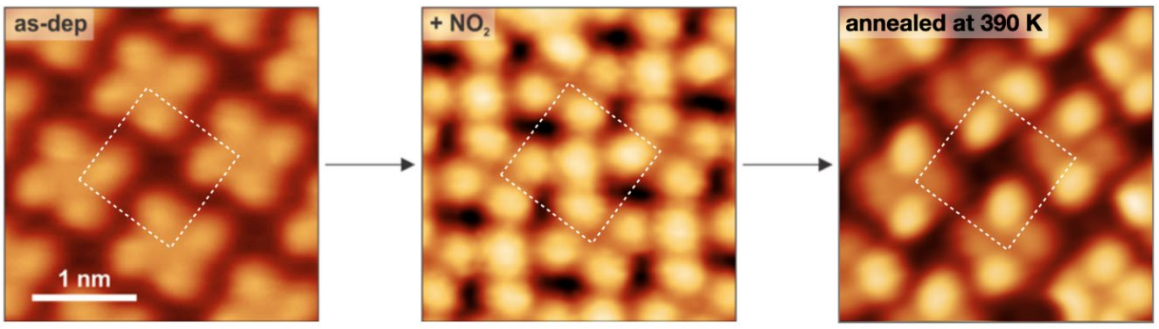

Figure 43) STM images of NiTPP/Cu(100) before (left) and after (middle) exposure to 10 L NO2, and after annealing (right) up to 390 K. A single NiTPP molecule is framed with a dashed white square to guide the eye. All images are acquired at 77 K. Image size 3x3 nm. The tunneling parameters are (left) V_b = -1 V, I = 500 pA, (centre) V_b = +1 V, I = 200 pA, (right) V_b = -1 V, I = 200 pA. Figure reproduced from [127].

As described above, after dosing the gas, bright protrusions appear at the center of the four bright lobes of a single NiTPP molecule. After annealing, these bright protrusions are replaced again by dark depressions, indicating desorption of the NO_2 molecules. Moreover, some of the bright lobes associated with the peripheral phenyl rings turn dark. This phenomenon can be ascribed to a flattening [47], which will be investigated in detail in section 5.4.

5.3.5. Conclusions

Altogether, the results presented in this section suggest that the NiTPP/Cu(100) interface can be viewed as two mostly independent subsystems: the Ni center and the porphyrin macrocycle.

The Ni center of the molecule mainly determines the spin state. Through the choice of a proper substrate, its oxidation state (and therefore also its spin configuration) can be precisely tuned. On the oxygen-passivated substrate, it retains its gas-phase-like $(d_{xy})^2$ $(d_{yz}, d_{xz})^4$ $(d_{z^2})^2$ $(d_{x^2-y^2})^0$ (S = 0) configuration. The previously found charge transfer changes the oxidation state from +2 to +1, leading to a $(d_{xy})^2$ $(d_{yz}, d_{xz})^4$ $(d_{z^2})^2$ $(d_{x^2-y^2})^1$ occupation with one unpaired electron (S = 1/2). Spin and oxidation state can be additionally tuned to a $(d_{xy})^2$ $(d_{yz}, d_{xz})^4$ $(d_{z^2})^1$ $(d_{x^2-y^2})^1$ configuration by a modification of the crystal field in the form of NO_2 coordination. Approximating the surroundings of the Ni ion with a O_h, C_{4v} and D_{4h} symmetry, the energetic order of the highest orbitals agrees with what would be expected from crystal field theory, as summarized in Figure 44.

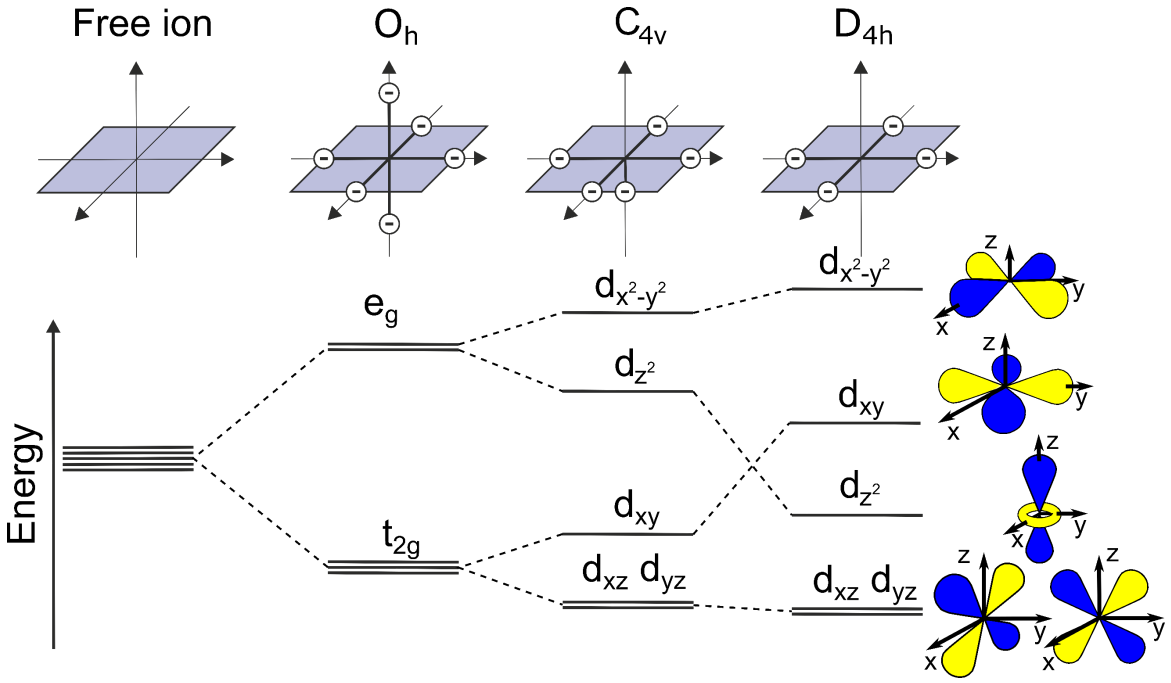

Figure 44) Energy splitting of the *d* orbitals of a transition metal ion in different crystal field symmetries. With nine electrons, the only singly occupied state is the energetically highest $d_{x^2-y^2}$ orbital. With eight electrons, there are either two unpaired spins in an O_h symmetry or only paired spins in a D_{4h} symmetry. The unperturbed *d* orbitals are shown at the right of the energy levels.

Instead, the second subsystem, i.e., the macrocycle, is only weakly perturbed by the interaction with the NO_2 ligand. Thanks to the exceptionally strong molecule-surface interaction, the energy level alignment of the frontier orbitals that are mainly located at the macrocycle remains vastly unaltered, as shown in Figure 38 (b).

In that sense, NiTPP/Cu(100) can be considered as a highly versatile platform for realizing multifunctional molecular units, as specific properties can be selectively addressed by deploying corresponding stimuli. The magnetic properties can (even at room temperature and in a buried interface) be tuned by NO_2 coordination, whereas the charge carrier transport and optical properties could be controlled independently by electric fields or light.

5.4. Stability against thermally induced chemical modifications

It was shown in section 5.3 that the NiTPP/Cu(100) interface is an attractive candidate for potential applications: the adsorption of NO_2 induces total spin switching from S = 1/2 to S = 1 without significantly changing the anisotropy. Many applications based on the absorption of small molecules at metal-organic interfaces require regeneration of the pristine interface. The axial coordination of small trace gases to self-assembled porphyrin arrays can open paths to conceivable applications in several fields, e.g., sensing [45], spintronics [6], and catalysis [148]. However, after binding the ligand, the possibility to restore the original electronic properties is vital for engineering non-degradable sensors, selective switching of the magnetic anisotropy, and the turnover of single-atom catalysts.

One of the most common and effective means to remove small molecules bound to porphyrin arrays that are adsorbed on metallic substrates is temperature annealing [10,12,149]. In powders, porphyrin molecules can be annealed up to high temperatures without suffering from chemical modifications. When deposited on a surface, however, the molecule-substrate interaction drastically affects the thermal stability. On weakly interacting surfaces, the molecules may desorb before the coordinated ligand has been removed. On strongly interacting surfaces, the thermal decomposition of the molecules can lead to irreversible and uncontrolled changes of the molecular array, which is a major bottleneck for the use in high-temperature rated devices. On standard electrode templates, e.g., Cu, Ag, and Au, on-surface annealing was reported to promote the partial dehydrogenation of polycyclic aromatic hydrocarbons, which can lead to the formation of oligomers [150,151]. For porphyrins and phthalocyanines, several publications reported structural changes where the periphery of a molecule undergoes dehydrogenation and ring-closing reactions [36,152,153] and commit bonding to the macrocycle of the molecules [34,64,94,154,155]. Once the electronic structure is changed, this can lead to macroscopically detectable changes. This was observed for Fe octaethyl porphyrin on an Au(111) substrate, for which the temperature-induced cyclodehydrogenation leads to an irreversible modification of the effective spin moment [35].

This section investigates the thermal stability against structural changes, which is key to the reversibility of such processes. Since it was already shown that the Ni(I) oxidation state is a necessary condition for the reactivity to NO_2, the conservation of this re-oxidized state upon annealing up to 620 K is tested.

5.4.1. Molecular unit cell

First, the topography of the molecular film is examined by means of STM. Constant-current STM images of the as-deposited NiTPP/Cu(100) surface and after two additional annealing steps are shown in Figure 45 (a). Immediately after deposition, a single NiTPP molecule appears as the familiar four bright lobes with a dark depression in the center, as shown in the previous section. Subsequently, the sample temperature was increased to 420 K for 5 minutes. After waiting for the sample to cool down back to room temperature, some lobes have a reduced contrast in the STM images taken at 77 K. After another annealing step to 530 K for 5 minutes and subsequent cooling time, the share of dimmed phenyls increases. The contrast polarity is independent of the bias and tunneling current. A statistical analysis of large-scale STM images revealed that after annealing up to 420 K, 51 ± 7 % of the phenyls have a dimmed intensity which increased after the second annealing step (530 K) to 87 ± 9 %. There is no particular observable order in the decrease in intensity, but the pristine and modified phenyls (bright and dim, respectively) are randomly distributed, i.e.,

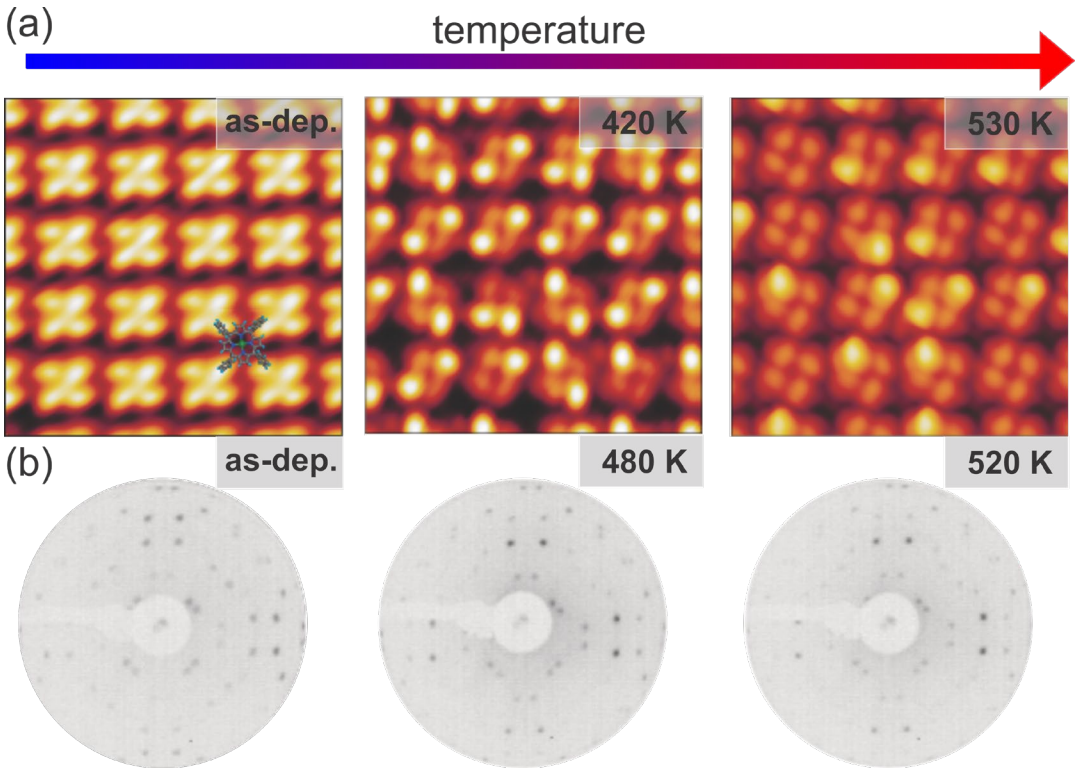

Figure 45) (a) STM images of NiTPP/Cu(100) after deposition and after two subsequent annealing steps. The images have a lateral size of (5.0 x 5.0) nm^2 and were acquired at 77 K with tunneling parameters of left: V_b = -1.5 V, I = 50 pA, center: V_b = -0.8 V, I = 100 pA, right: V_b = -0.5 V, I = 500 pA. A ball-and-stick model of an adsorbed NiTPP molecule is superimposed to the STM image of the as-deposited NiTPP film. (b) LEED images of the as-deposited NiTPP/Cu(100) surface and after two annealing steps to 480 K and 520 K, respectively. The images were acquired at electron energies of 20 eV. Figure adapted from [47].

there is no preference for single molecules observable. Also, no systematic influence on the contrast of neighboring NiTPP molecules can be observed. Such a decrease in the contrast was already observed on copper [64,94,156,157] and silver [154,155,158] substrates and ascribed to a flattening due to partial dehydrogenation and subsequent ring-closure reactions. However, NiTPP molecules are expected to have a larger footprint with four peripheral phenyl groups aligned coplanar to the macrocycle ring. Thus, the distance

between adjacent molecules is expected to increase in this scenario due to the steric interactions. For different flat conformations reported in the literature, e.g., on silver, the spiral, rectangular, and hybrid conformation [154,155,158], this was reported to affect the surface phase density and symmetry [159]. In our STM images (Figure 45), neither a change in the molecular footprint nor in the density is visible. To confirm the latter, we performed additional LEED measurements after deposition and after two similar annealing steps to 480 K and 520 K, as shown in Figure 45 (b). The LEED patterns after each annealing stage are in agreement with the previously reported (4, 3/ -3, 4) and (3, 4/ 4, -3) superstructures [13] and do not change upon annealing, thus, excluding a surface phase symmetry transition. This preservation of the surface phase symmetry contradicts a base area enlargement that was previously observed for similar molecules that were reported to undergo a complete flattening through ring-closing reactions upon annealing [155].

As both STM and LEED lack an element-specific chemical sensitivity, the results so far cannot directly determine whether the reason for the decreasing STM contrast at the molecular periphery is a structural or a conformational modification of the molecule. To shed light on this, we performed additional XPS measurements, as the element-specificity of this technique allows the evaluation of changes in the chemical environment of a selected atom species.

5.4.2. Modification of the peripheral substituents

As the peripheral substituents mainly consist of carbon atoms, we will first discuss the C 1*s* core-level spectra shown in Figure 46 (a). Upon stepwise annealing up to 470 K, the C 1*s* spectrum undergoes severe line shape changes, whereas the total peak area is conserved. Directly after deposition, the C 1*s* spectrum has a main peak at a binding energy of approximately 285 eV and a pronounced shoulder at around 284 eV. After each annealing step, the intensity of the high BE feature reduces, while the intensity at lower binding energy increases. Notably, the total area below the C 1*s* peak stays constant. In order to interpret the changes in the core-level spectrum, a fit assuming four different contributions was performed. The 44 C atoms in the NiTPP molecule can be divided into four subgroups, each representing a chemical environment. As can be seen in Figure 46 (b), there are 24 phenylic (yellow), 4 *meso*-bridges, 8 C-C-N pyrrolic, and 8 C-C-C pyrrolic carbon atoms. The total spectrum can be reasonably fitted with a multi-peak Voigt function by fixing the area ratio of the four components according to the number of carbon atoms in each chemical environment. The resulting energy alignment of the four components, i.e., the binding energies of 285.1 ± 0.1 eV (phenylic), 284.0 ± 0.1 eV (meso bridge), 285.2 ± 0.1 eV (C-C-N), and 284.6 ± 0.1 eV (C-C-C), agrees with the results for a ZnTPP molecule on Si(111) obtained by Castellarin-Cudia *et al.* [160]. The changes in the line shape can be reproduced by introducing a fifth component at 284.4 ± 0.1 eV. While the binding energies and line

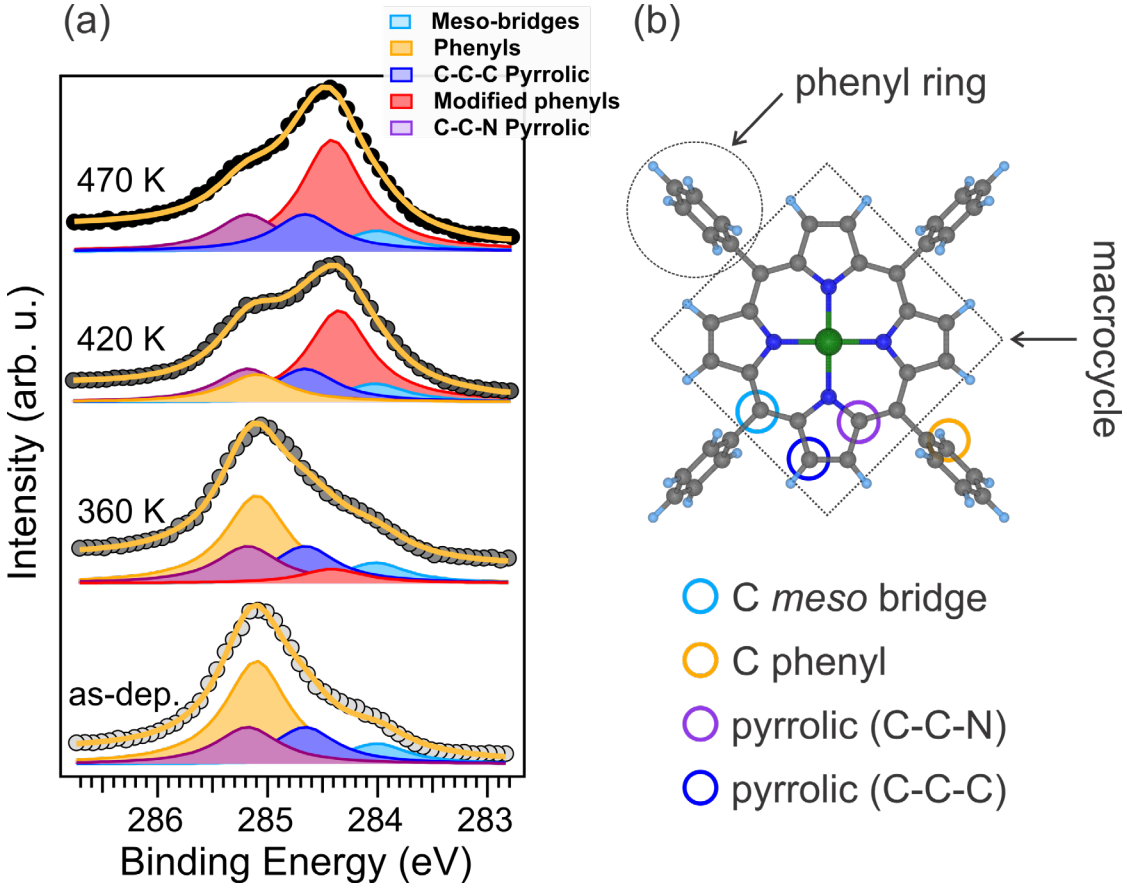

Figure 46) (a) C 1*s* XPS spectra of NiTPP/Cu(100) interface after deposition and after different annealing steps. The spectra were measured in a normal emission geometry with a photon energy of hv = 515 eV. The spectra were fitted with five Voigt profile components representing the four different carbon environments highlighted in (b) and a fifth component representing the carbons located at modified phenyls as described in the main text. Figure adapted from [47].

shapes of the three other components (*meso* bridge, C-C-C, and C-C-N) were kept constant, the data could be reasonably fitted only by reducing the peak area of the unmodified phenyls by the same amount by which the component of the modified phenyl species grows. This suggests that the arising feature in the XPS measurements can be assigned to the fraction of phenyl rings that are subject to the temperature-induced changes seen in the STM images in Figure 45. After annealing to 470 K, the component of the pristine phenyl rings has vanished, and the corresponding area has been transferred to the component representing the modified phenyl rings. The conservation of the total area below the two components suggests that the moieties remain intact and do not undergo (partial) dehydrogenation. The fact that the transformation seems to be completed after annealing to 470 K, while there are still bright phenyls in the STM images after annealing to 530 K, can have two reasons. On the one hand, the STM images and XPS spectra were measured in two different experimental setups having thermocouples in different locations, which generally deviate differently from the temperature directly at the sample surface. On the other hand, the remaining share of the pristine phenyls might still exist but fall below our sensitivity limits.

In addition to the decomposition of the molecule, we can also exclude the formation of C-Cu bonds between phenylic carbons and the surface atoms, as they would give rise to a characteristic XPS component around 283.2 eV, as was reported for other compounds [161]. A repetition of the XPS measurement revealed that the transition of the phenyls from their pristine to their modified state is irreversible on a time scale of around 24 hours.

The difference in binding energy between the components of the pristine and the modified phenyls of approximately 0.7 eV appears to be too large for a purely screening-related effect caused by the decreased phenyl-substrate distance. Alternative options are a charge transfer from the macrocycle to the phenyls and a structural modification affecting the aromatic structure of the whole molecule.

For further insights on the chemical structure, the $k_{\parallel}$ -integrated valence band photoemission intensities, as shown in Figure 47, are discussed next. Starting with the clean copper substrate, a featureless plateau up to the onset of the d bands around a binding energy of around 1.8 eV can be observed, as previously reported [13]. Upon deposition of 1 ML of NiTPP, three molecular fingerprints appear, two of which (around 0.4 and 1 eV) are also visible in the integrated spectrum [13]. A first annealing step up to a temperature of 570 K does not strongly affect the spectrum. A slight intensity enhancement of the VB region, especially of the feature at 0.4 eV, is observed. Beyond 620 K, the VB spectrum starts to change. The two components gradually lose intensity, indicating a stepwise decomposition of the adsorbed molecules. The two features are entirely gone after annealing to 720 K, indicating that the decomposition is complete.

This is also confirmed by the C 1*s* XPS spectra in Figure 47 (b). Up to 620 K (red spectrum), the spectral line shape already measured after annealing to 470 K (see Figure 46) does not undergo further changes. After annealing to 650 K (blue spectrum), the line shape and the

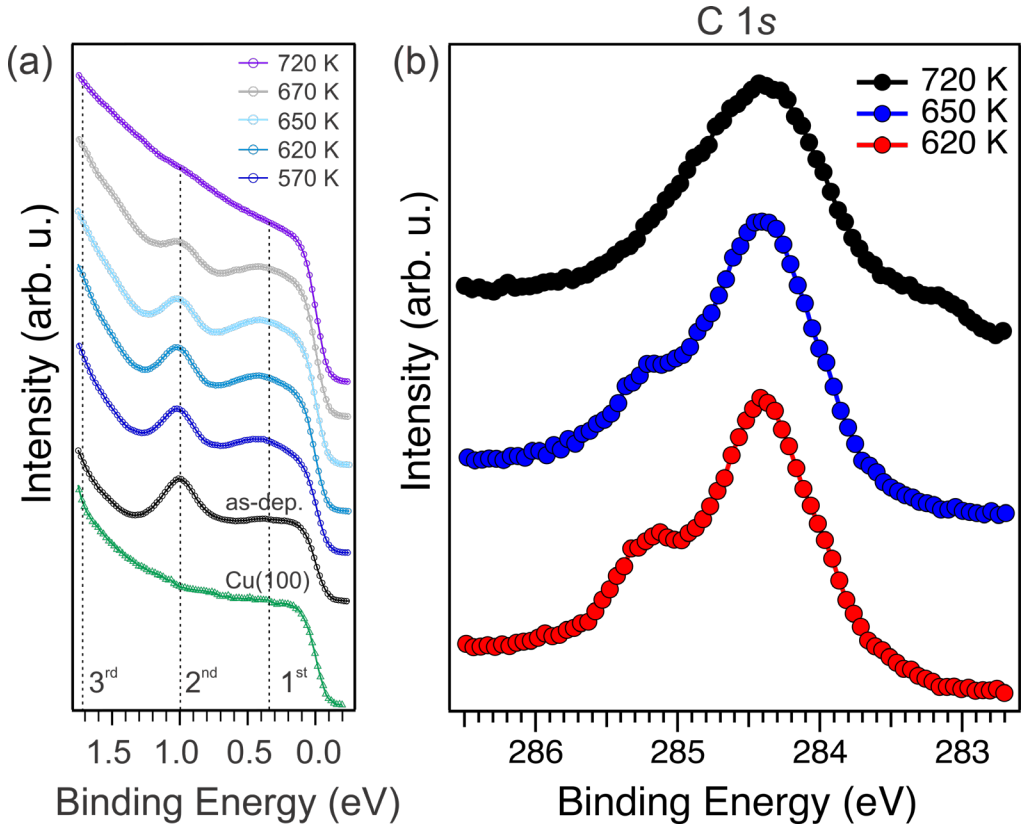

Figure 47) (a) Angle-integrated valence band photoemission spectra of NiTPP/Cu(100) after different annealing steps acquired at a photon energy of 35 eV. (b) C 1*s* XPS spectra at different annealing steps. The spectra were measured in a normal emission geometry and a photon energy of hv = 515 eV. Figure adapted from [47].

total area start to change. Especially the high binding energy shoulder starts to lose intensity. After annealing up to 720 K, the shoulder is much less distinct, and another feature appears at the low binding energy side. Together, this results in one broad C 1*s* feature with contributions of carbon atoms in several different chemical environments, which cannot be identified individually anymore. This is in line with the vanished peaks in the valence band spectrum after annealing to 720 K, as the molecular orbitals do not exist in their pristine form (i.e., as in the as-deposited layer).

Even though the valence band and C 1*s* spectra already provide a first indication of when the decomposition of the molecular layer starts, the question of whether a chemical change of the molecule takes place remains open at this juncture. To answer that, we performed additional PT measurements, which allow us to directly probe the electronic structure of the macrocycle. In the past, PT has already been utilized for the identification of molecular orbitals [13,162–165] or even for the retrieval of wavefunctions by combining it with computational procedures [166,167]. In the experiment presented here, we measured the $k_{\parallel}$-resolved momentum maps at the valence band of the pristine NiTPP film and after several annealing steps to temperatures ranging from 570 to 720 K. Notably, PT has already proven to be a suitable tool for identifying possible intermediate reaction products.

Relevant examples include thermally induced dehydrogenation and subsequent bond formation between carbons atoms of a molecule and copper surface atoms [55], as well as dehydrogenation followed by a ring-closure reaction of cobalt octaethyl porphyrins [56].

To understand whether the changes upon annealing are associated with structural changes, the momentum maps of a frequently reported reaction product for tetraphenyl porphyrins [64,154,155] with a fourfold rotational symmetry were calculated within the framework of DFT. The theoretically calculated momentum patterns of nickel benzotetracyclopenta[*at*, *ef*, *jk*, *op*] porphyrin (hereafter abbreviated as dh-NiTPP), where the phenyl rings are fused with the macrocycle, are calculated and compared to the known [13] NiTPP maps subsequently. Ball-and-stick models of a NiTPP and a dh-NiTPP molecule are shown in Figure 48.

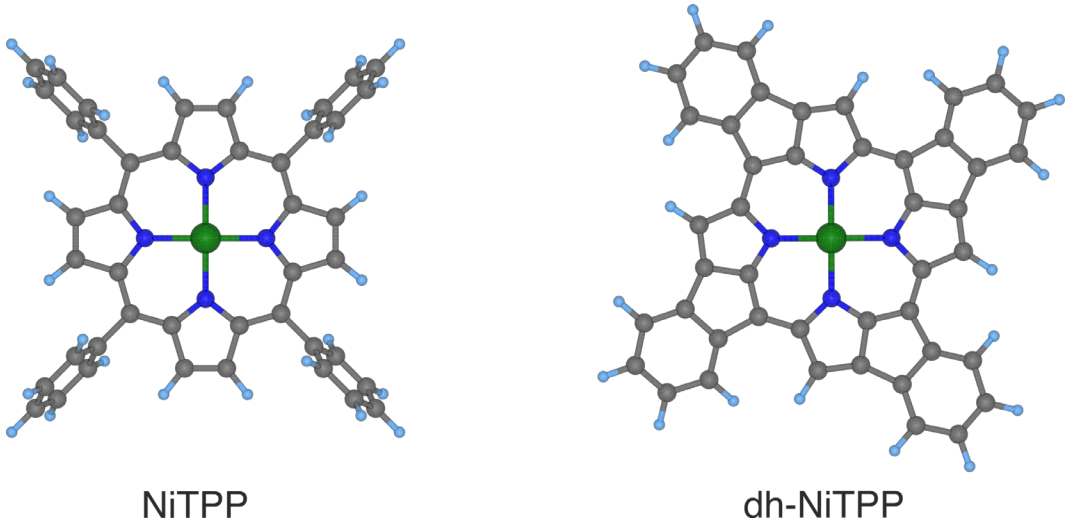

Figure 48) Ball-and-stick models of a NiTPP (left) and a dh-NiTPP molecule (right).

Initial comparison of the simulated momentum maps of the gas-phase molecules in Figure 49 reveals that there are differences expected between the $k_{\parallel}$-resolved valence band intensities for NiTPP and dh-NiTPP. Ball-and-stick models of the molecules left to the maps indicate what can be seen in the corresponding row. In the rows next to panels (a) and (c), the maps of a single NiTPP and dh-NiTPP molecule can be seen, respectively. When deposited onto Cu(100), the molecules self-assemble into two rotational domains. Both the rotational domains and the molecular N-Ni-N axes within these two domains are mirrored by ± 8° with respect to the [100] direction of the copper substrate [13]. As photoemission measurements generally probe a sample area that contains both domains, the signal is averaged over the two azimuthal orientations. To take this into account, the theoretical maps for both molecules are rotated by ± 8°, and the sum of both orientations is calculated so that they can be directly compared to the experimentally obtained maps. For NiTPP, the so-obtained maps are shown in the rows next to panel (b). As dh-NiTPP is additionally chiral, the two chiralities also have to be superimposed for each rotational domain. The row next to panel (d) shows the superposition of both rotational domains, each of which contains molecules in both chiralities.

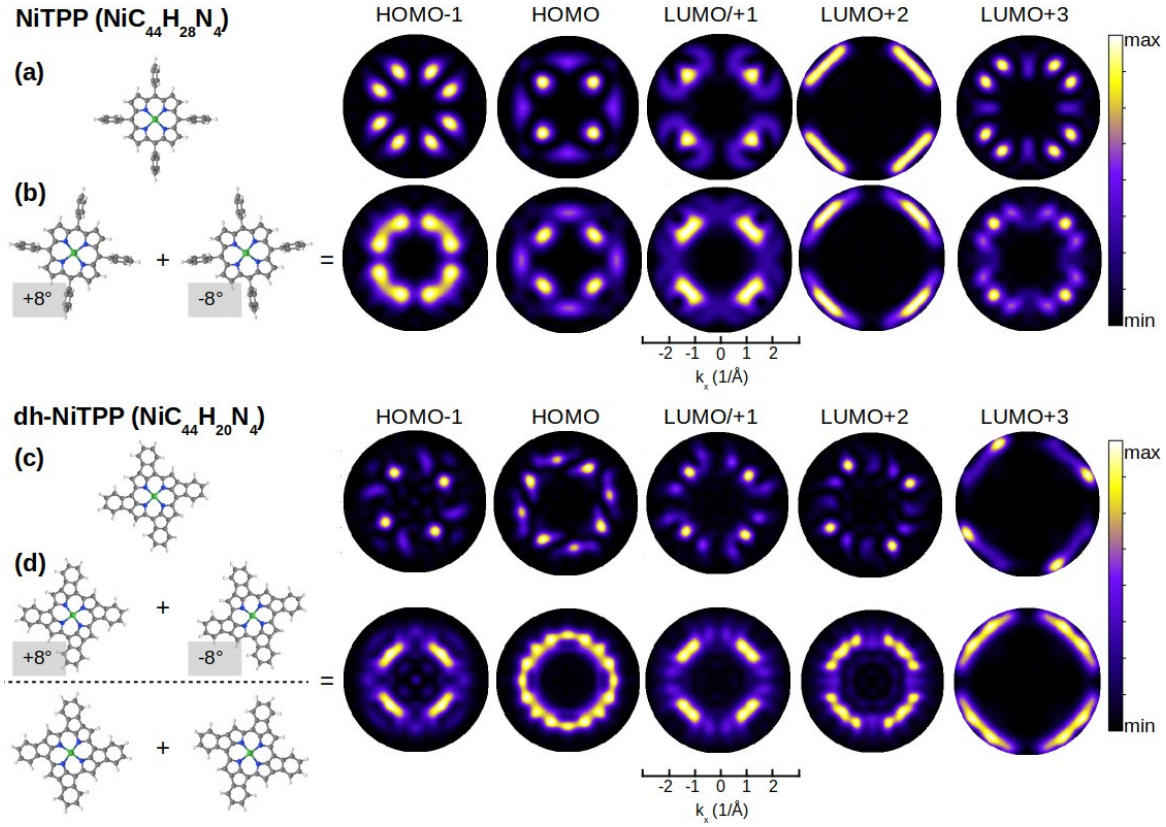

Figure 49) Simulated momentum space patterns of NiTPP and dh-NiTPP. The rows next to the panels (a) and (c) are Fourier transforms of the molecular orbitals of a single molecule. The rows next to the panels (b) and (d) result from a superposition of all experimentally observed azimuthal orientations and, for dh-NiTPP, all possible chiralities. Figure adapted from [47].

Aside from the mismatch in a one-to-one comparison between the molecular orbitals (panels (b) and (d)), there are also pronounced differences in the energy level alignments of the two gas-phase molecules. As shown in Figure 50, the HOMO-LUMO gap is significantly smaller for dh-NiTPP due to a delocalization of the π electrons over the whole molecule. Moreover, unlike the situation in NiTPP, the HOMO and HOMO-1 are not degenerate in dh-NiTPP. It shall be noted that the molecular orbitals, and thus also their energy level alignment, is generally modified upon adsorption on metallic substrates, as observed for NiTPP/Cu(100) [13]. However, there is no apparent reason to assume that the level alignment is more similar for the adsorbed molecules than for the gas-phase molecules.

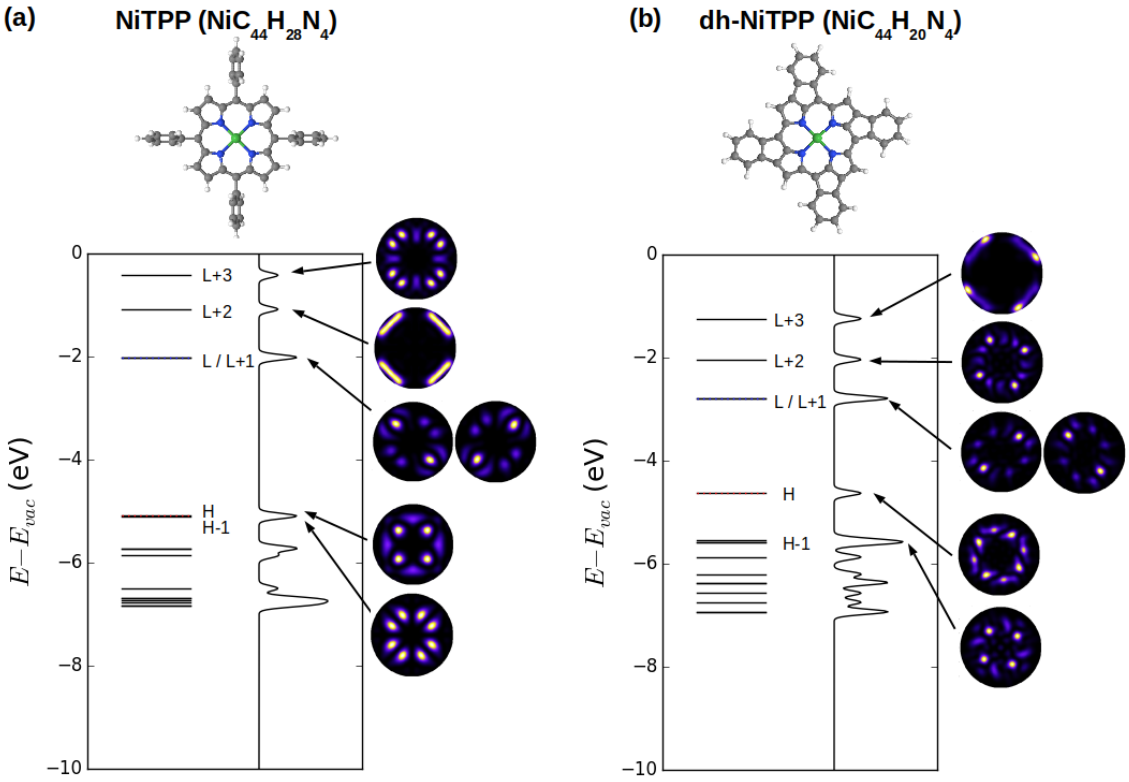

Figure 50) Orbital energies of (a) NiTPP and (b) dh-NiTPP resulting from gas phase DFT calculations. The momentum patterns of the molecular orbitals ranging from the HOMO-1 up to the LUMO+3 are displayed next to the orbital energy diagram. Figure adapted from [47].

Having discussed the differences of the theoretically simulated orbitals, a direct comparison of the experimental momentum maps of NiTPP/Cu(100) before and after annealing to 620 K, i.e., the highest temperature before decomposition is done now. The measured momentum patterns are shown in Figure 51 (a). The exact match between the momentum patterns before and after annealing is a sign that no ring-closing reaction takes place at temperatures up to 620 K. Such chemical modifications would cause essential changes in the symmetry and *k*-space appearance of the molecule and, thus, be detectable in PT.

This is further illustrated in Figure 51 (b) by a direct comparison of the experimentally observed momentum patterns to their simulated counterparts in dh-NiTPP. Even after accounting for the existing chirality and rotational domains, the measured HOMO-1,

LUMO/+1, and LUMO+3 substantially differ from the corresponding molecular orbitals in dh-NiTPP.

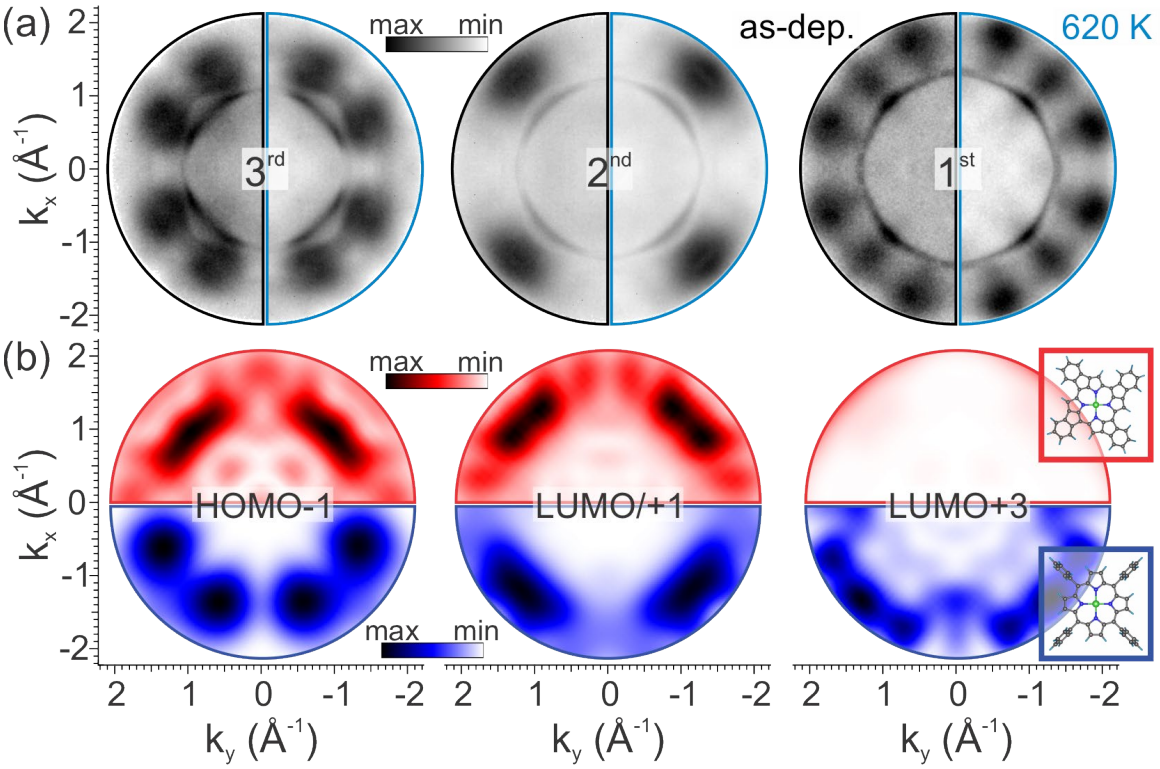

Figure 51) (a) Experimental momentum maps acquired after deposition of NiTPP atop Cu(100) and after annealing up to 620 K. (b) Theoretically computed momentum maps of NiTPP (bottom) and dh-NiTPP (top). Insets on the right side of the maps show ball-and-stick models of the corresponding molecules. Figure adapted from [47].

As the PT results exclude structural changes of the molecule, the question of what ultimately causes the changes in the STM images and XPS spectra upon annealing still remains to be answered. As mentioned previously, NEXAFS is a valuable tool to provide information about the electronic structure and the orientation of molecular orbitals. Therefore, we compare the N and C K-edge spectra before and after annealing in Figure 52.

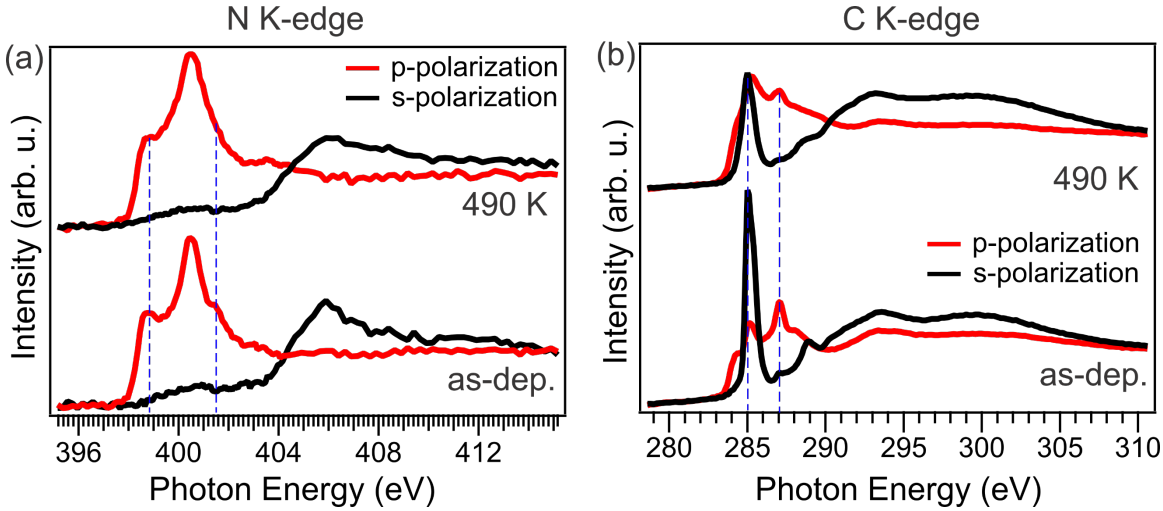

Figure 52) NEXAFS spectra of NiTPP/Cu(100) at the (a) N and (b) C K-edge, respectively, acquired with s- and p-polarized light. The spectra of the as-deposited (annealed) sample are shown in the bottom (top) of the panels. Figure adapted from [47].

Upon annealing, the overall dichroism, i.e., the difference in absorption of s- and p-polarized light, does not change in the N K-edge spectra in Figure 52 (a). However, the intensity of the two π-symmetry resonances at 398.7 and 401.5 eV related to the N 1*s* → LUMO/+1 and LUMO+3 transitions slightly decreases. As already discussed in sections 5.2.2 and 5.2.3, a similar behavior has been observed in the comparison of a monolayer NiTPP in direct contact with copper, where charge transfer takes place, to the multilayer and oxygen-modified system, where the charge transfer is quenched [90]. Therefore, the intensity decrease of the two features can be ascribed to an enhanced charge transfer from the substrate, whereas the similar dichroism indicates that the macrocycle remains flat and parallel to the surface. The enhanced charge transfer is also in line with the intensity increase of the valence band feature at 0.4 eV in Figure 47 (a).

In contrast to the N K-edge spectrum, considerable changes of the dichroism can be observed in the C K-edge spectra upon annealing. The feature at 285.1 eV can be mainly associated with a π^* resonance due to excitation to orbitals located in the phenyl rings [103]. Therefore, the intensity ratio for the two different polarizations can be used to estimate the average angle between the axis of the π^* orbital located at the phenyl rings and the surface normal, as already demonstrated in section 5.2.2. On average, the phenyl rings are rotated by 72° ± 5° out of the plane right after adsorption at room temperature. After completion of the thermal transition, this value decreases to 62° ± 5°. This decrease indicates a flatter conformation of the phenyl rings. However, as mentioned in sections 2.1 and 5.2, two angles (tilt and twist) are required to describe the phenyl conformation unambiguously, and the contributions of these two angles to the flattening of the phenyls cannot be deconvoluted exclusively based on the presented NEXAFS data.

It shall be noted that, aside from a reorientation of the molecular orbitals, the temperature-induced changes in the NEXAFS spectra can also be caused by modifications of the charge transfer. This includes potential changes of the charge transfer from the substrate to the molecule or between different parts of the molecule. A helpful means to get insights into this charge rearrangement is the NEXAFS signal acquired under the so-called magic angle of incidence, which is 54.7° for threefold or higher substrate symmetry [68]. Under this angle, the measured intensity distribution is independent of the molecular orientation and, therefore, mainly determined by changes in the electronic structure [68]. Under the assumption of perfectly linearly polarized light, the absorption intensity acquired under the magic angle can be calculated from a linear combination of the spectra measured in s- and p-polarization, i.e., $I_{\text{magic angle}} = I_p + 2I_s$. Figure 53 shows the C K-edge NEXAFS spectrum under the magic angle of incidence obtained by this relation.

Selected features in the spectra are labeled according to whether they are mainly localized

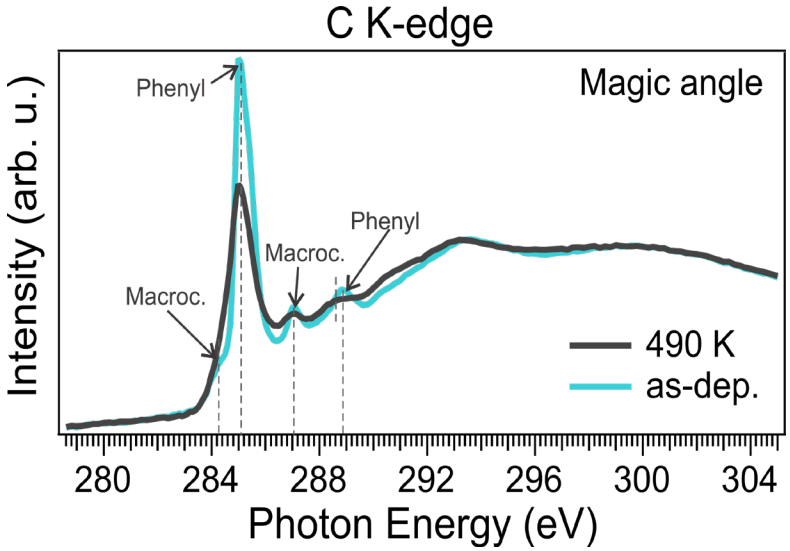

Figure 53) Magic angle C K-edge NEXAFS spectra of NiTPP/Cu(100) before (yellow) and after annealing (black). Selected spectra are labeled according to the molecule moiety they are predominantly localized at. Figure adapted from [47].

at the phenyl rings or the macrocycle. While the features associated with resonances of orbitals at the macrocycle barely change upon annealing, more evident changes can be observed for the phenylic features. Both phenyl-related features experience a substantial intensity reduction upon annealing, suggesting an enhanced charge transfer to the peripheral substituents [111]. This is also supported by the shift in photon energy of the feature around 289 eV. Together with the core-level shift of the phenyl component in the C 1*s* spectrum, this provides evidence that the change of the STM contrast also has an electronic origin.

In addition, the NEXAFS data also exclude the formation of C-Cu bonds, as this would give rise to a characteristic π^* resonance at 288.1 eV, as reported for *para*-phenylene polymerization on copper [161].
Remarkably, the data presented so far consistently point toward conformational instead of structural changes of the molecule. As this behavior might seem contradictory to what has been observed for multiple other porphyrin-metal combinations, we try to contextualize our findings into the literature.

Generally, the energy barrier for a complete flattening is mainly determined by two parameters: the degree of flexibility of the macrocycle and the interaction strength with neighboring molecules. Concerning the flexibility of the macrocycle, the following was observed: the macrocycle is more flexible on rather inert substrates, such as Ag, than on the more reactive Cu surfaces. Accordingly, cyclodehydrogenation was observed for temperatures well beyond 500 K on different Ag surfaces [34,154,158]. It was also observed on Ag substrates that higher temperatures are required for metalated TPP than for free-base TPP molecules, as their macrocycles are more rigid [155,168]. Hence, a higher rigidity leads to enhanced reaction temperatures. Regarding the choice of the substrate, it was reported for the more close-packed Cu(111) surface that the cyclodehydrogenation is completed at temperatures between 570 and 590 K [18]. Generally, the surface reactivity

and, closely related, the charge transfer is higher for the more open Cu(100) surface due to its local undercoordination [26]. Thus, a high charge transfer seemingly stabilizes the molecules against cyclodehydrogenation. With reference to the intermolecular interaction, it was found that for higher coverages, higher temperatures are required to induce cyclodehydrogenation [64]. This can be ascribed to the additional phenyl-phenyl interaction in molecular islands [64].

Assuming that the transformation in NiTPP/Cu(100) behaves kinetically like a first-order reaction, an order of magnitude estimate of the activation barrier can be obtained from a Redhead analysis [169]. From the two components representing pristine and modified phenyls in the C 1*s* spectrum, the share of converted phenyls can be plotted against the temperature, as shown in Figure 54. Since the relationship between the activation energy and the temperature of the maximum reaction rate $T_{max\ rate}$ is constant for a wide range of rate constants and temperatures [169], we can estimate the activation barrier to ± 20 % [170] as $0.25\ kJ / (mol\ K) \cdot T_{max\ rate} = 0.25\ kJ / (mol\ K) \cdot 400\ K \approx 1.04 \pm 0.21\ eV$. In agreement with all the data above that are in contradiction to a chemical modification, this value is significantly smaller than typical barriers reported for a complete flattening, including dehydrogenation [171,172].

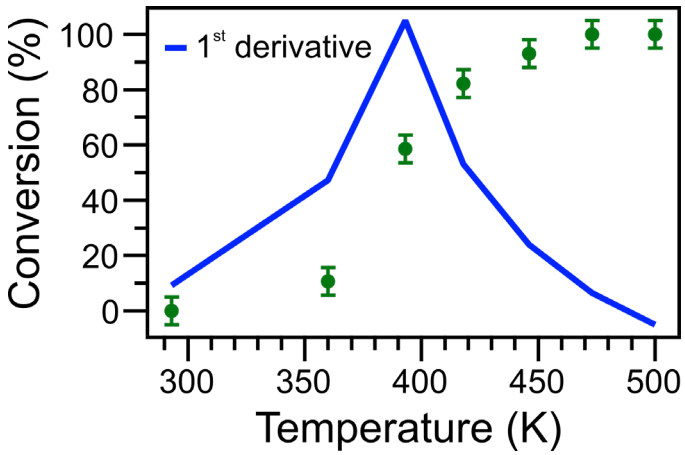

Figure 54) Share of the component of modified phenyls in C 1*s* Figure 46 plotted as a function of the temperature (green markers). The inflection point was determined by calculating the first derivative (blue line). Figure adapted from [47].

An attempt to estimate the energy required for a simple twist of the phenyl substituents can be made using literature data. For this, we consider the intramolecular (phenyl-macrocycle) and intermolecular (phenyl-neighboring phenyl) steric forces. For a phenyl twist from 50 to 70° in isolated CoTPP and ZnTPP molecules with a perfectly flat and rigid macrocycle, similar to the present case, DFT calculations predicted an energy cost of slightly above and slightly below 0.1 eV, respectively [20]. Therefore, we assume that this value is around 0.1 eV for NiTPP. Note that this value is expected to increase when the molecule is adsorbed on a surface, as this causes an additional upward bending (tilting) in the present system [13].

The energy cost due to phenyl-phenyl interaction can be approximated with the value of 0.1 eV for a T-shaped arrangement of two benzene rings, as the phenyls are in a similar

face-to-edge configuration in NiTPP/Cu(100) [13]. Thus, considering that one molecule has four phenyl rings, additional costs of 0.4 eV can be assumed. Hence, a lower limit of 0.5 eV can be estimated for the total energy barrier of twisting the phenyls in a free-standing layer. The difference to our value of 1.04 ± 0.21 eV from the Redhead analysis above likely originates from the neglect of the surface and, in particular for the present system, the related charge transfer.

5.4.3. Nickel oxidation state

Since in section 5.3 the Ni(I) oxidation state was shown to be an essential prerequisite for the reactivity of the molecule, the effects of the annealing on the central nickel ion needs to be examined. For this, we first discuss the Ni $2p_{3/2}$ core-level spectrum in Figure 55.

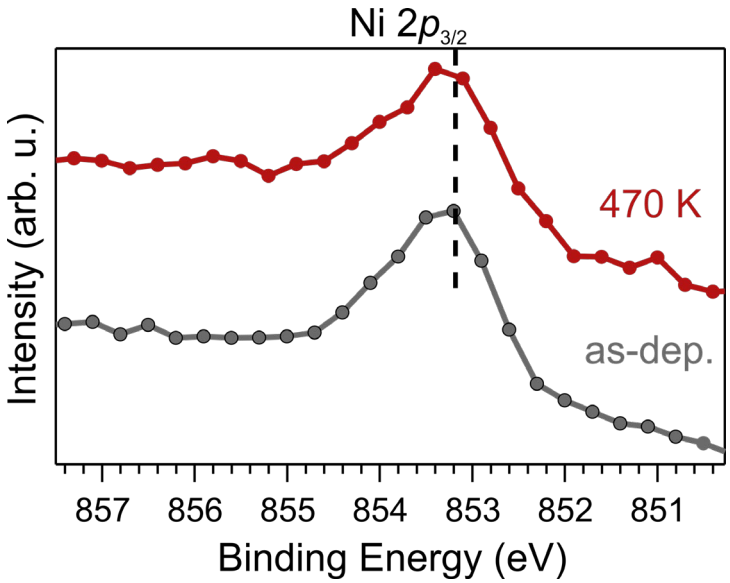

Figure 55) XPS spectra of the Ni $2p_{3/2}$ core level of NiTPP/Cu(100) before and after annealing to 470 K. The spectra were measured in a normal emission geometry with a photon energy of hν = 1020 eV. Figure adapted from [47].

The binding energy of 853.15 eV is a fingerprint of the Ni(I) oxidation state [14]. Even though the oxidation state cannot be determined solely from the core-level spectrum, the match of the binding energies and line shapes before and after annealing is a first indication for the preservation of the substrate-induced Ni(I) state. The Ni L_3-absorption spectra in Figure 56 further support this.

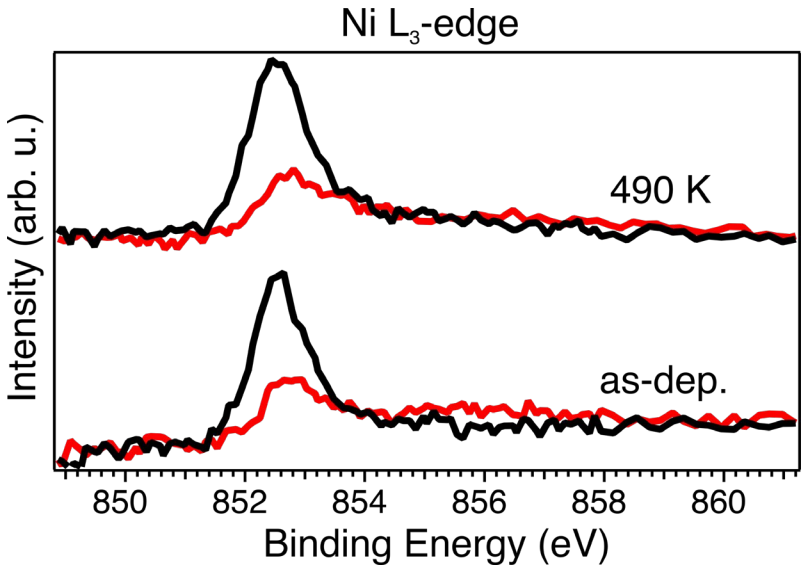

Figure 56) NEXAFS spectra at the Ni L_3-absorption edge for NiTPP/Cu(100) before and after annealing up to 490 K, measured with s- and p-polarized light. Figure adapted from [47].

In agreement with the XPS measurements, the spectra before and after annealing have a similar line shape. As mentioned in the previous section, the single-peak structure of the σ^*-type main feature at 852.4 eV is characteristic of the Ni(I) oxidation state [14]. Furthermore, the agreement of line shape and energy position before and after annealing excludes the replacement of the central Ni atom by a Cu surface atom. In particular, the conservation of the dichroism unequivocally rules out such a replacement of the central ion. This process, also referred to as transmetalation, was previously observed at increased temperatures [173,174]. The effect of the annealing on the direct environment of the nickel atom can be examined from the N 1*s* core-level spectrum after different annealing steps, as shown in Figure 57.

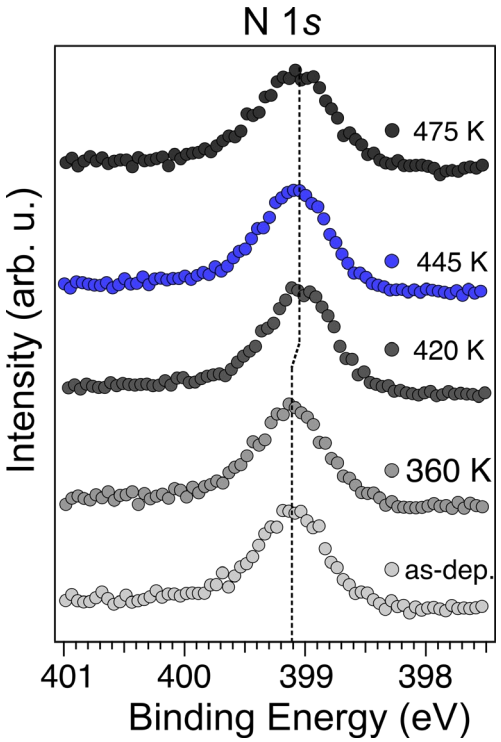

Figure 57) N 1*s* XPS spectra of NiTPP/Cu(100) after deposition and after different annealing steps. The spectra were measured in a normal emission geometry with a photon energy of hν = 515 eV. Figure adapted from [47].

After every annealing step, the N 1*s* spectrum shows a single component. This is expected for metalated porphyrin molecules, in which the four N atoms are in chemically equivalent environments. Thus, the concentration of impurities, e.g., by non-metalated free-base porphyrins (2HTPP), is below our experimental sensitivity. After annealing up to 420 K, a small peak shift by less than 0.1 eV toward lower binding energy can be observed, whereas the overall line shape remains unchanged. Such a small core-level shift suggests that the chemical surrounding of the nitrogen atoms after annealing is similar to the one in the as-deposited NiTPP layer. Possible explanations include an increase in the charge transfer from the substrate and a

decrease in the distance between the N atoms and the surface. The former is also in line with the quenching of the N 1*s* → LUMO/+1 and LUMO+3 transitions in the N K-edge NEXAFS spectrum presented above. However, it shall be noted that cyclodehydrogenation cannot be excluded merely from these XPS results since it typically does not manifest in the N 1*s* core-level spectra [94,157,158].

5.4.4. Conclusions

In summary, the consistency of the presented data allows a number of conclusions about the behavior of the strong metal-molecule interaction at the NiTPP/Cu(100) interface upon annealing. STM reveals a gradual, irreversible transformation upon annealing to temperatures starting from 420 K. A surface phase change, however, can be excluded from both STM and LEED. Crucially, the highly reactive Ni(I) oxidation state is preserved throughout the whole temperature-induced transition up to the limit of thermal decomposition at 620 K. According to PT, even the peripheral substituents do not undergo chemical modifications, resulting in a conservation of the overall electronic structure of the molecules.

Since this is clearly in contrast to previous experiments on similar pairs of porphyrins and metal substrates, we tried to answer what ultimately prevents the cyclodehydrogenation. After estimating the energy and analyzing the driving mechanisms in comparable systems, the presented data consistently point towards the surface-pinning as the ultimate reason for the stability against thermally induced chemical changes. By preventing any lateral displacement of the NiTPP molecules, the pinning ensures the conservation of the catalytically valuable Ni(I) oxidation state up to the point of molecular decomposition. Thus, the Ni(I)TPP/Cu(100) interface offers perspectives for thermally resistant catalysts, sensors, or spintronic building blocks, where annealing cycles up to 620 K can be used to restore the reactivity of the molecular layer.

6. Conclusions

Starting from NiTPP deposited onto the Cu(100) surface as a model system, two strategies to tune and manipulate the chemical and physical properties of this system were investigated in this thesis. The first approach aimed at quenching the charge transfer by means of a pre-oxidization of the copper surface. In the second approach, a reversible spin-switching transition of the central nickel atom was induced at room temperature.

The molecular self-assembly on the oxygen pre-exposed copper (O-Cu(100)) surface was characterized by LEED and STM. By means of PT and NEXAFS, we found that the charge transfer was indeed quenched: in contrast to the plain NiTPP/Cu(100) interface, the features associated with the LUMO/+1 and LUMO+3 cannot be observed via PT, and the LUMO+2, which is accessible via NEXAFS is also at the expected position. Moreover, a clear dichroic x-ray absorption signal reveals a preferential orientation of the molecule. As a definite advantage to a multilayer spectrum, where the molecules are randomly ordered, this enables the identification of molecular orbital symmetries. Due to the preservation of the gas-phase-like Ni(II) oxidation state, the Ni(II)TPP/O-Cu(100) interface can be considered as a reference system with molecules that are weakly perturbed by the surface but still grow in an ordered fashion.

With the help of this reference system, we found that the Ni(I) oxidation state is a prerequisite for the extremely high reactivity of the Ni(I)TPP/Cu(100) interface to NO_2, as we did not detect any sign of adsorption on the Ni(II)TPP/O-Cu(100) interface. The Ni(I) atom in the reduced Ni(I)TPP, instead, binds the NO_2 molecule even in the buried interface.

Regarding the adsorption geometry, both IRAS and NEXAFS revealed a "V" shaped configuration of the NO_2 molecule that was supported by theoretical calculations.

For the Ni(I)TPP/Cu(100) surface, x-ray absorption measurements suggest that the NO_2 adsorption induces a transition from a $3d^9$ to a $3d^8$ configuration with two unpaired electrons. The three different $3d$ shell configurations (d^9 for Ni(I)TPP/Cu(100), LS d^8 for Ni(II)TPP/O-Cu(100), and HS d^8 for NO_2-Ni(II)TPP/Cu(100)) were confirmed by the corresponding projected densities of states obtained by DFT. Instead, the electronic structure of the macrocycle remains almost unaffected by the NO_2 adsorption. Hence, the Ni(I)TPP/Cu(100) system can be viewed as two mostly independent systems. While the central Ni atom mainly carries the spin moment and therefore the magnetic properties, the macrocycle contains the frontier orbitals which determine the optical and transport properties.

An annealing cycle up to 390 K is sufficient to remove the adsorbed NO_2 molecules and to restore the pristine Ni(I). After that, a flatter conformation and an increased substrate interaction of the peripheral phenyl rings could be observed. Nevertheless, the molecule was found to be stable against chemical modifications up to the limit of thermal decomposition (620 K), as shown by PT and NEXAFS. Additionally, evidence is found for an overall increase in the charge transfer from the substrate to the molecule and an intramolecular electron rearrangement from the macrocycle towards the phenyl substituents upon annealing. After an estimate of the energy costs at play, the presented data consistently point towards a pinning of the molecules due to the strong molecule-substrate interaction

as the underlying reason for the high thermal stability. This paves the way for thermally highly resistant building blocks in the fields of heterogeneous catalysis or gas sensing.

This work has improved the understanding of the implications of the charge transfer at the Ni(I)TPP/Cu(100) interface and suggests mechanisms to selectively tune the electronic and magnetic properties of this system to meet application-specific requirements. Moreover, technologically relevant insights regarding the thermal stability and the behavior of the buried interface have been gained. This can help to bridge the gap between fundamental research on metal-organic interfaces under precisely controlled laboratory conditions and their use in more applicative environments.

7. Outlook

The results discussed in this thesis suggest significant differences between the strongly hybridizing NiTPP/Cu(100) and the weakly coupled NiTPP/O-Cu(100) interface concerning the reactivity and the magnetic properties of the molecule. Therefore, the insights gathered about these systems can build a base to address fundamental problems like the charge injection and relaxation dynamics at these model interfaces. Time-resolved photoemission spectroscopy has proven to be a suitable means to investigate such characteristics [175,176]. Recent experiments have shown that combining high harmonics generation (HHG) and momentum microscopy paves the way for an extension of this technique to the space domain by capturing the full momentum-space distribution of unoccupied molecular orbitals [114]. While HHG provides probe photon energies that allow photoemission of electrons with high parallel momenta, momentum microscopy enables their detection. In combination with the electronic decoupling by the oxygen interlayer, the NiTPP/O-Cu(100) interface presented in this thesis is an exciting candidate for time-resolved orbital tomography. On the bare copper substrate, strong hybridization with the NiTPP molecules might lead to decay times of excited electronic states beyond the fs regime, making this process inaccessible with current state-of-the-art laser systems. Nevertheless, a comparison of NiTPP/Cu(100) before and after the functionalization with NO_2 might induce more localized states which generally have longer lifetimes [7]. Aside from the emergence of electronic states localized at the NO_2 molecule itself, a decoupling of the NiTPP molecule from the metal substrate due to the surface-*trans* effect could open pathways for investigating the relaxation mechanisms at metal-organic interfaces.

Moreover, the fact that NO_2 also binds to the buried monolayer might offer the possibility for optical measurements in (near-) ambient pressure conditions to further explore the applicative potential of this interface. The results in this thesis demonstrate that the electronic structure of the NiTPP macrocycle is barely changed by the functionalization of NiTPP with NO_2 molecules. As the energy level alignment of the frontier orbitals ultimately determines the optical properties of the molecule, the absence of any changes suggests that the optical properties remain vastly unaffected by the on-top ligation. All-optical measurements provide a means to prove that directly. The high bulk sensitivity of such techniques (compared to photoemission experiments) might allow for the direct examination of the effects of the NO_2 adsorption on the ultrafast dynamics at the metal-organic interface. As the chelated metal ion in tetra-coordinate ligand complexes has been shown to have an impact on the optical properties of the molecule at wavelengths ranging from 200 to 1000 nm [177,178], the effect of selectively changed spin and oxidation state of the central nickel ion can be investigated with the white-light supercontinuum spectrometer that is currently set up in our lab. Such experiments might help to deepen the understanding of the optoelectronic properties of this multifunctional interface.

A. Appendix

A.1. Sum rule normalization

As mentioned in section 4.2.2, for calculating the effective spin and orbital magnetic moments, system-specific assumptions on the isotropic absorption intensity I_{iso} have to be made. In general, this isotropic absorption intensity can be written as the sum of the absorption intensities of three light waves, each having a linear polarization aligned along one of the three main symmetry directions in a cubic crystal

$$\mathrm{I_{iso}} = \int_{\mathrm{L_3+L_2}} \mathrm{I_x} + \mathrm{I_y} + \mathrm{I_z}. \tag{28}$$

Moreover, it is reasonable to assume that $I_x = I_y = I_z$ in cubic systems. Therefore, it is sufficient to know the absorption due to light that is linearly polarized along one of these main symmetry axes and to multiply that by three. An equivalent approximation is often made for the absorption of circularly polarized light in normal incidence ($\Theta = 0°$). As the electric field vectors of left- and right-hand circularly polarized light rotate in a plane parallel to the sample plane, it can be written that

$$I_x + I_y = I_+^{0°} + I_-^{0°} = \frac{2}{3} I_{\mathrm{iso}}. \tag{29}$$

However, this approximation is not appropriate for systems like an adsorbed metal that is laterally caged in an organic ligand, as they have a significantly different symmetry in the z-direction than in the x- and y-direction. The aim of this appendix is to derive an expression for I_{iso} for an arbitrary angle of incidence Θ that depends on the absorption intensities of circularly polarized light. In this way, we can evaluate the sum rules for the effective spin moment and the orbital moment with only two absorption measurements with different helicities.

The geometry of such an absorption experiment with linearly polarized light is depicted in Figure 58. A light beam is incident onto the sample plane lying in the x-y-plane of the laboratory frame of reference under an angle of incidence Θ. Generally, the polarization can be written as the sum of a linear horizontal (LH) and a linear vertical component (LV).

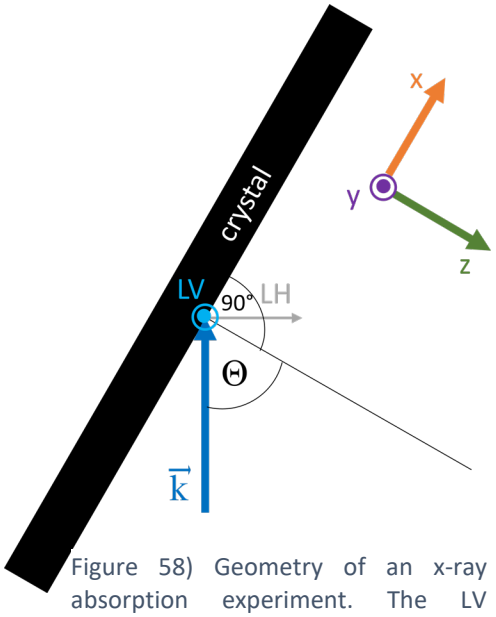

Figure 58) Geometry of an x-ray absorption experiment. The LV component of the light points into y-direction, i.e., into the image plane.

To find an expression for the intensities of circularly polarized light, we need to relate the absorption intensity of linearly polarized light to the absorption intensity of circularly polarized light. As the same plane is probed, the sum of the absorption intensities of LV and LH polarized light equals the sum of right- and left-circularly polarized light for an arbitrary angle Θ

$$I_{\mathrm{XAS}}^{\Theta} = I_{+}^{\Theta} + I_{-}^{\Theta} = I_{\mathrm{LH}}^{\Theta} + I_{\mathrm{LV}}. \tag{30}$$

Independent of the angle of incidence Θ, the absorption of the LV component equals the absorption for light polarized along the y-direction and, due to the cubic symmetry, along the x-direction. The absorption due to the LH component can be derived from geometrical considerations:

$$\begin{aligned} I_{\mathrm{LV}} &= I_x = I_y =: I_{xy}, \text{ and} \\ I_{\mathrm{LH}}^{\Theta} &= I_z \, sin^2(\Theta) + I_{xy} \, cos^2(\Theta). \end{aligned} \tag{31}$$

Replacing I_{LH}^{Θ} and I_{LV} in (30) with the expressions in (31), we find

$$I_{\mathrm{XAS}}^{\Theta} = I_z \, sin^2(\Theta) + I_{xy}(1 + cos^2(\Theta)), \tag{32}$$

and, therefore, for normal incidence

$$I_{\mathrm{XAS}}^{0^\circ} = 2I_{xy}. \tag{33}$$

Moreover, we can rewrite (32) to find an expression for I_z

$$I_z = \frac{I_{\mathrm{XAS}}^{\Theta} - (cos^2(\Theta) + 1)I_{xy}}{sin^2(\Theta)} = \frac{I_{\mathrm{XAS}}^{\Theta} - (cos^2(\Theta) + 1)\dfrac{I_{\mathrm{XAS}}^{0^\circ}}{2}}{sin^2(\Theta)}, \tag{34}$$

where equation (33) was exploited in the last step. To evaluate the expression (28), an expression for $I_x + I_y$ in dependence of the grazing XAS intensity $I_{\mathrm{XAS}}^{\Theta}$ is necessary. By normalizing $I_{\mathrm{XAS}}^{\Theta}$ by the intensity at normal incidence $I_{\mathrm{XAS}}^{0^\circ}$, we get

$$\frac{I_{\mathrm{XAS}}^{\Theta}}{I_{\mathrm{XAS}}^{0^\circ}} = \underbrace{\frac{I_z \sin^2(\Theta)}{2I_{xy}}}_{g(\Theta)} + \underbrace{\frac{\cos^2(\Theta) + 1}{2}}_{f(\Theta)}. \tag{35}$$

The term $g(\Theta)$ only differs from zero if there is an unoccupied orbital with a component in the z-direction, as otherwise there is no absorption due to the light component aligned in the z-direction. If this is not the case, we can express $I_x + I_y$ with the help of equation (34) as

$$I_x + I_y = 2I_{xy} = \frac{I_{\mathrm{XAS}}^{\Theta}}{\frac{1}{2}(cos^2(\Theta) + 1)} \tag{36}$$

As an example, the copper atom in CuPc/Ag(100) is in a $3d^9$ configuration with an empty $d_{x^2-y^2}$ orbital mainly lying in the x-y-plane [179]. Stepanow *et al.* found an excellent agreement for the effective spin moment and the orbital moment with theoretical calculations by neglecting $f(\Theta)$ in the normalization of the sum rules [140]. As previous DFT calculations revealed that for Ni(I)TPP/Cu(100), the only unoccupied orbital has a strong $d_{x^2-y^2}$ character, we can reasonably assume that $I_z = 0$. Notably, this was also assumed for the NO_2-Ni(II)TPP/Cu(100) interface, even though there are empty orbitals with $d_{x^2-y^2}$ and d_{z^2} character. This might lead to deviations of the effective spin and orbital moments for NO_2-Ni(II)TPP/Cu(100) at grazing incidence.

In summary, for a correct normalization, we have to distinguish between two systems in two geometries, i.e., Ni(I)TPP/Cu(100) and NO_2-Ni(II)TPP/Cu(100), each in a grazing and normal incidence geometry:

Ni(I)TPP/Cu(100):

- Normal incidence:
  As the light polarization has no component in the z-direction, we assume
  $$I_{\text{iso}} = I_x + I_y = I_+^{0^\circ} + I_-^{0^\circ} \tag{37}$$

- Grazing incidence
  As the d_{z^2} orbital is fully occupied, our case is equivalent to CuPc/Ag(100), and it can be assumed that $I_z = 0$ [78]. Exploiting equation (36), we get
  $$I_{\text{iso}} = I_x + I_y = \frac{I_+^\Theta + I_-^\Theta}{\frac{1}{2}(cos^2(\Theta) + 1)} \tag{38}$$

NO_2-Ni(II)TPP/Cu(100):

- Normal incidence:
  As the light polarization has no component in the z-direction, we assume
  $$I_{\text{iso}} = I_x + I_y = I_+^{0^\circ} + I_-^{0^\circ}. \tag{39}$$

- Grazing incidence
  Here, the adsorption due to the z-component of the light polarization is not necessarily negligible, since the DFT calculations from section 5.2 suggest that there are two unoccupied orbitals available for the excitation, i.e., the $3d_{x^2-y^2}$ and also the $3d_{z^2}$ orbital, which is aligned in the z-direction. Hence, we can use the expression in equation (34) to evaluate I_z. However, we cannot further evaluate $g(\Theta)$ and, thus, cannot entirely account for the absorption intensity $I_x + I_y$. We have to make the simplifying assumption that
  $$\begin{aligned} I_{\text{iso}} &= I_x + I_y + I_z \\ &= \frac{I_+^\Theta + I_-^\Theta}{\frac{1}{2}(cos^2(\Theta) + 1)} + \frac{I_+^\Theta + I_-^\Theta - (cos^2(\Theta) + 1)\frac{I_+^{0^\circ} + I_-^{0^\circ}}{2}}{sin^2(\Theta)}. \end{aligned} \tag{40}$$

  This can result in an overestimation of the effective spin moment and orbital moment from the sum rules.

A.2. Magnetic dipole term

As described in section 4.2.2, the effective spin moment $m_{s,\mathrm{eff}}$ deviates from the isotropic spin moment m_s by the magnetic dipole term $7\langle T_\Theta\rangle$. $\langle T_\Theta\rangle$ is the expectation value of the magnetic dipole operator T in the direction Θ and generally arises from an anisotropic spin density in the atomic volume. In a one-electron model, it can be written as

$$T = \hat{S} - 3\hat{r}(\hat{r}\cdot S), \tag{41}$$

where $\hat{S}$ is the magnetization unit vector of the spin moment S and $\hat{r}$ is the position unit vector. Its component along α can be expressed by the charge quadrupole tensor and the spin components as

$$T_\alpha = \sum_\beta Q_{\alpha\beta} S_\beta, \tag{42}$$

which shows that the charge and spin components of T are generally coupled. For an atomic spin-orbit coupling which is comparable to the crystal field splitting, this means that it is not possible to determine the isotropic spin moment from the XMCD measurements directly, as $\langle T_\alpha\rangle$ gives an additional contribution to $m_{s,\mathrm{eff}}$. However, if the spin-orbit coupling is weak compared to the crystal field and the exchange splitting, it can be treated by perturbation theory. For symmetries higher than D_{2h}, this leads to the approximate result

$$\langle T_\alpha\rangle \approx \sum_i Q_\alpha^i s^i, \tag{43}$$

where $Q_\alpha^i = \langle d_i|Q_{\alpha\alpha}|d_i\rangle$ is the quadrupole matrix element of the orbital d_i, and s^i is the spin component projected onto this orbital, with $\langle S\rangle = \sum_i s^i$ [180]. This approximation is exact without spin-orbit interaction, i.e., with a coupling constant $\xi = 0$. With spin-orbit interaction ($\xi > 0$), the correction term depends on the orientation of the spins. If all spins are aligned in the same direction, it is in the order of $(\xi/\Delta_{CF})^2 \approx 0.01$, whereas if the spins are aligned in different orientations, it is $\left(\xi/(\Delta_{CF}+\Delta_{ex})\right) < 0.1$ [180]. Moreover, in this approximation, the isotropic spin moment m_s can be obtained in three ways, i.e.,

- measuring the absorption along the x, y, and z axes,
- measuring the absorption of polycrystalline samples, or
- performing a measurement at the magic angle.

The first two ways exploit the fact that the angular average of $\langle T_\alpha\rangle$ vanishes as $\sum_\alpha\langle T_\alpha\rangle \approx \sum_i s^i \sum_\alpha Q_\alpha^i = 0$ [180]. The third aspect is valid for a higher than twofold symmetry about the z-axis and an angle of incidence Θ. In this case, the quadrupole matrix element can be written as $Q_{\alpha=\Theta} = \left(\langle Q_{xx}\rangle + \langle Q_{yy}\rangle \frac{1}{2} sin(\Theta)^2 + \langle Q_{zz}\rangle cos(\Theta)^2\right)$ and, thus, vanishes for $\Theta = 54.7°$.

For $3d$ metals, the conditions for the approximation above are fulfilled, as they have a low spin-orbit coupling with respect to their crystal field splitting. The role of $\langle T_\alpha\rangle$ is much debated. However, it can be said that for low-dimensional systems, its contribution is generally expected to be higher as the charge density anisotropy is higher [181–183]. Wu and Freeman predicted an increase in the out-of-plane correction $7\langle T_z\rangle$ when going from a monolayer to a bulk-like center layer of approximately 200 %, 1600 %, and 700 % for Ni, Co, and Fe [181]. However, for four-coordinated metal ions caged in a molecular ligand

supported by a metal surface, comparable to the situation of the nickel center in NiTPP/Cu(100), smaller anisotropies were reported. Stepanow *et al.* found an excellent agreement for a model based on a tetragonal pyramidal crystal field (C_{4v}) and experimentally obtained $m_{s,\mathrm{eff}}$ values CuPc/Ag(100) [78]. Thereby, they could disentangle m_s and $7\langle T_\alpha \rangle$, yielding an almost isotropic $m_s \approx 0.5\mu_B$ and a $7\langle T_\alpha \rangle$ that strongly varied with the angle of incidence, ranging from 1.1 μ_B at normal incidence to -0.5 μ_B at 90°.

List of abbreviations

2HTPP	Free-base porphyrin
ATR	Attenuated total reflectance
CoOEP	Cobalt octaethyl porphyrin
CuPc	Copper phthalocyanine
DFT	Density functional theory
DOS	Density of states
ESCA	Electron spectroscopy for chemical analysis
FM	Ferromagnetic
FT-IR	Fourier transform infrared
G. I.	Grazing incidence
HHG	High harmonics generation
HOMO	highest occupied molecular orbital
HREELS	High-resolution electron energy loss spectroscopy
HS	High-spin
IRAS	Infrared reflection absorption spectroscopy
L	Piperidine
LDOS	Local density of states
LEED	Low-energy electron diffraction
LH	Linear horizontal
LS	Low-spin
LUMO	Lowest unoccupied molecular orbital
LV	Linear vertical
MO	Molecular orbital
MSSR	Metal surface selection rule
MTPP	Metal tetraphenyl porphyrin
N. I.	Normal incidence
NEXAFS	Near-edge x-ray absorption fine structure spectroscopy
NiTPP	Nickel tetraphenyl porphyrin
PDOS	Projected density of states
PEEM	Photoelectron emission microscope
PT	Photoemission tomography
PTCDA	Perylene-tetracarboxylic dianhydride
STM	Scanning tunneling microscopy
TEY	Total electron yield
UHV	Ultra-high vacuum
UPS	Ultraviolett photoemission spectroscopy
XMCD	X-ray magnetic circular dichroism

Bibliography

[1] Nobel Foundation. "The nobel prize in physics 2007". NobelPrize.org. Published 2007. Accessed on: November 2, 2021. https://web.archive.org/web/20110805062614/http://nobelprize.org/nobel_prizes/physics/laureates/2007/index.html

[2] I. Žutić, J. Fabian, and S. Das Sarma. "Spintronics: fundamentals and applications". *Reviews of Modern Physics* **76** (2), (2004), pp. 323-410.

DOI: 10.1103/RevModPhys.76.323

[3] J. Devkota, R. Geng, R.C. Subedi, and T.D. Nguyen. "Organic spin valves: a review". *Advanced Functional Materials* **26** (22), (2016), pp. 3881-3898.

DOI: 10.1002/adfm.201504209

[4] X. Sun, A. Bedoya-Pinto, Z. Mao, M. Gobbi, W. Yan, Y. Guo, A. Atxabal, R. Llopis, G. Yu, Y. Liu, A. Chuvilin, F. Casanova, and L.E. Hueso. "Active morphology control for concomitant long distance spin transport and photoresponse in a single organic device". *Advanced Materials* **28** (13), (2016), pp. 2609-2615.

DOI: 10.1002/adma.201503831

[5] G.R. Whittell and I. Manners. "Metallopolymers: new multifunctional materials". *Advanced Materials* **19** (21), (2007), pp. 3439-3468.

DOI: 10.1002/adma.200702876

[6] L. Guo, X. Gu, X. Zhu, and X. Sun. "Recent advances in molecular spintronics: multifunctional spintronic devices". *Advanced Materials* **31** (45), (2019), pp. 1805355.

DOI: 10.1002/adma.201805355

[7] M. Cinchetti, V.A. Dediu, and L.E. Hueso. "Activating the molecular spinterface". *Nature Materials* **16** (5), (2017), pp. 507-515.

DOI: 10.1038/nmat4902

[8] F. Al Ma'Mari, T. Moorsom, G. Teobaldi, W. Deacon, T. Prokscha, H. Luetkens, S. Lee, G.E. Sterbinsky, D.A. Arena, D.A. MacLaren, M. Flokstra, M. Ali, M.C. Wheeler, G. Burnell, B.J. Hickey, and O. Cespedes. "Beating the Stoner criterion using molecular interfaces". *Nature* **524** (7563), (2015), pp. 69-73.

DOI: 10.1038/nature14621

[9] N. Ballav, C. Wäckerlin, D. Siewert, P.M. Oppeneer, and T.A. Jung. "Emergence of on-surface magnetochemistry". *Journal of Physical Chemistry Letters* **4** (14), (2013), pp. 2303-2311.

DOI: 10.1021/jz400984k

[10] C. Wäckerlin, K. Tarafder, J. Girovsky, J. Nowakowski, T. Hählen, A. Shchyrba, D. Siewert, A. Kleibert, F. Nolting, P.M. Oppeneer, T.A. Jung, and N. Ballav. "Ammonia coordination introducing a magnetic moment in an on-surface low-spin porphyrin". *Angewandte Chemie International Edition* **52** (17), (2013), pp. 4568-4571.

DOI: 10.1002/anie.201208028

[11] I. Cojocariu, S. Carlotto, H.M. Sturmeit, G. Zamborlini, M. Cinchetti, A. Cossaro, A. Verdini, L. Floreano, M. Jugovac, P. Puschnig, C. Piamonteze, M. Casarin, V. Feyer, and C.M. Schneider. "Ferrous to ferric transition in Fe-phthalocyanine driven by NO_2 exposure". *Chemistry – A European Journal* **27** (10), (2021), pp. 3526-3535.

DOI: 10.1002/chem.202004932

[12] C. Wäckerlin, D. Chylarecka, A. Kleibert, K. Müller, C. Iacovita, F. Nolting, T.A. Jung, and N. Ballav. "Controlling spins in adsorbed molecules by a chemical switch". *Nature Communications* **1** (5), (2010), pp. 1-7.

DOI: 10.1038/ncomms1057

[13] G. Zamborlini, D. Lüftner, Z. Feng, B. Kollmann, P. Puschnig, C. Dri, M. Panighel, G. Di Santo, A. Goldoni, G. Comelli, M. Jugovac, V. Feyer, and C.M. Schneider. "Multi-orbital charge transfer at highly oriented organic/metal interfaces". *Nature Communications* **8** (1), (2017), pp. 1-22.

DOI: 10.1038/s41467-017-00402-0

[14] G. Zamborlini, M. Jugovac, A. Cossaro, A. Verdini, L. Floreano, D. Lüftner, P. Puschnig, V. Feyer, and C.M. Schneider. "On-surface nickel porphyrin mimics the reactive center of an enzyme cofactor". *Chemical Communications* **54** (95), (2018), pp. 13423-13426.

DOI: 10.1039/C8CC06739B

[15] J.M. Gottfried. "Surface chemistry of porphyrins and phthalocyanines". *Surface Science Reports* **70** (3), (2015), pp. 259-379.

DOI: 10.1016/j.surfrep.2015.04.001

[16] W. Auwärter, D. Écija, F. Klappenberger, and J. V. Barth. "Porphyrins at interfaces". *Nature Chemistry* **7** (2), (2015), pp. 105-120.

DOI: 10.1038/nchem.2159

[17] F. Buchner, K. Flechtner, Y. Bai, E. Zillner, I. Kellner, H.P. Steinrück, H. Marbach, and J.M. Gottfried. "Coordination of iron atoms by tetraphenylporphyrin monolayers and multilayers on Ag(111) and formation of iron-tetraphenylporphyrin". *The Journal of Physical Chemistry C* **112** (39), (2008), pp. 15458-15465.

DOI: 10.1021/jp8052955

[18] K. Diller, F. Klappenberger, M. Marschall, K. Hermann, A. Nefedov, C. Wöll, and J. V. Barth. "Self-metalation of 2H-tetraphenylporphyrin on Cu(111): an x-ray spectroscopy study". *The Journal of Chemical Physics* **136** (1), (2012), pp. 014705.

DOI: 10.1063/1.3674165

[19] A. Rosa, G. Ricciardi, and E.J. Baerends. "Synergism of porphyrin-core saddling and twisting of meso-aryl substituants". *Journal of Physical Chemistry A* **110** (15), (2006), pp. 5180-5190.

DOI: 10.1021/jp060931i

[20] T. Wölfle, A. Görling, and W. Hieringer. "Conformational flexibility of metalloporphyrins studied by density-functional calculations". *Physical Chemistry Chemical Physics* **10** (37), (2008), pp. 5739-5742.

DOI: 10.1039/b800566b

[21] K.M. Barkigia, M.D. Berber, J. Fajer, C.J. Medforth, M.W. Renner, and K.M. Smith. "Nonplanar porphyrins. x-ray structures of (2,3,7,8,12,13,17,18-octaethyl- and -octamethyl-5,10,15,20-tetraphenylporphinato)zinc(II)". *Journal of the American Chemical Society* **112** (24), (1990), pp. 8851-8857.

DOI: 10.1021/ja00180a029

[22] M.S. Liao and S. Scheiner. "Electronic structure and bonding in metal porphyrins, metal = Fe, Co, Ni, Cu, Zn". *Journal of Chemical Physics* **117** (1), (2002), pp. 205-219.

DOI: 10.1063/1.1480872

[23] T.C. Berto, V.K.K. Praneeth, L.E. Goodrich, and N. Lehnert. "Iron-porphyrin NO complexes with covalently attached n-donor ligands: formation of a stable six-coordinate species in solution". *Journal of the American Chemical Society* **131** (47), (2009), pp. 17116-17126.

DOI: 10.1021/ja904368n

[24] A. Köbke, F. Gutzeit, F. Röhricht, A. Schlimm, J. Grunwald, F. Tuczek, M. Studniarek, D. Longo, F. Choueikani, E. Otero, P. Ohresser, S. Rohlf, S. Johannsen, F. Diekmann, K. Rossnagel, A. Weismann, T. Jasper-Toennies, C. Näther, R. Herges, R. Berndt, and M. Gruber. "Reversible coordination-induced spin-state switching in complexes on metal surfaces". *Nature Nanotechnology* **15** (1), (2020), pp. 18-21.

DOI: 10.1038/s41565-019-0594-8

[25] S. Mohnani and D. Bonifazi. "Supramolecular architectures of porphyrins on surfaces: the structural evolution from 1D to 2D to 3D to devices". *Coordination Chemistry Reviews* **254** (19-20), (2010), pp. 2342-2362.

DOI: 10.1016/j.ccr.2010.05.006

[26] M. Willenbockel, D. Lüftner, B. Stadtmüller, G. Koller, C. Kumpf, S. Soubatch, P. Puschnig, M.G. Ramseyc, and F.S. Tautz. "The interplay between interface structure, energy level alignment and chemical bonding strength at organic-metal interfaces". *Physical Chemistry Chemical Physics* **17** (3), (2015), pp. 1530-1548.

DOI: 10.1039/c4cp04595e

[27] F. Buchner, E. Zillner, M. Röckert, S. Gläel, H.P. Steinrück, and H. Marbach. "Substrate-mediated phase separation of two porphyrin derivatives on Cu(111)". *Chemistry - A European Journal* **17** (37), (2011), pp. 10226-10229.

DOI: 10.1002/chem.201100462

[28] J. Brede, M. Linares, S. Kuck, J. Schwöbel, A. Scarfato, S.H. Chang, G. Hoffmann, R. Wiesendanger, R. Lensen, P.H.J. Kouwer, J. Hoogboom, A.E. Rowan, M. Bröring, M. Funk, S. Stafström, F. Zerbetto, and R. Lazzaroni. "Dynamics of molecular self-ordering in tetraphenyl porphyrin monolayers on metallic substrates". *Nanotechnology* **20** (27), (2009), p. 275602.

DOI: 10.1088/0957-4484/20/27/275602

[29] F. Buchner, I. Kellner, W. Hieringer, A. Görling, H.P. Steinrück, and H. Marbach. "Ordering aspects and intramolecular conformation of tetraphenylporphyrins on Ag(111)". *Physical Chemistry Chemical Physics* **12** (40), (2010), pp. 13082-13090.

DOI: 10.1039/c004551a

[30] M.S. Dyer, A. Robin, S. Haq, R. Raval, M. Persson, and J. Klimeš. "Understanding the interaction of the porphyrin macrocycle to reactive metal substrates: structure, bonding, and adatom capture". *ACS Nano* **5** (3), (2011), pp. 1831-1838.

DOI: 10.1021/nn102610k

[31] K. Diller, F. Klappenberger, M. Marschall, K. Hermann, A. Nefedov, C. Wöll, and J. V Barth. "Self-metalation of 2H-tetraphenylporphyrin on Cu(111): an x-ray spectroscopy study". *The Journal of Chemical Physics* **136** (1), (2012), pp. 014705.

DOI: 10.1063/1.3674165

[32] F. Buchner, J. Xiao, E. Zillner, M. Chen, M. Röckert, S. Ditze, M. Stark, H.P. Steinrück, J.M. Gottfried, and H. Marbach. "Diffusion, rotation, and surface chemical bond of individual 2H-tetraphenylporphyrin molecules on Cu(111)". *Journal of Physical Chemistry C* **115** (49), (2011), pp. 24172-24177.

DOI: 10.1021/jp206675u

[33] H. Marbach and H.P. Steinrück. "Studying the dynamic behaviour of porphyrins as prototype functional molecules by scanning tunnelling microscopy close to room temperature". *Chem Commun* **50** (65), (2014), pp. 9034-9048.

DOI: 10.1039/C4CC01744G

[34] G. Di Santo, S. Blankenburg, C. Castellarin-Cudia, M. Fanetti, P. Borghetti, L. Sangaletti, L. Floreano, A. Verdini, E. Magnano, F. Bondino, C.A. Pignedoli, M.T. Nguyen, R. Gaspari, D. Passerone, and A. Goldoni. "Supramolecular engineering through temperature-induced chemical modification of 2H-tetraphenylporphyrin on Ag(111): flat phenyl conformation and possible dehydrogenation reactions". *Chemistry - A European Journal* **17** (51), (2011), pp. 14354-14359.

DOI: 10.1002/chem.201102268

[35] L.M. Arruda, M.E. Ali, M. Bernien, F. Nickel, J. Kopprasch, C. Czekelius, P.M. Oppeneer, and W. Kuch. "Modifying the magnetic anisotropy of an iron porphyrin molecule by an on-surface ring-closure reaction". *Journal of Physical Chemistry C* **123** (23), (2019), pp. 14547-14555.

DOI: 10.1021/acs.jpcc.9b03126

[36] B.W. Heinrich, G. Ahmadi, V.L. Müller, L. Braun, J.I. Pascual, and K.J. Franke. "Change of the magnetic coupling of a metal-organic complex with the substrate by a stepwise ligand reaction". *Nano Letters* **13** (10), (2013), pp. 4840-4843.

DOI: 10.1021/nl402575c

[37] T.G. Appleton, H.C. Clark, and L.E. Manzer. "The trans-influence: its measurement and significance". *Coordination Chemistry Reviews* **10** (3-4), (1973), pp. 335-422.

DOI: 10.1016/S0010-8545(00)80238-6

[38] W. Hieringer, K. Flechtner, A. Kretschmann, K. Seufert, W. Auwärter, J. V. Barth, A. Görling, H.P. Steinrück, and J.M. Gottfried. "The surface trans effect: influence of axial ligands on the surface chemical bonds of adsorbed metalloporphyrins". *Journal of the American Chemical Society* **133** (16), (2011), pp. 6206-6222.

DOI: 10.1021/ja1093502

[39] K. Flechtner, A. Kretschmann, H.P. Steinrück, and J.M. Gottfried. "NO-induced reversible switching of the electronic interaction between a porphyrin-coordinated cobalt ion and a silver surface". *Journal of the American Chemical Society* **129** (40), (2007), pp. 12110-12111.

DOI: 10.1021/ja0756725

[40] C. Wäckerlin, K. Tarafder, D. Siewert, J. Girovsky, T. Hählen, C. Iacovita, A. Kleibert, F. Nolting, T.A. Jung, P.M. Oppeneer, and N. Ballav. "On-surface coordination chemistry of planar molecular spin systems: novel magnetochemical effects induced by axial ligands". *Chemical Science* **3** (11), (2012), pp. 3154-3160.

DOI: 10.1039/c2sc20828h

[41] L.X. Chen, W.J.H. Jäger, G. Jennings, D.J. Gosztota, A. Munkholm, and J.P. Hessler. "Capturing a photoexcited molecular structure through time-domain x-ray absorption fine structure". *Science* **292** (5515), (2001), pp. 262-264.

DOI: 10.1126/science.1057063

[42] S. Venkataramani, U. Jana, M. Dommaschk, F.D. Sonnichsen, F. Tuczek, and R. Herges. "Magnetic bistability of molecules in homogeneous solution at room temperature". *Science* **331** (6016), (2011), pp. 445-448.

DOI: 10.1126/science.1201180

[43] G. Zamborlini. "Organic-metal hybrid interfaces at the mesoscopic scale". Ph. D. Dissertation, Universität Duisburg-Essen, Duisburg, 2017. Accessed on: November 2, 2021. [Online].

http://hdl.handle.net/2128/19490

[44] P. Puschnig, S. Berkebile, A.J. Fleming, G. Koller, K. Emtsev, T. Seyller, J.D. Riley, C. Ambrosch-Draxl, F.P. Netzer, and M.G. Ramsey. "Reconstruction of molecular orbital densities from photoemission data". *Science* **326** (5953), (2009), pp. 702-706.

DOI: 10.1126/science.1176105

[45] N.A. Rakow and K.S. Suslick. "A colorimetric sensor array for odour visualization". *Nature* **406** (6797), (2000), pp. 710-713.

DOI: 10.1038/35021028

[46] I. Mochida, K. Suetsugu, H. Fujitsu, and K. Takeshita. "Enhanced catalytic activity of cobalt tetraphenylporphyrin on titanium dioxide by evacuation at elevated temperatures for intensifying the complex-support interaction". *The Journal of Physical Chemistry* **87** (9), (1983), pp. 1524-1529.

DOI: 10.1021/j100232a015

[47] H.M. Sturmeit, I. Cojocariu, M. Jugovac, A. Cossaro, A. Verdini, L. Floreano, A. Sala, G. Comelli, S. Moro, M. Stredansky, M. Corva, E. Vesselli, P. Puschnig, C.M. Schneider, V. Feyer, G. Zamborlini, and M. Cinchetti. "Molecular anchoring stabilizes low valence Ni(I)TPP on copper against thermally induced chemical changes". *Journal of Materials Chemistry C* **8** (26), (2020), pp. 8876-8886.

DOI: 10.1039/d0tc00946f

[48] A. Damascelli, Z. Hussain, and Z.X. Shen. "Angle-resolved photoemission studies of the cuprate superconductors". *Reviews of Modern Physics* **75** (2), (2003), pp. 473-541.

DOI: 10.1103/RevModPhys.75.473

[49] I.G. Hill, D. Milliron, J. Schwartz, and A. Kahn. "Organic semiconductor interfaces: electronic structure and transport properties". *Applied Surface Science* **166** (1-4), (2000), pp. 354-362.

DOI: 10.1016/S0169-4332(00)00449-9

[50] S. Hüfner. *Photoelectron spectroscopy- Principles and applications*, 3rd ed. Berlin, Heidelberg, Springer-Verlag Berlin Heidelberg, 2003.

DOI: 10.1007/978-3-662-09280-4

[51] A. Damascelli. "Probing the electronic structure of complex systems by ARPES". *Physica Scripta* **T109**, (2004), pp. 61.

DOI: 10.1238/Physica.Topical.109a00061

[52] W. Schattke. "Photoemission within and beyond the one-step model". *Progress in Surface Science* **54** (3-4), (1997), pp. 211-227.

DOI: 10.1016/S0079-6816(97)00005-1

[53] J.B. Pendry. "Theory of photoemission". *Surface Science* **57** (2), (1976), pp. 679-705.

DOI: 10.1016/0039-6028(76)90355-1

[54] A.M. Bradshaw and D.P. Woodruff. "Molecular orbital tomography for adsorbed molecules: is a correct description of the final state really unimportant?". *New Journal of Physics* **17** (1), (2015), pp. 13033.

DOI: 10.1088/1367-2630/17/1/013033

[55] X. Yang, L. Egger, P. Hurdax, H. Kaser, D. Lüftner, F.C. Bocquet, G. Koller, A. Gottwald, P. Tegeder, M. Richter, M.G. Ramsey, P. Puschnig, S. Soubatch, and F.S. Tautz. "Identifying surface reaction intermediates with photoemission tomography". *Nature Communications* **10** (1), (2019), pp. 1-6.

DOI: 10.1038/s41467-019-11133-9

[56] I. Cojocariu, F. Feyersinger, P. Puschnig, L. Schio, L. Floreano, V. Feyer, and C.M. Schneider. "Insight into intramolecular chemical structure modifications by on-surface reaction using photoemission tomography". *Chemical Communications* **57** (24), (2021), pp. 3050-3053.

DOI: 10.1039/D1CC00311A

[57] M. Scheffler, K. Kambe, and F. Forstmann. "Angled resolved photoemission from adsorbates: theoretical considerations of polarization effects and symmetry". *Solid State Communications* **25** (2), (1978), pp. 93-99.

DOI: 10.1016/0038-1098(78)90365-4

[58] P. Puschnig, G. Koller, C. Draxl, and M.G. Ramsey. "The structure of molecular orbitals investigated by angle-resolved photoemission". In: *Small Organic Molecules on Surfaces*. (2013), pp.3-23.

DOI: 10.1007/978-3-642-33848-9_1

[59] K. Schönauer, S. Weiss, V. Feyer, D. Lüftner, B. Stadtmüller, D. Schwarz, T.

Sueyoshi, C. Kumpf, P. Puschnig, M.G. Ramsey, F.S. Tautz, and S. Soubatch. "Charge transfer and symmetry reduction at the CuPC/Ag(110) interface studied by photoemission tomography". *Physical Review B* **94** (20), (2016), pp. 205144.

DOI: 10.1103/PhysRevB.94.205144

[60] C.M. Schneider, C. Wiemann, M. Patt, V. Feyer, L. Plucinski, I.P. Krug, M. Escher, N. Weber, M. Merkel, O. Renault, and N. Barrett. "Expanding the view into complex material systems: from micro-ARPES to nanoscale haxpes". *Journal of Electron Spectroscopy and Related Phenomena* **185** (10), (2012), pp. 330-339.

DOI: 10.1016/j.elspec.2012.08.003

[61] C. Nordling, E. Sokolowski, and K. Siegbahn. "Precision method for obtaining absolute values of atomic binding energies". *Physical Review* **105** (5), (1957), pp. 1676-1677.

DOI: 10.1103/PhysRev.105.1676

[62] C. Wang, Q. Fan, S. Hu, H. Ju, X. Feng, Y. Han, H. Pan, J. Zhu, and J.M. Gottfried. "Coordination reaction between tetraphenylporphyrin and nickel on a TiO_2(110) surface". *Chemical Communications* **50** (61), (2014), pp. 8291-8294.

DOI: 10.1039/c4cc02919d

[63] T. Lukasczyk, K. Flechtner, L.R. Merte, N. Jux, F. Maier, J.M. Gottfried, and H.P. Steinrück. "Interaction of cobalt(II) tetraarylporphyrins with a Ag(111) surface studied with photoelectron spectroscopy". *The Journal of Physical Chemistry C* **111** (7), (2007), pp. 3090-3098.

DOI: 10.1021/jp0652345

[64] M. Röckert, M. Franke, Q. Tariq, S. Ditze, M. Stark, P. Uffinger, D. Wechsler, U. Singh, J. Xiao, H. Marbach, H.P. Steinrück, and O. Lytken. "Coverage- and temperature-dependent metalation and dehydrogenation of tetraphenylporphyrin on Cu(111)". *Chemistry - A European Journal* **20** (29), (2014), pp. 8948-8953.

DOI: 10.1002/chem.201402420

[65] P. Fornasini. "Introduction to x-ray absorption spectroscopy". In: *Synchrotron Radiation*, 1st ed. S. Mobilio, F. Boscherini, C. Meneghini, Eds. Berlin, Heidelberg, Springer-Verlag Berlin Heidelberg, 2015, ch. 6, pp.181-211.

DOI: 10.1007/978-3-642-55315-8_6

[66] A. Nefedov and C. Wöll. "Advanced applications of nexafs spectroscopy for functionalized surfaces". In: *Surface Science Techniques*. (2013), pp.277-303.

DOI: 10.1007/978-3-642-34243-1_10

[67] G. Hähner. "Near edge x-ray absorption fine structure spectroscopy as a tool to probe electronic and structural properties of thin organic films and liquids". *Chemical Society Reviews* **35** (12), (2006), pp. 1244-1255.

DOI: 10.1039/b509853j

[68] J. Stöhr. *NEXAFS spectroscopy*, 1st Ed. Berlin, Heidelberg, Springer-Verlag Berlin Heidelberg, 1992.

DOI: 10.1007/978-3-662-02853-7

[69] K. Syres, A. Thomas, F. Bondino, M. Malvestuto, and M. Grätzel. "Dopamine

adsorption on anatase TiO_2(101): a photoemission and nexafs spectroscopy study". *Langmuir* **26** (18), (2010), pp. 14548-14555.

DOI: 10.1021/la1016092

[70] L. Floreano, A. Cossaro, R. Gotter, A. Verdini, G. Bavdek, F. Evangelista, A. Ruocco, A. Morgante, and D. Cvetko. "Periodic arrays of cu-phthalocyanine chains on Au(110)". *Journal of Physical Chemistry C* **112** (29), (2008), pp. 10794-10802.

DOI: 10.1021/jp711140e

[71] L. Floreano, G. Naletto, D. Cvetko, R. Gotter, M. Malvezzi, L. Marassi, A. Morgante, A. Santaniello, A. Verdini, F. Tommasini, and G. Tondello. "Performance of the grating-crystal monochromator of the ALOISA beamline at the Elettra synchrotron". *Review of Scientific Instruments* **70** (10), (1999), pp. 3855-3864.

DOI: 10.1063/1.1150001

[72] "ALOISA web page (Elettra synchrotron web site)". Accessed on: November 2, 2021.

https://www.elettra.trieste.it/elettra-beamlines/aloisa.html

[73] J. Stöhr and H.C. Siegmann. *Magnetism: From Fundamentals to Nanoscale Dynamics*, 1st ed. Berlin, Heidelberg, Springer-Verlag Berlin Heidelberg, 2006.

DOI: 10.1007/978-3-540-30283-4

[74] S.W. Lovesey and S.P. Collins. *X-ray scattering and absorption by magnetic materials*. New York, Oxford University Press, 1996.

[75] B.T. Thole, P. Carra, F. Sette, and G. Van Der Laan. "X-ray circular dichroism as a probe of orbital magnetization". *Physical Review Letters* **68** (12), (1992), pp. 1943-1946.

DOI: 10.1103/PhysRevLett.68.1943

[76] P. Carra, B.T. Thole, M. Altarelli, and X. Wang. "X-ray circular dichroism and local magnetic fields". *Physical Review Letters* **70** (5), (1993), pp. 694-697.

DOI: 10.1103/PhysRevLett.70.694

[77] C.T. Chen, Y.U. Idzerda, H.J. Lin, N. V. Smith, G. Meigs, E. Chaban, G.H. Ho, E. Pellegrin, and F. Sette. "Experimental confirmation of the x-ray magnetic circular dichroism sum rules for iron and cobalt". *Physical Review Letters* **75** (1), (1995), pp. 152-155.

DOI: 10.1103/PhysRevLett.75.152

[78] S. Stepanow, A. Mugarza, G. Ceballos, P. Moras, J.C. Cezar, C. Carbone, and P. Gambardella. "Giant spin and orbital moment anisotropies of a Cu-phthalocyanine monolayer". *Physical Review B - Condensed Matter and Materials Physics* **82** (1), (2010), pp. 014405.

DOI: 10.1103/PhysRevB.82.014405

[79] C. Piamonteze, P. Miedema, and F.M.F. De Groot. "Accuracy of the spin sum rule in XMCD for the transition-metal L edges from manganese to copper". *Physical Review B - Condensed Matter and Materials Physics* **80** (18), (2009), pp. 184410.

DOI: 10.1103/PhysRevB.80.184410

[80] F. de Groot and A. Kotani. *Core level spectroscopy of solids*. Boca Raton, FL, CRC Press, 2008.

DOI: 10.1201/9781420008425

[81] C. Piamonteze, U. Flechsig, S. Rusponi, J. Dreiser, J. Heidler, M. Schmidt, R. Wetter, M. Calvi, T. Schmidt, H. Pruchova, J. Krempasky, C. Quitmann, H. Brune, and F. Nolting. "X-treme beamline at SLS: x-ray magnetic circular and linear dichroism at high field and low temperature". *Journal of Synchrotron Radiation* **19** (5), (2012), pp. 661-674.

DOI: 10.1107/S0909049512027847

[82] B.E. Hayden. "Reflection absorption infrared spectroscopy". In: *Vibrational Spectroscopy of Molecules on Surfaces*, 1st ed. T. E. Madey, J. T. Yates Jr., Eds. Boston, Springer, 1987, ch. 7, pp.267-344.

DOI: 10.1007/978-1-4684-8759-6_7

[83] N.D. Lang and W. Kohn. "Theory of metal surfaces: induced surface charge and image potential". *Physical Review B* **7** (8), (1973), pp. 3541-3550.

DOI: 10.1103/PhysRevB.7.3541

[84] F. Hoffmann. "Infrared reflection-absorption spectroscopy of adsorbed molecules". *Surface Science Reports* **3** (2-3), (1983), pp. 107-192.

DOI: 10.1016/0167-5729(83)90001-8

[85] C. Schuschke, C. Hohner, M. Jevric, A. Ugleholdt Petersen, Z. Wang, M. Schwarz, M. Kettner, F. Waidhas, L. Fromm, C.J. Sumby, A. Görling, O. Brummel, K. Moth-Poulsen, and J. Libuda. "Solar energy storage at an atomically defined organic-oxide hybrid interface". *Nature Communications* **10** (1), (2019), pp. 1-10.

DOI: 10.1038/s41467-019-10263-4

[86] C.J. Chen. *Introduction to scanning tunneling microscopy*, New York, Oxford University Press, 1993.

DOI: 10.1093/acprof:oso/9780199211500.001.0001

[87] J. Tersoff and D.R. Hamann. "Theory and application for the scanning tunneling microscope". *Physical Review Letters* **50** (25), (1983), pp. 1998-2001.

DOI: 10.1103/PhysRevLett.50.1998

[88] P.K. Hansma and J. Tersoff. "Scanning tunneling microscopy". *Journal of Applied Physics* **61** (2), (1987), pp. R1-R24.

DOI: 10.1063/1.338189

[89] X. Yang, I. Krieger, D. Lüftner, S. Weiß, T. Heepenstrick, M. Hollerer, P. Hurdax, G. Koller, M. Sokolowski, P. Puschnig, M.G. Ramsey, F.S. Tautz, and S. Soubatch. "On the decoupling of molecules at metal surfaces". *Chemical Communications* **54** (65), (2018), pp. 9039-9042.

DOI: 10.1039/c8cc03334j

[90] I. Cojocariu, H.M. Sturmeit, G. Zamborlini, A. Cossaro, A. Verdini, L. Floreano, E. D'Incecco, M. Stredansky, E. Vesselli, M. Jugovac, M. Cinchetti, V. Feyer, and C.M. Schneider. "Evaluation of molecular orbital symmetry via oxygen-induced charge transfer quenching at a metal-organic interface". *Applied Surface Science*

504, (2020), pp. 144343.

DOI: 10.1016/j.apsusc.2019.144343

[91] M. Stredansky, S. Moro, M. Corva, M. Jugovac, G. Zamborlini, V. Feyer, C.M. Schneider, I. Cojocariu, H.M. Sturmeit, M. Cinchetti, A. Verdini, A. Cossaro, L. Floreano, and E. Vesselli. "Vibronic fingerprints of the nickel oxidation states in surface-supported porphyrin arrays". *The Journal of Physical Chemistry C* **124** (11), (2020), pp. 6297-6303.

DOI: 10.1021/acs.jpcc.0c01387

[92] T.S. Rush, P.M. Kozlowski, C.A. Piffat, R. Kumble, M.Z. Zgierski, and T.G. Spiro. "Computational modeling of metalloporphyrin structure and vibrational spectra: porphyrin ruffling in NiTPP". *The Journal of Physical Chemistry B* **104** (20), (2000), pp. 5020-5034.

DOI: 10.1021/jp000266s

[93] J. Brede, M. Linares, R. Lensen, A.E. Rowan, M. Funk, M. Bröring, G. Hoffmann, and R. Wiesendanger. "Adsorption and conformation of porphyrins on metallic surfaces". *Journal of Vacuum Science & Technology B: Microelectronics and Nanometer Structures* **27** (2), (2009), pp. 799.

DOI: 10.1116/1.3010722

[94] J. Xiao, S. Ditze, M. Chen, F. Buchner, M. Stark, M. Drost, H.P. Steinrück, J.M. Gottfried, and H. Marbach. "Temperature-dependent chemical and structural transformations from 2H-tetraphenylporphyrin to copper(II)-tetraphenylporphyrin on Cu(111)". *Journal of Physical Chemistry C* **116** (22), (2012), pp. 12275-12282.

DOI: 10.1021/jp301757h

[95] D. Wechsler, M. Franke, Q. Tariq, L. Zhang, T.L. Lee, P.K. Thakur, N. Tsud, S. Bercha, K.C. Prince, H.P. Steinrück, and O. Lytken. "Adsorption structure of cobalt tetraphenylporphyrin on Ag(100)". *Journal of Physical Chemistry C* **121** (10), (2017), pp. 5667-5674.

DOI: 10.1021/acs.jpcc.7b00518

[96] M. Chen, X. Feng, L. Zhang, H. Ju, Q. Xu, J. Zhu, J.M. Gottfried, K. Ibrahim, H. Qian, and J. Wang. "Direct synthesis of nickel(II) tetraphenylporphyrin and its interaction with a Au(111) surface: a comprehensive study". *Journal of Physical Chemistry C* **114** (21), (2010), pp. 9908-9916.

DOI: 10.1021/jp102031m

[97] M. Wuttig, R. Franchy, and H. Ibach. "Oxygen on Cu(100) - a case of an adsorbate induced reconstruction". *Surface Science* **213** (1), (1989), pp. 103-136.

DOI: 10.1016/0039-6028(89)90254-9

[98] Q. Zhu, L. Zou, G. Zhou, W.A. Saidi, and J.C. Yang. "Early and transient stages of Cu oxidation: atomistic insights from theoretical simulations and in situ experiments". *Surface Science* **652**, (2016), pp. 98-113.

DOI: 10.1016/j.susc.2016.03.003

[99] S.J. Tjung, Q. Zhang, J.J. Repicky, S.F. Yuk, X. Nie, N.M. Santagata, A. Asthagiri, and J.A. Gupta. "STM and dft studies of CO_2 adsorption on Cu(100)-O surface". *Surface Science* **679**, (2018), pp. 50-55.

DOI: 10.1016/j.susc.2018.08.013

[100] J.H. Onuferko and D.P. Woodruff. "Leed structural study of the adsorption of oxygen on Cu {100} surfaces". *Surface Science* **95** (2-3), (1980), pp. 555-570.

DOI: 10.1016/0039-6028(80)90195-8

[101] J.E. Nitschke. "The electronic structure of the NiTPP/O/Cu(100) interface investigated by a combined spectromicroscopic approach". M. S. thesis, Technische Universität Dortmund, Dortmund, 2020.

[102] L. Cao, Y.Z. Wang, T.X. Chen, W.H. Zhang, X.J. Yu, K. Ibrahim, J.O. Wang, H.J. Qian, F.Q. Xu, D.C. Qi, and A.T.S. Wee. "Charge transfer dynamics of 3,4,9,10-perylene-tetracarboxylic-dianhydride molecules on Au(111) probed by resonant photoemission spectroscopy". *The Journal of Chemical Physics* **135** (17), (2011), pp. 174701.

DOI: 10.1063/1.3656834

[103] N. Schmidt, R. Fink, and W. Hieringer. "Assignment of near-edge x-ray absorption fine structure spectra of metalloporphyrins by means of time-dependent density-functional calculations". *Journal of Chemical Physics* **133** (5), (2010).

DOI: 10.1063/1.3435349

[104] C.C. Fernández, D. Wechsler, T.C.R. Rocha, H.P. Steinrück, O. Lytken, and F.J. Williams. "Adsorption geometry of carboxylic acid functionalized porphyrin molecules on TiO_2(110)". *Surface Science* **689**, (2019), pp. 121462.

DOI: 10.1016/j.susc.2019.121462

[105] S.A. Krasnikov, N.N. Sergeeva, M.M. Brzhezinskaya, A.B. Preobrajenski, Y.N. Sergeeva, N.A. Vinogradov, A.A. Cafolla, M.O. Senge, and A.S. Vinogradov. "An x-ray absorption and photoemission study of the electronic structure of Ni porphyrins and Ni n-confused porphyrin". *Journal of Physics Condensed Matter* **20** (23), (2008), pp. 0-6.

DOI: 10.1088/0953-8984/20/23/235207

[106] D.G. de Oteyza, A. Sakko, A. El-Sayed, E. Goiri, L. Floreano, A. Cossaro, J.M. Garcia-Lastra, A. Rubio, and J.E. Ortega. "Inversed linear dichroism in F K-edge NEXAFS spectra of fluorinated planar aromatic molecules". *Physical Review B* **86** (7), (2012), pp. 075469.

DOI: 10.1103/PhysRevB.86.075469

[107] M.G. Betti, P. Gargiani, R. Frisenda, R. Biagi, A. Cossaro, A. Verdini, L. Floreano, and C. Mariani. "Localized and dispersive electronic states at ordered FePc and CoPc chains on Au(110)". *The Journal of Physical Chemistry C* **114** (49), (2010), pp. 21638-21644.

DOI: 10.1021/jp108734u

[108] R. De Francesco, M. Stener, and G. Fronzoni. "Theoretical study of near-edge x-ray absorption fine structure spectra of metal phthalocyanines at C and N K-edges". *The Journal of Physical Chemistry A* **116** (11), (2012), pp. 2885-2894.

DOI: 10.1021/jp2109913

[109] M.V. Nardi, F. Detto, L. Aversa, R. Verucchi, G. Salviati, S. Iannotta, and M.

Casarin. "Electronic properties of CuPc and H2Pc: an experimental and theoretical study". *Physical Chemistry Chemical Physics* **15** (31), (2013), pp. 12864.

DOI: 10.1039/c3cp51224j

[110] T.C. Tseng, C. Urban, Y. Wang, R. Otero, S.L. Tait, M. Alcamí, D. Écija, M. Trelka, J.M. Gallego, N. Lin, M. Konuma, U. Starke, A. Nefedov, A. Langner, C. Wöll, M.Á. Herranz, F. Martín, N. Martín, K. Kern, and R. Miranda. "Charge-transfer-induced structural rearrangements at both sides of organic/metal interfaces". *Nature Chemistry* **2** (5), (2010), pp. 374-379.

DOI: 10.1038/nchem.591

[111] A. Calabrese, L. Floreano, A. Verdini, C. Mariani, and M.G. Betti. "Filling empty states in a CuPc single layer on the Au(110) surface via electron injection". *Physical Review B - Condensed Matter and Materials Physics* **79** (11), (2009), pp. 115446.

DOI: 10.1103/PhysRevB.79.115446

[112] H. Wang, S.M. Butorin, A.T. Young, and J. Guo. "Nickel oxidation states and spin states of bioinorganic complexes from nickel L-edge x-ray absorption and resonant inelastic x-ray scattering". *Journal of Physical Chemistry C* **117** (47), (2013), pp. 24767-24772.

DOI: 10.1021/jp402404b

[113] F.A. Cotton, G. Wilkinson, A.C. Murillo, and M. Bochmann. *Advanced inorganic chemistry*, 6th ed. New York, Wiley, 1999.

[114] R. Wallauer, M. Raths, K. Stallberg, L. Münster, D. Brandstetter, X. Yang, J. Güdde, P. Puschnig, S. Soubatch, C. Kumpf, F.C. Bocquet, F.S. Tautz, and U. Höfer. "Tracing orbital images on ultrafast time scales". *Science* **371** (6533), (2021), pp. 1056-1059.

DOI: 10.1126/science.abf3286

[115] P. Wahl, L. Diekhöner, G. Wittich, L. Vitali, M.A. Schneider, and K. Kern. "Kondo effect of molecular complexes at surfaces: ligand control of the local spin coupling". *Physical Review Letters* **95** (16), (2005), pp. 166601.

DOI: 10.1103/PhysRevLett.95.166601

[116] P. Gambardella, S. Stepanow, A. Dmitriev, J. Honolka, F.M.F. De Groot, M. Lingenfelder, S. Sen Gupta, D.D. Sarma, P. Bencok, S. Stanescu, S. Clair, S. Pons, N. Lin, A.P. Seitsonen, H. Brune, J. V. Barth, and K. Kern. "Supramolecular control of the magnetic anisotropy in two-dimensional high-spin Fe arrays at a metal interface". *Nature Materials* **8** (3), (2009), pp. 189-193.

DOI: 10.1038/nmat2376

[117] L. Giovanelli, A. Savoyant, M. Abel, F. Maccherozzi, Y. Ksari, M. Koudia, R. Hayn, F. Choueikani, E. Otero, P. Ohresser, J.M. Themlin, S.S. Dhesi, and S. Clair. "Magnetic coupling and single-ion anisotropy in surface-supported Mn-based metal–organic networks". *The Journal of Physical Chemistry C* **118** (22), (2014), pp. 11738-11744.

DOI: 10.1021/jp502209q

[118] M.N. Faraggi, V.N. Golovach, S. Stepanow, T.C. Tseng, N. Abdurakhmanova, C.S. Kley, A. Langner, V. Sessi, K. Kern, and A. Arnau. "Modeling ferro- and

antiferromagnetic interactions in metal–organic coordination networks". *The Journal of Physical Chemistry C* **119** (1), (2015), pp. 547-555.

DOI: 10.1021/jp512019w

[119] M. a. Blanco-Rey, A. Sarasola, C. Nistor, L. Persichetti, C. Stamm, C. Piamonteze, P. Gambardella, S. Stepanow, M.M. Otrokov, V.N. Golovach, and A. Arnau. "Magnetic properties of metal–organic coordination networks based on 3d transition metal atoms". *Molecules* **23** (4), 964, (2018), pp. 1-18.

DOI: 10.3390/molecules23040964

[120] S. Carlotto, M. Sambi, F. Sedona, A. Vittadini, and M. Casarin. "A theoretical study of the occupied and unoccupied electronic structure of high- and intermediate-spin transition metal phthalocyaninato (Pc) complexes: VPc, CrPc, MnPc, and FePc". *Nanomaterials* **11** (1), (2020), pp. 54.

DOI: 10.3390/nano11010054

[121] H. Wende, M. Bernien, J. Luo, C. Sorg, N. Ponpandian, J. Kurde, J. Miguel, M. Piantek, X. Xu, P. Eckhold, W. Kuch, K. Baberschke, P.M. Panchmatia, B. Sanyal, P.M. Oppeneer, and O. Eriksson. "Substrate-induced magnetic ordering and switching of iron porphyrin molecules". *Nature Materials* **6** (7), (2007), pp. 516-520.

DOI: 10.1038/nmat1932

[122] K. Seufert, M.L. Bocquet, W. Auwärter, A. Weber-Bargioni, J. Reichert, N. Lorente, and J. V. Barth. "Cis-dicarbonyl binding at cobalt and iron porphyrins with saddle-shape conformation". *Nature Chemistry* **3** (2), (2011), pp. 114-119.

DOI: 10.1038/nchem.956

[123] S. Stepanow, A. Lodi Rizzini, C. Krull, J. Kavich, J.C. Cezar, F. Yakhou-Harris, P.M. Sheverdyaeva, P. Moras, C. Carbone, G. Ceballos, A. Mugarza, and P. Gambardella. "Spin tuning of electron-doped metal-phthalocyanine layers". *Journal of the American Chemical Society* **136** (14), (2014), pp. 5451-5459.

DOI: 10.1021/ja501204q

[124] C. Krull, R. Robles, A. Mugarza, and P. Gambardella. "Site- and orbital-dependent charge donation and spin manipulation in electron-doped metal phthalocyanines". *Nature Materials* **12** (4), (2013), pp. 337-343.

DOI: 10.1038/nmat3547

[125] Y. Hasegawa, Y. Yamada, and M. Sasaki. "Reordering and disordering of the copper hexadecafluorophthalocyanine ($F_{16}CuPc$) monolayer by K doping". *Journal of Physical Chemistry C* **118** (42), (2014), pp. 24490-24496.

DOI: 10.1021/jp506682t

[126] M.H. Chang, Y.H. Chang, N.Y. Kim, H. Kim, S.H. Lee, M.S. Choi, Y.H. Kim, and S.J. Kahng. "Tuning and sensing spin interactions in Co-porphyrin/Au with NH_3 and NO_2 binding". *Physical Review B* **100** (24), (2019), pp. 245406.

DOI: 10.1103/PhysRevB.100.245406

[127] H.M. Sturmeit, I. Cojocariu, A. Windischbacher, P. Puschnig, C. Piamonteze, M. Jugovac, A. Sala, C. Africh, G. Comelli, A. Cossaro, A. Verdini, L. Floreano, M. Stredansky, E. Vesselli, C. Hohner, M. Kettner, J. Libuda, C.M. Schneider, G.

Zamborlini, M. Cinchetti, and V. Feyer. "Room-Temperature on-spin-switching and tuning in a porphyrin-based multifunctional interface". *Small* (October 12, 2021), pp. 2104779.

DOI: 10.1002/smll.202104779

[128] G. Di Santo, C. Castellarin-Cudia, M. Fanetti, B. Taleatu, P. Borghetti, L. Sangaletti, L. Floreano, E. Magnano, F. Bondino, and A. Goldoni. "Conformational adaptation and electronic structure of 2H-tetraphenylporphyrin on Ag(111) during Fe metalation". *Journal of Physical Chemistry C* **115** (10), (2011), pp. 4155-4162.

DOI: 10.1021/jp111151n

[129] M. Verónica Rivas, L.P. Méndez De Leo, M. Hamer, R. Carballo, and F.J. Williams. "Self-assembled monolayers of disulfide Cu porphyrins on au surfaces: adsorption induced reduction and demetalation". *Langmuir* **27** (17), (2011), pp. 10714-10721.

DOI: 10.1021/la2020836

[130] K. Diller, F. Klappenberger, F. Allegretti, A.C. Papageorgiou, S. Fischer, A. Wiengarten, S. Joshi, K. Seufert, D. Écija, W. Auwärter, and J. V. Barth. "Investigating the molecule-substrate interaction of prototypic tetrapyrrole compounds: adsorption and self-metalation of porphine on Cu(111)". *Journal of Chemical Physics* **138** (15), (2013), pp. 154710.

DOI: 10.1063/1.4800771

[131] M.E. Bartram and B.E. Koel. "The molecular adsorption of NO_2 and the formation of N_2O_3 on au(111)". *Surface Science* **213** (1), (1989), pp. 137-156.

DOI: 10.1016/0039-6028(89)90255-0

[132] T.J. Dines, C.H. Rochester, and A.M. Ward. "Infrared and raman study of the adsorption of nitrogen oxides on titania-supported vanadia catalysts". *Journal of the Chemical Society, Faraday Transactions* **87** (10), (1991), pp. 1617-1622.

DOI: 10.1039/FT9918701617

[133] J. Wang and B.E. Koel. "IRAS studies of NO_2, N_2, O_3, and N_2O_4 adsorbed on Au(111) surfaces and reactions with coadsorbed H_2O". *The Journal of Physical Chemistry A* **102** (44), (1998), pp. 8573-8579.

DOI: 10.1021/jp982061d

[134] R. V. St. Louis and B. Crawford. "Infrared spectrum of matrix-isolated NO_2". *The Journal of Chemical Physics* **42** (3), (1965), pp. 857-864.

DOI: 10.1063/1.1696071

[135] M.H. Chang, N.Y. Kim, Y.H. Chang, Y. Lee, U.S. Jeon, H. Kim, Y.H. Kim, and S.J. Kahng. "O_2, NO_2 and NH_3 coordination to Co-porphyrin studied with scanning tunneling microscopy on Au(111)". *Nanoscale* **11** (17), (2019), pp. 8510-8517.

DOI: 10.1039/c9nr00843h

[136] H. Wang, S.M. Butorin, A.T. Young, and J. Guo. "Nickel oxidation states and spin states of bioinorganic complexes from nickel L- edge x - ray absorption and resonant inelastic x - ray scattering". *The Journal of Physical Chemistry C* **117** (47), (2013), pp. 24767–24772.

DOI: 10.1021/jp402404b

[137] I.G. Rau, S. Baumann, S. Rusponi, F. Donati, S. Stepanow, L. Gragnaniello, J. Dreiser, C. Piamonteze, F. Nolting, S. Gangopadhyay, O.R. Albertini, R.M. Macfarlane, C.P. Lutz, B.A. Jones, P. Gambardella, A.J. Heinrich, and H. Brune. "Reaching the magnetic anisotropy limit of a 3d metal atom". *Science* **344** (6187), (2014), pp. 988-992.

DOI: 10.1126/science.1252841

[138] H. Geisler, G. Odörfer, G. Illing, R. Jaeger, H.J. Freund, G. Watson, E.W. Plummer, M. Neuber, and M. Neumann. "NO_2 adsorption on Ni(100): a comparison of NO_2 with CO_2 adsorption". *Surface Science* **234** (3), (1990), pp. 237-250.

DOI: 10.1016/0039-6028(90)90557-O

[139] W.H.E. Schwarz, T.C. Chang, and J.P. Connerade. "Core-electron excitation in NO_2". *Chemical Physics Letters* **49** (2), (1977), pp. 207-212.

DOI: 10.1016/0009-2614(77)80571-X

[140] S. Stepanow, J. Honolka, P. Gambardella, L. Vitali, N. Abdurakhmanova, T.C. Tseng, S. Rauschenbach, S.L. Tait, V. Sessi, S. Klyatskaya, M. Ruben, and K. Kern. "Spin and orbital magnetic moment anisotropies of monodispersed bis(phthalocyaninato)terbium on a copper surface". *Journal of the American Chemical Society* **132** (34), (2010), pp. 11900-11901.

DOI: 10.1021/ja105124r

[141] C.F. Hermanns, M. Bernien, A. Krüger, W. Walter, Y.M. Chang, E. Weschke, and W. Kuch. "Huge magnetically coupled orbital moments of Co porphyrin molecules and their control by Co adsorption". *Physical Review B - Condensed Matter and Materials Physics* **88** (10), (2013), pp. 104420.

DOI: 10.1103/PhysRevB.88.104420

[142] M.S. Liao and S. Scheiner. "Electronic structure and bonding in unligated and ligated Fe^{II} porphyrins". *Journal of Chemical Physics* **116** (9), (2002), pp. 3635-3645.

DOI: 10.1063/1.1447902

[143] G. Marchand, H. Roy, D. Mendive-Tapia, and D. Jacquemin. "N-confused porphyrin tautomers: lessons from density functional theory". *Physical Chemistry Chemical Physics* **17** (7), (2015), pp. 5290-5297.

DOI: 10.1039/c4cp05158k

[144] P.S. Deimel, R.M. Bababrik, B. Wang, P.J. Blowey, L.A. Rochford, P.K. Thakur, T.L. Lee, M.L. Bocquet, J. V. Barth, D.P. Woodruff, D.A. Duncan, and F. Allegretti. "Direct quantitative identification of the “surface *trans*-effect”". *Chemical Science* **7** (9), (2016), pp. 5647-5656.

DOI: 10.1039/c6sc01677d

[145] S. Thies, C. Bornholdt, F. Köhler, F.D. Sönnichsen, C. Näther, F. Tuczek, and R. Herges. "Coordination-induced spin crossover (cisco) through axial bonding of substituted pyridines to nickel-porphyrins: σ-donor versus π-acceptor effects". *Chemistry - A European Journal* **16** (33), (2010), pp. 10074-10083.

DOI: 10.1002/chem.201000603

[146] X. Yang, D. Luo, Y. Xiang, L. Zhao, M. Anaya, Y. Shen, J. Wu, W. Yang, Y. Chiang, Y. Tu, R. Su, Q. Hu, H. Yu, G. Shao, W. Huang, T.P. Russell, Q. Gong,

S.D. Stranks, W. Zhang, and R. Zhu. "Buried interfaces in halide perovskite photovoltaics". *Advanced Materials* **33** (7), (2021), pp. 2006435.

DOI: 10.1002/adma.202006435

[147] C. Wäckerlin, D. Siewert, T.A. Jung, and N. Ballav. "On-surface coordination chemistry: direct imaging of the conformational freedom of an axial ligand at room temperature". *Physical Chemistry Chemical Physics* **15** (39), (2013), pp. 16510-16514.

DOI: 10.1039/c3cp50966d

[148] A. Wang, J. Li, and T. Zhang. "Heterogeneous single-atom catalysis". *Nature Reviews Chemistry* **2** (6), (2018), pp. 65-81.

DOI: 10.1038/s41570-018-0010-1

[149] C.F. Hermanns, M. Bernien, A. Krüger, J. Miguel, and W. Kuch. "Switching the electronic properties of Co-octaethylporphyrin molecules on oxygen-covered Ni films by NO adsorption". *Journal of Physics: Condensed Matter* **24** (39), (2012), pp. 394008.

DOI: 10.1088/0953-8984/24/39/394008

[150] F. Bischoff, Y. He, A. Riss, K. Seufert, W. Auwärter, and J. V. Barth. "Exploration of interfacial porphine coupling schemes and hybrid systems by bond-resolved scanning probe microscopy". *Angewandte Chemie - International Edition* **57** (49), (2018), pp. 16030-16035.

DOI: 10.1002/anie.201808640

[151] S. Haq, F. Hanke, M.S. Dyer, M. Persson, P. Iavicoli, D.B. Amabilino, and R. Raval. "Clean coupling of unfunctionalized porphyrins at surfaces to give highly oriented organometallic oligomers". *Journal of the American Chemical Society* **133** (31), (2011), pp. 12031-12039.

DOI: 10.1021/ja201389u

[152] D. van Vörden, M. Lange, M. Schmuck, J. Schaffert, M.C. Cottin, C.A. Bobisch, and R. Möller. "Communication: substrate induced dehydrogenation: transformation of octa-ethyl-porphyrin into tetra-benzo-porphyrin". *The Journal of Chemical Physics* **138** (21), (2013), pp. 211102.

DOI: 10.1063/1.4810879

[153] C.G. Williams, M. Wang, D. Skomski, C.D. Tempas, L.L. Kesmodel, and S.L. Tait. "Dehydrocyclization of peripheral alkyl groups in porphyrins at Cu(100) and Ag(111) surfaces". *Surface Science* **653**, (2016), pp. 130-137.

DOI: 10.1016/j.susc.2016.06.013

[154] C. Ruggieri, S. Rangan, R.A. Bartynski, and E. Galoppini. "Zinc(II) tetraphenylporphyrin on Ag(100) and Ag(111): multilayer desorption and dehydrogenation". *Journal of Physical Chemistry C* **120** (14), (2016), pp. 7575-7585.

DOI: 10.1021/acs.jpcc.6b00159

[155] A. Wiengarten, J.A. Lloyd, K. Seufert, J. Reichert, W. Auwärter, R. Han, D.A. Duncan, F. Allegretti, S. Fischer, S.C. Oh, Ö. Sağlam, L. Jiang, S. Vijayaraghavan, D. Écija, A.C. Papageorgiou, and J. V. Barth. "Surface-assisted

cyclodehydrogenation; break the symmetry, enhance the selectivity". *Chemistry - A European Journal* **21** (35), (2015), pp. 12285-12290.

DOI: 10.1002/chem.201502001

[156] C.H. Shu, Y.L. Xie, A. Wang, K.J. Shi, W.F. Zhang, D.Y. Li, and P.N. Liu. "On-surface reactions of aryl chloride and porphyrin macrocycles via merging two reactive sites into a single precursor". *Chemical Communications* **54** (89), (2018), pp. 12626-12629.

DOI: 10.1039/C8CC07652A

[157] A.C. Papageorgiou, S. Fischer, S.C. Oh, Ö. Sağlam, J. Reichert, A. Wiengarten, K. Seufert, S. Vijayaraghavan, D. Écija, W. Auwärter, F. Allegretti, R.G. Acres, K.C. Prince, K. Diller, F. Klappenberger, and J. V. Barth. "Self-terminating protocol for an interfacial complexation reaction in vacuo by metal-organic chemical vapor deposition". *ACS Nano* **7** (5), (2013), pp. 4520-4526.

DOI: 10.1021/nn401171z

[158] A.C. Papageorgiou, K. Diller, S. Fischer, F. Allegretti, F. Klappenberger, S.C. Oh, Ö. Sağlam, J. Reichert, A. Wiengarten, K. Seufert, W. Auwärter, and J. V. Barth. "In vacuo porphyrin metalation on Ag(111) via chemical vapor deposition of $Ru_3(CO)_{12}$: mechanistic insights". *Journal of Physical Chemistry C* **120** (16), (2016), pp. 8751-8758.

DOI: 10.1021/acs.jpcc.6b01457

[159] G. Lovat, D. Forrer, M. Abadia, M. Dominguez, M. Casarin, C. Rogero, A. Vittadini, and L. Floreano. "Very high temperature tiling of tetraphenylporphyrin on rutile TiO_2(110)". *Nanoscale* **9** (32), (2017), pp. 11694-11704.

DOI: 10.1039/c7nr04093h

[160] C. Castellarin-Cudia, P. Borghetti, G. Di Santo, M. Fanetti, R. Larciprete, C. Cepek, P. Vilmercati, L. Sangaletti, A. Verdini, A. Cossaro, L. Floreano, A. Morgante, and A. Goldoni. "Substrate influence for the Zn-tetraphenyl-porphyrin adsorption geometry and the interface-induced electron transfer". *ChemPhysChem* **11** (10), (2010), pp. 2248-2255.

DOI: 10.1002/cphc.201000017

[161] M. Di Giovannantonio, M. El Garah, J. Lipton-Duffin, V. Meunier, L. Cardenas, Y. Fagot Revurat, A. Cossaro, A. Verdini, D.F. Perepichka, F. Rosei, and G. Contini. "Insight into organometallic intermediate and its evolution to covalent bonding in surface-confined ullmann polymerization". *ACS Nano* **7** (9), (2013), pp. 8190-8198.

DOI: 10.1021/nn4035684

[162] X. Yang, L. Egger, J. Fuchsberger, M. Unzog, D. Lüftner, F. Hajek, P. Hurdax, M. Jugovac, G. Zamborlini, V. Feyer, G. Koller, P. Puschnig, F.S. Tautz, M.G. Ramsey, and S. Soubatch. "Coexisting charge states in a unary organic monolayer film on a metal". *The Journal of Physical Chemistry Letters* (110), (2019), pp. 6438-6445.

DOI: 10.1021/acs.jpclett.9b02231

[163] P. Kliuiev, G. Zamborlini, M. Jugovac, Y. Gurdal, K. Von Arx, K. Waltar, S. Schnidrig, R. Alberto, M. Iannuzzi, V. Feyer, M. Hengsberger, J. Osterwalder, and L. Castiglioni. "Combined orbital tomography study of multi-configurational molecular adsorbate systems". *Nature Communications* (2019), pp. 5255.

DOI: 10.1038/s41467-019-13254-7

[164] B. Stadtmüller, J. Seidel, N. Haag, L. Grad, C. Tusche, G. Van Straaten, M. Franke, J. Kirschner, C. Kumpf, M. Cinchetti, and M. Aeschlimann. "Modifying the surface of a Rashba-split Pb-Ag alloy using tailored metal-organic bonds". *Physical Review Letters* **117** (9), (2016), pp. 096805.

DOI: 10.1103/PhysRevLett.117.096805

[165] M. Dauth, M. Graus, I. Schelter, M. Wießner, A. Schöll, F. Reinert, and S. Kümmel. "Perpendicular emission, dichroism, and energy dependence in angle-resolved photoemission: the importance of the final state". *Physical Review Letters* **117** (18), (2016), pp. 183001.

DOI: 10.1103/PhysRevLett.117.183001

[166] D. Lüftner, T. Ules, E.M. Reinisch, G. Koller, S. Soubatch, F.S. Tautz, M.G. Ramsey, and P. Puschnig. "Imaging the wave functions of adsorbed molecules". *Proceedings of the National Academy of Sciences* **111** (2), (2014), pp. 605-610.

DOI: 10.1073/pnas.1315716110

[167] P. Kliuiev, T. Latychevskaia, G. Zamborlini, M. Jugovac, C. Metzger, M. Grimm, A. Schöll, J. Osterwalder, M. Hengsberger, and L. Castiglioni. "Algorithms and image formation in orbital tomography". *Physical Review B* **98** (8), (2018), pp. 085426.

DOI: 10.1103/PhysRevB.98.085426

[168] G. Di Santo, C. Sfiligoj, C. Castellarin-Cudia, A. Verdini, A. Cossaro, A. Morgante, L. Floreano, and A. Goldoni. "Changes of the molecule-substrate interaction upon metal inclusion into a porphyrin". *Chemistry - A European Journal* **18** (40), (2012), pp. 12619-12623.

DOI: 10.1002/chem.201201640

[169] P.A. Redhead. "Thermal desorption of gases". *Vacuum* **12** (4), (1962), pp. 203-211.

DOI: 10.1016/0042-207X(62)90978-8

[170] R.I. Masel. *Principles of adsorption and reaction on solid surfaces*. 1st ed. New York, John Wiley & Sons, 1996.

[171] H. Lesnard, M.L. Bocquet, and N. Lorente. "Dehydrogenation of aromatic molecules under a scanning tunneling microscope: pathways and inelastic spectroscopy simulations". *Journal of the American Chemical Society* **129** (14), (2007), pp. 4298-4305.

DOI: 10.1021/ja067442g

[172] H. Lesnard, N. Lorente, and M.L. Bocquet. "Theoretical study of benzene and pyridine STM-induced reactions on copper surfaces". *Journal of Physics: Condensed Matter* **20** (22), (2008), pp. 224012.

DOI: 10.1088/0953-8984/20/22/224012

[173] K. Shen, B. Narsu, G. Ji, H. Sun, J. Hu, Z. Liang, X. Gao, H. Li, Z. Li, B. Song, Z. Jiang, H. Huang, J.W. Wells, and F. Song. "On-surface manipulation of atom substitution between cobalt phthalocyanine and the Cu(111) substrate". *RSC Advances* **7** (23), (2017), pp. 13827-13835.

DOI: 10.1039/c7ra00636e

[174] C.M. Doyle, J.P. Cunniffe, S.A. Krasnikov, A.B. Preobrajenski, Z. Li, N.N. Sergeeva, M.O. Senge, and A.A. Cafolla. "Ni-Cu ion exchange observed for Ni(II)-porphyrins on Cu(111)". *Chemical Communications* **50** (26), (2014), pp. 3447-3449.

DOI: 10.1039/c3cc48913b

[175] M. Cinchetti, K. Heimer, J.P. Wüstenberg, O. Andreyev, M. Bauer, S. Lach, C. Ziegler, Y. Gao, and M. Aeschlimann. "Determination of spin injection and transport in a ferromagnet/organic semiconductor heterojunction by two-photon photoemission". *Nature Materials* **8** (2), (2009), pp. 115-119.

DOI: 10.1038/nmat2334

[176] B. Stadtmüller, S. Emmerich, D. Jungkenn, N. Haag, M. Rollinger, S. Eich, M. Maniraj, M. Aeschlimann, M. Cinchetti, and S. Mathias. "Strong modification of the transport level alignment in organic materials after optical excitation". *Nature Communications* **10** (1), (2019), pp. 1470.

DOI: 10.1038/s41467-019-09136-7

[177] A. Gadalla, O. Crégut, M. Gallart, B. Hönerlage, J.B. Beaufrand, M. Bowen, S. Boukari, E. Beaurepaire, and P. Gilliot. "Ultrafast optical dynamics of metal-free and cobalt phthalocyanine thin films". *The Journal of Physical Chemistry C* **114** (9), (2010), pp. 4086-4092.

DOI: 10.1021/jp911438y

[178] A. Zawadzka, P. Płóciennik, J. Strzelecki, M. Pranaitis, S. Dabos-Seignon, and B. Sahraoui. "Structural and nonlinear optical properties of as-grown and annealed metallophthalocyanine thin films". *Thin Solid Films* **545**, (2013), pp. 429-437.

DOI: 10.1016/j.tsf.2013.07.042

[179] A. Rosa and E.J. Baerends. "Metal-macrocycle interaction in phthalocyanines: density functional calculations of ground and excited states". *Inorganic Chemistry* **33** (3), (1994), pp. 584-595.

DOI: 10.1021/ic00081a029

[180] J. Stöhr and H. König. "Determination of spin- and orbital-moment anisotropies in transition metals by angle-dependent x-ray magnetic circular dichroism". *Physical Review Letters* **75** (20), (1995), pp. 3748-3751.

DOI: 10.1103/PhysRevLett.75.3748

[181] R. Wu and A.J. Freeman. "Limitation of the magnetic-circular-dichroism spin sum rule for transition metals and importance of the magnetic dipole term". *Physical Review Letters* **73** (14), (1994), pp. 1994-1997.

DOI: 10.1103/PhysRevLett.73.1994

[182] J.P. Crocombette, B.T. Thole, and F. Jollet. "The importance of the magnetic dipole term in magneto-circular x-ray absorption dichroism for 3d transition metal compounds". *Journal of Physics Condensed Matter* **8** (22), (1996), pp. 4095-4105.

DOI: 10.1088/0953-8984/8/22/013

[183] G.H.O. Daalderop, P.J. Kelly, and M.F.H. Schuurmans. "Magnetic anisotropy of a

free-standing Co monolayer and of multilayers which contain Co monolayers". *Physical Review B* **50** (14), (1994), pp. 9989-10003.

DOI: 10.1103/PhysRevB.50.9989

[184] B.K. Teo. *EXAFS: basic principles and data analysis*, 1st ed. Berlin, Heidelberg, Springer-Verlag Berlin Heidelberg, 1986.

DOI: 10.1007/978-3-642-50031-2

[185] P. Tegeder. "Optically and thermally induced molecular switching processes at metal surfaces". *Journal of Physics: Condensed Matter* **24** (39), (2012), pp. 394001.

DOI: 10.1088/0953-8984/24/39/394001

[186] K.W. Kolasinski. "Experimental probes and techniques". In: *Surface Science: Foundations of Catalysis and Nanoscience*, 3rd ed. K.W. Kolasinski, Ed. John Wiley & Sons , 2012, pp.51-114.

DOI: 10.1002/9781119941798.ch2

List of publications and conference contributions

Publications

(1) M. Stredansky, S. Moro, M. Corva, M. Jugovac, G. Zamborlini, V. Feyer, C.M. Schneider, I. Cojocariu, **H.M. Sturmeit**, M. Cinchetti, A. Verdini, A. Cossaro, L. Floreano, and E. Vesselli.
"Vibronic fingerprints of the nickel oxidation states in surface-supported porphyrin arrays".
The Journal of Physical Chemistry C **124** (11), (2020), pp. 6297-6303.
DOI: 10.1021/acs.jpcc.0c01387

(2) I. Cojocariu, **H.M. Sturmeit**, G. Zamborlini, A. Cossaro, A. Verdini, L. Floreano, E. D'Incecco, M. Stredansky, E. Vesselli, M. Jugovac, M. Cinchetti, V. Feyer, and C.M. Schneider.
"Evaluation of molecular orbital symmetry via oxygen-induced charge transfer quenching at a metal-organic interface".
Applied Surface Science **504**, (2020), pp. 144343.
DOI: 10.1016/j.apsusc.2019.144343

(3) **H.M. Sturmeit**, I. Cojocariu, M. Jugovac, A. Cossaro, A. Verdini, L. Floreano, A. Sala, G. Comelli, S. Moro, M. Stredansky, M. Corva, E. Vesselli, P. Puschnig, C.M. Schneider, V. Feyer, G. Zamborlini, and M. Cinchetti.
"Molecular anchoring stabilizes low valence Ni(I)TPP on copper against thermally induced chemical changes".
Journal of Materials Chemistry C **8** (26), (2020), pp. 8876-8886.
DOI: 10.1039/d0tc00946f

(4) I. Cojocariu, S. Carlotto, **H.M. Sturmeit**, G. Zamborlini, M. Cinchetti, A. Cossaro, A. Verdini, L. Floreano, M. Jugovac, P. Puschnig, C. Piamonteze, M. Casarin, V. Feyer, and C.M. Schneider.
"Ferrous to ferric transition in Fe-phthalocyanine driven by NO_2 exposure".
Chemistry – A European Journal **27** (10), (2021), pp. 3526-3535.
DOI: 10.1002/chem.202004932

(5) **H.M. Sturmeit**, I. Cojocariu, A. Windischbacher, P. Puschnig, C. Piamonteze, M. Jugovac, A. Sala, C. Africh, G. Comelli, A. Cossaro, A. Verdini, L. Floreano, M. Stredansky, E. Vesselli, C. Hohner, M. Kettner, J. Libuda, C.M. Schneider, G. Zamborlini, M. Cinchetti, and V. Feyer.
"Room-Temperature on-spin-switching and tuning in a porphyrin-based multifunctional interface".
Small (October 12, 2021), pp. 2104779.
DOI: 10.1002/smll.202104779

Talks

- **H. Sturmeit**, G. Zamborlini, S. Ponzoni, M. Jugovac, V. Feyer, C. M. Schneider, and M. Cinchetti.
  "Electronic properties of NiOEP on copper:a molecular orbital tomography study"
  DPG Spring Meeting, Regensburg (DE), April 2nd 2019

- **H. Sturmeit**, I. Cojocariu, G. Zamborlini, M. Jugovac, A. Cossaro, A. Verdini, L. Floreano, M. M. Stredansky, E. Dincecco, E. Vesselli, C. M. Schneider, M. Cinchetti, V. Feyer.
  "Thermal stability of a nickel porphyrin layer deposited on Cu(100) upon annealing"
  12th European School on Molecular Nanoscience (ESMolNa), Elche (ES), May 22nd 2019

Poster

- **H. Sturmeit**, I. Cojocariu, M. Jugovac, A. Windischbacher, P. Puschnig, C. Piamonteze, A. Sala, C. Africh, G. Comelli, A. Cossaro, A. Verdini, L. Floreano, M. Stredansky, E. Vesselli, C. Hohner, M. Kettner, J. Libuda, C. M. Schneider, G. Zamborlini, M. Cinchetti, and V. Feyer
  "A multifunctional organic interface: decoupling the spin tuning from molecule-metal hybridization"
  DPG Spring Meeting of the Surface Science Division, virtual conference, March 4th 2021

Acknowledgements

Finally, I would like to express my gratitude to all the people who supported me during the last few years. Directly or indirectly- each one of them significantly contributed to this Ph.D. thesis project.

First of all, I would like to thank **Prof. Dr. Mirko Cinchetti** for his supervision and everything I learned from him. He was a great teacher, particularly regarding the presentation of collected results in both written publications and oral presentations. Aside from that, he has always been supportive of pursuing ideas for a new experiment. Be it through the purchase of new laboratory equipment or even visits to external user facilities: he was always open to new proposals. Moreover, due to his precise knowledge about the most pressing questions at the frontier of organic spintronics, he has always been able to provide proper guidance and to steer our research efforts into promising directions.

I thank **Dr. Giovanni Zamborlini** for sharing his expertise to set up a neat and tidy experiment from scratch and to pay attention even to the smallest details during the conduction of experiments. These two aspects have essentially contributed to the advances of our group within the last four years. Scientifically, the results of his Ph. D. thesis build the point of departure for this thesis. Without his extensive knowledge about the system NiTPP/Cu(100), as well as the beamtimes and collaborations he initiated, this thesis would not have been possible. Thus, I am very grateful to have worked with him and, more importantly, to have learned from him.

Next, I want to thank **Dr. Stefano Ponzoni** for many fruitful discussions. Without a doubt, his impressively broad knowledge about surface science and laser physics constitutes a significant asset for the group. I am very grateful that his door was always open and that he always took his time to patiently share this knowledge.

I also want to thank **Dr. Vitaliy Feyer** and **Iulia Cojocariu**. Due to their strong experience with several synchrotron-based measurement techniques and their hardworking attitude, our joint beamtimes, as well as the following data analysis and interpretation, were highly efficient. Moreover, besides the late hours, it was always enormous fun, and I enjoyed every beamtime we had together. This work would not have been possible without them.

Prof. Dr. Peter Puschnig and **Andreas Windischbacher** significantly contributed to this work by providing all the above-presented DFT calculations. Moreover, Andreas substantially improved the presentation of the results by providing most of the renderings of the systems presented in our joint publications and in this thesis. I am very grateful to have worked with them as their input from the theoretical side has crucially enhanced our understanding of the data.

I am also very grateful to had the chance to have collaborated with **Dr. Luca Floreano**, **Dr. Albano Cossaro**, and **Dr. Alberto Verdini**. Their tremendous support during the beamtimes and the subsequent data analysis and interpretation of the above presented XPS and NEXAFS results were a fundamental building block in the process of understanding the data presented in this thesis.

I want to thank also **Dr. Alessandro Sala** for providing the high-quality STM images presented in this work and for being open to discussions about the collected results as well as technical aspects of STM.

I also thank **Prof. Dr. Erik Vesselli** and **Dr. Matus Stredansky**. Their support during several beamtimes and the complementary IR-Vis SFG measurements they performed additionally boosted our understanding of the above-presented systems.

The collaboration with **Prof. Dr. Jörg Libuda**, **Dr. Miroslav Kettner**, and **Chantal Hohner** has been highly effective. I am very thankful I had the chance to learn from their high expertise about IRAS.

I also thank **Dr. Cinthia Piamonteze** for her support during our beamtime at PSI and her help with the subsequent data analysis of the above presented XMCD data.

Moreover, I am thankful that **Prof. Dr. Carsten Westphal** has helped to improve this work by suggesting reformulations in the final version of this work that enhanced its readability.

At this point, I also want to name the colleagues that made working at E6 a pleasure by providing a warm and supportive working atmosphere. I would like to highlight the two longest companions, **Fabian Mertens** and **Marc Terschanski**, as well as **David Janas**, **Valentin Mischke**, and **Jonah Nitschke** from the photoemission branch of the group: you made working in our group fun, keep up the good work.

Last but not least, I want to thank my whole **family** for their unconditional backing. I am deeply indebted for this.

Thank you.